

Zhang, Mingqi (2026) *Terahertz quantum communication with superconducting circuits.* PhD thesis.

https://theses.gla.ac.uk/86331/

Copyright and moral rights for this work are retained by the author

A copy can be downloaded for personal non-commercial research or study, without prior permission or charge

This work cannot be reproduced or quoted extensively from without first obtaining permission from the author

The content must not be changed in any way or sold commercially in any format or medium without the formal permission of the author

When referring to this work, full bibliographic details including the author, title, awarding institution and date of the thesis must be given

In reference to IEEE copyrighted material which is used with permission in this thesis, the IEEE does not endorse any of University of Glasgow's products or services. Internal or personal use of this material is permitted. If interested in reprinting/republishing IEEE copyrighted material for advertising or promotional purposes or for creating new collective works for resale or redistribution, please go to http://www.ieee.org/publications_standards/publications/rights/rights_link.html to learn how to obtain a License from RightsLink.

Enlighten: Theses
https://theses.gla.ac.uk/
research-enlighten@glasgow.ac.uk

# TERAHERTZ QUANTUM COMMUNICATION WITH SUPERCONDUCTING CIRCUITS

Mingqi Zhang

Supervisor: Prof Kaveh Delfanazari

Submitted in fulfilment of the requirements for the

Degree of Doctor of Philosophy

James Watt School of Engineering

College of Science and Engineering

University of Glasgow




June 2026

# Abstract

The increasing demand for high-capacity and secure wireless communication has driven increasing interest in millimetre-wave (mm-wave) and terahertz (THz) frequencies for next-generation communication, especially for wireless quantum communication. However, their practical deployment is limited by severe propagation losses, hardware constraints, and the lack of integrated quantum communication frameworks. This work investigates continuous-variable quantum key distribution (CVQKD) in the mm-wave and THz regimes by considering cryogenic environments, multiple-input multiple-output (MIMO) schemes, multicarrier transmission techniques, and superconducting THz hardware. Both single-input single-output (SISO) and MIMO architectures of CVQKD are studied between 100 GHz and 1 THz under cryogenic conditions, demonstrating that positive secret key rates are achievable. THE MIMO CVQKD protocol can significantly enhance the secure transmission distance. In addition, an OFDM-based CVQKD protocol is developed, incorporating modulation-induced excess noise and frequency-dependent atmospheric absorption. Results show that multicarrier transmission improves secret key rates compared with single-carrier systems, although performance is limited by noise accumulation and system imperfections. With the consideration of hardware accomplishment, a high-temperature superconducting chip-scale THz emitter based on $Bi_2Sr_2CaCu_2O_{8+\delta}$ is experimentally evaluated. The device exhibits long-term stable coherent THz emission with tunable radiation in the 100 GHz–1 THz range, demonstrating its potential as a practical hardware for quantum communication systems. Overall, this thesis establishes a unified framework for THz quantum communication by integrating protocol development and enabling hardware, providing a foundation for future high-capacity and quantum-secure wireless networks.

# Contents

**ABSTRACT** ..... **I**

**CONTENTS** ..... **II**

**ACKNOWLEDGEMENTS** ..... **IV**

**CHAPTER 1 INTRODUCTION** ..... **1**

**CHAPTER 2 MILLIMETER-WAVES TO TERAHERTZ SISO AND MIMO CONTINUOUS VARIABLE QUANTUM KEY DISTRIBUTION** ..... **7**

2.1 ABSTRACT ..... 7

2.2 INTRODUCTION ..... 8

2.3 SYSTEM MODEL ..... 10

*2.3.1 Channel* ..... *11*

*2.3.2 Secret key rate* ..... *15*

*2.3.3 System condition* ..... *18*

2.4 SIMULATION RESULT ..... 19

*2.4.1 Simulation of the MIMO system* ..... *19*

*2.4.2 Simulation of the SISO system* ..... *21*

2.5 DISCUSSION ..... 22

2.6 CONCLUSION ..... 23

2.7 APPENDIX A ..... 24

*2.7.1 Computation of channel model* ..... *24*

*2.7.2 Computation of the secret key rate* ..... *27*

**CHAPTER 3 ORTHOGONAL FREQUENCY DIVISION MULTIPLEXING CONTINUOUS VARIABLE TERAHERTZ QKD FOR LARGE-SCALE WIRELESS QUANTUM COMMUNICATION** ..... **29**

3.1 ABSTRACT ..... 29

3.2 INTRODUCTION ..... 30

3.3 SYSTEM MODELING ..... 32

*3.3.1 THz OFDM CVQKD protocol* ..... *32*
*3.3.2 Modulation noise* ..... *35*
3.4 SECRET KEY RATE ..... 39
3.5 RESULTS ..... 43
*3.5.1 Open-air channel* ..... *43*
*3.5.2 THz OFDM CVQKD Cryogenic links* ..... *50*
3.6 PROPOSAL FOR THZ QKD WITH SUPERCONDUCTING COHERENT PHOTON SOURCES ..... 52
3.7 CONCLUSION ..... 55
3.8 APPENDIX B ..... 57
**CHAPTER 4 TUNABLE TERAHERTZ SOURCE ON A CHIP WITH DECADE-LONG STABILITY USING LAYERED-SUPERCONDUCTOR ELLIPTICAL MICROCAVITIES ..... 59**
4.1 ABSTRACT ..... 59
4.2 INTRODUCTION ..... 60
4.3 TUNABLE COHERENT THZ SOURCE FABRICATION AND MEASUREMENT SETUP ..... 62
4.4 TUNABLE COHERENT THZ RADIATION SOURCE SUSTAINED OVER 11 YEARS ..... 63
4.5 FREE-SPACE OVER-THE-AIR THZ RADIATION FREQUENCY MEASUREMENT ..... 67
4.6 COHERENT THZ PHOTON RADIATION RATE ..... 73
4.7 CONCLUSION ..... 75
4.8 APPENDIX C ..... 76
**CHAPTER 5 CONCLUSIONS AND OUTLOOK ..... 83**
**REFERENCES ..... 85**

# Acknowledgements

I would like to express my sincere gratitude to my supervisor, Prof Kaveh Delfanazari, for giving me the opportunity to work in this challenging and fascinating research field. His continuous encouragement, insightful discussions, and invaluable guidance have had a profound impact on the development of this research.

I am also deeply grateful to my second supervisor, Prof. Muhammad Ali Imran, for his support and guidance, particularly in the broader context of terahertz (THz) technologies and their applications.

I would further like to thank Prof. Kashiwagi Takanari for his generous support and for sharing his expertise during my short-term research visits at the University of Tsukuba, Japan.

I acknowledge the support of the JWNC cleanroom facility, where a significant portion of the device fabrication work was carried out. I sincerely appreciate the assistance and collaboration of the staff and research community, whose contributions were essential to the success of this project.

Finally, I would like to express my heartfelt gratitude to my family, friends, and colleagues for their unwavering support throughout my studies. I am especially thankful to my family for their constant encouragement and sacrifices, which have made this journey possible. I would not be the person I am today without them.

# Chapter 1
# Introduction

The rapid evolution of wireless communication systems has led to a critical demand for higher carrier frequencies, broader spectral resources, and fundamentally new communication models [1, 2]. Conventional microwave and radio-frequency (RF) bands are increasingly unable to support the precise requirements of next-generation networks in terms of data rate, latency, connectivity density, and security. In this context, the millimetre-wave (mm-wave) and terahertz (THz) frequency bands, spanning approximately 100 GHz to 10 THz, bridging the gap between microwave and optical regimes, have emerged as key enablers for future beyond-5G and 6G communication systems [3-7].

The THz spectral region offers undeveloped opportunities with inherently large bandwidths, enabling ultra-high data-rate transmission, potentially reaching terabit-per-second (Tb/s) capacities. In addition, THz radiation exhibits enhanced transmission through non-metallic materials and improved robustness under adverse atmospheric conditions such as fog and dust [8, 9]. These characteristics make THz systems highly attractive for applications such as ultra-fast wireless communications, high-resolution sensing, imaging, and space-air-ground integrated networks [3-7]. However, the practical exploitation of THz bands remains significantly constrained by the lack of efficient, compact, and power-scalable THz sources, detectors, and system-level components capable of operating reliably in this frequency range [1-7, 10-21].

In recent years, substantial progress has been made in addressing this gap through advances in electronic, photonic, and plasmonic technologies. Novel THz emitters [22-29], integrated antennas [30-34], modulators [35-47], and detectors [15, 44, 48-50] have demonstrated improved efficiency and tunability, gradually enabling the potential of practical THz systems. However, the performance of THz systems remains limited by propagation losses, atmospheric absorption, and device-level non-idealities, particularly when operating in realistic free-space environments. A fundamental challenge in THz wireless communication arises from frequency-dependent atmospheric attenuation. Electromagnetic waves propagating through free space are subject to absorption and scattering caused by molecular gases, water vapour, aerosols, fog, and precipitation. In particular, molecular absorption lines associated with water vapour ($H_2O$) and carbon dioxide ($CO_2$) introduce significant attenuation, which becomes increasingly severe at THz frequencies [51, 52]. As a result, the effective transmission distance of THz systems is strongly frequency-selective, making the identification and exploitation of low-loss transmission windows essential for practical deployment.

In parallel with classical THz communication development, quantum communication has developed significantly over the past decade, particularly in quantum key distribution (QKD). In basic QKD, two users, normally referred to as Alice and Bob, exchange quantum states over a communication channel to establish a shared secret key. According to the principles of quantum mechanics, an eavesdropper (Eve) attempting to measure the transmitted quantum states generally introduces detectable disturbances, allowing the users to recognise the presence of eavesdropping. This provides QKD with a fundamentally different security mechanism from conventional cryptographic schemes, whereas conventional cryptographic schemes typically rely on the computational hardness of mathematical problems [53-56]. Based on the type of quantum states used to encode information, QKD can be categorised into discrete-variable QKD (DVQKD) and continuous-variable QKD (CVQKD) [57]. CVQKD is particularly attractive due to its compatibility with standard coherent detection techniques, such as homodyne and

heterodyne detection, its high potential secret key rates, and its integration availability with existing communication infrastructure [58]. Quantum communication based on quantum key distribution (QKD) at THz frequencies enables secure wireless links between spatially separated users through free-space and inter-satellite channels [10, 59]. Owing to its unique propagation characteristics, THz-QKD is a promising candidate for constructing local quantum-secure wireless networks, providing an important complement to long-distance optical fibre-based QKD systems.

The extension of CVQKD into the THz regime introduces both opportunities and challenges. On one hand, THz frequencies offer wireless potential for quantum communication with large bandwidths, enabling high-capacity quantum-secure links without physical connection limitations. On the other hand, operation in this regime is accompanied by strong thermal noise, frequency-dependent channel loss, and stringent hardware requirements, which are not fully captured by conventional models developed for optical QKD systems. To improve system capacity and spectral efficiency, spatial multiplexing techniques such as cc (MIMO) architectures have been widely adopted in classical wireless communications. Their extension to quantum communication systems offers a promising pathway for enhancing secret key rates and secure distance under limited bandwidth and power constraints [60, 61]. However, most existing studies on THz QKD have primarily focused on simplified single-carrier configurations and idealised room-temperature assumptions [53], leaving several critical aspects insufficiently addressed, including realistic multi-antenna operation, low-temperature environments, and combined channel–hardware interactions.

In addition to spatial multiplexing, multicarrier modulation schemes such as orthogonal frequency-division multiplexing (OFDM) provide an alternative strategy for improving spectral efficiency in THz CVQKD systems. By decomposing a high-rate data stream into multiple narrowband subcarriers, OFDM enables parallel key distribution using a single transceiver architecture, thereby simplifying system design while maintaining high

throughput [62]. However, existing theoretical models often rely on idealised assumptions that neglect important practical impairments, including modulation-induced excess noise, inter-subcarrier crosstalk, and frequency-dependent atmospheric absorption. These simplifications may lead to overly optimistic estimations of secret key rates and system performance.

The realisation of hardware, especially efficient and stable coherent THz sources, remains one of the most critical bottlenecks for the practical deployment of THz quantum communication systems. Different THz source technologies offer different trade-offs among operating temperature, frequency coverage, output power, and system integration, as illustrated in Fig. 1.1. Conventional electronic approaches face increasing limitations in output power and bandwidth towards the higher-frequency THz range, while photonic approaches often require relatively complex optical or electro-optic configurations. Photonic approaches based on optical-to-THz conversion can provide broadband and coherent THz generation and facilitate the distribution of a stable optical reference or local oscillator over relatively long distances. However, they generally require additional optical

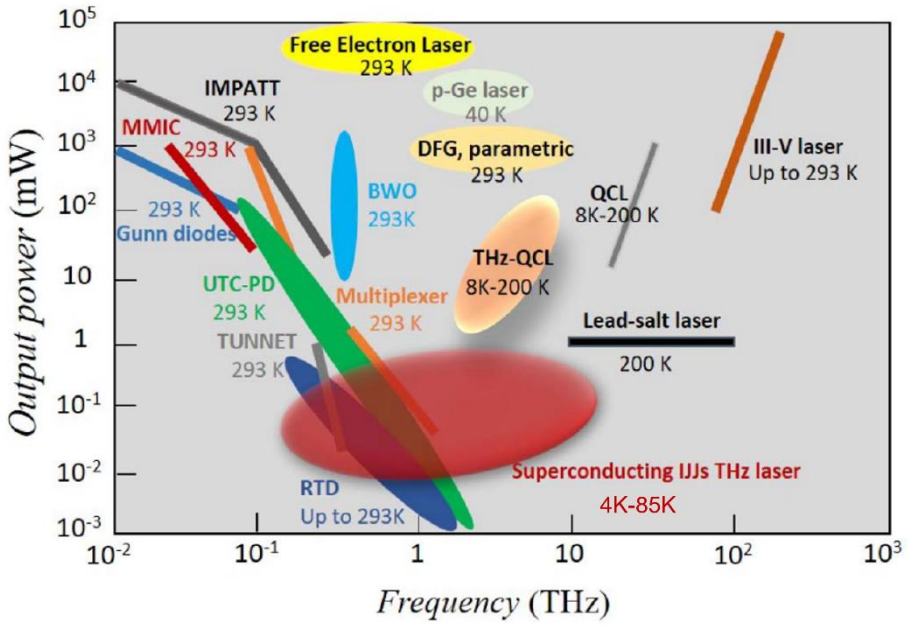



**Fig. 1.1.** The schematic of different types of THz sources and their typical operating temperatures, frequency coverage, and output power [15].

sources, fibres, precise optical components, and conversion stages, increasing system complexity, alignment requirements, and physical space. Such additional optical hardware may become a practical constraint when developing compact THz quantum communication platforms, particularly where limited space, environmental robustness, or integration with other quantum hardware and quantum computers needs to be considered. Solid-state and superconducting THz sources, such as quantum cascade lasers (QCLs) [63], resonant tunnelling diodes (RTDs) [64], and Josephson plasma emitters (JPEs), therefore provide promising alternatives for reducing hardware complexity and enabling more compact implementations. Among these technologies, JPEs based on the Josephson-junction effect in superconducting structures are particularly attractive because of their broad frequency coverage, with reported THz radiation extending from approximately 0.1 to 11 THz [65-67]. They also offer electrically tunable emission with relatively low driving voltage and power, together with the potential for compact solid-state implementation and long operational lifetime [68]. In particular, the high-temperature superconducting materials such as $Bi_2Sr_2CaCu_2O_{8+\delta}$ (BSCCO) can operate at temperatures well above those required by dilution refrigerators, with THz emission demonstrated at temperatures approaching or exceeding the liquid-nitrogen range [66, 69, 70]. These characteristics make BSCCO-based JPEs particularly attractive for compact and tunable THz sources in quantum communication applications.

BSCCO-based superconducting intrinsic Josephson junctions (IJJs) THz emitters have demonstrated remarkable potential as coherent THz radiation sources. The BSCCO THz emitters exploit macroscopic quantum coherence across stacked Josephson junctions, enabling phase-synchronised emission through cavity resonance effects [15, 65, 67, 71-74]. Our recent advances reported in Chapter 3, including elliptical microcavity geometries, have enabled enhanced mode control and improved spectral tunability, which is highly desirable for wireless communication applications [68]. Moreover, long-term experimental evidence has demonstrated that such devices can maintain stable superconducting and emission characteristics over extended periods, even after more than a decade of

fabrication, highlighting their exceptional robustness for practical deployment in cryogenic and free-space environments [68].

Despite these promising developments, a key limitation persists: current THz CVQKD system models often fail to integrate realistic hardware behaviour, channel-dependent absorption profiles, and system-level noise sources into a unified framework. This leads to a significant gap between theoretical performance predictions and experimentally achievable results.

Motivated by these challenges, this thesis aims to develop a comprehensive framework for continuous-variable quantum key distribution (CVQKD) in the mm-wave and THz frequency regimes under realistic physical and system constraints, with particular emphasis on cryogenic operation environments, spatial multiplexing, and multicarrier modulation techniques. We develop and analyse CVQKD systems operating in the mm-wave to THz frequency range under cryogenic temperatures, incorporating both SISO and MIMO architectures to evaluate their impact on secret key rate performance. We also propose and analyse an OFDM-based CVQKD scheme that incorporates modulation-induced excess noise and frequency-dependent atmospheric absorption across subcarriers, providing a more physically accurate performance evaluation than existing models. With the hardware-informed considerations, we examine superconducting BSCCO-based THz emitters with long-term stability and cavity-engaged emission properties, evaluating their relevance as a potential practical source for cryogenic quantum-secure wireless communication systems.

The remainder of this thesis is organised into 4 Chapters. Chapter 2 presents the simulation and analysis of THz SISO and MIMO CVQKD propagation under a cryogenic environment. Chapter 3 introduces the system models for OFDM CVQKD in the THz frequency ranges with detailed consideration of modulation noise and existing hardware. Chapter 4 discusses high-temperature superconducting BSCCO THz sources and their characteristics. Chapter 5 concludes the thesis and outlines future research directions.

# Chapter 2
# Millimeter-Waves to Terahertz SISO and MIMO Continuous Variable Quantum Key Distribution

**Publication statement:** *©2023 IEEE. Reprinted, with permission, from [M. Zhang, S. Pirandola and K. Delfanazari, "Millimeter-Waves to Terahertz SISO and MIMO Continuous Variable Quantum Key Distribution," in IEEE Transactions on Quantum Engineering, vol. 4, pp. 1-10, 2023, Art no. 4100410, doi: 10.1109/TQE.2023.3266946.]*

## 2.1 Abstract

With the exponentially increased demands for large bandwidth, it is important to think about the best network platform as well as the security and privacy of the information in communication networks. Millimeter (mm)-waves and terahertz (THz) with high carrier frequencies are proposed as enabling technologies to overcome Shannon's channel capacity limit of existing communication systems by providing ultrawide bandwidth signals. Mm-waves and THz are also able to build wireless links compatible with optical communication systems. However, most solid-state components that can operate reasonably efficiently at these frequency ranges (100 GHz–10 THz), especially sources and detectors, require cryogenic cooling, as is a requirement for most quantum systems. Here, we show that secure mm-waves and THz quantum key distribution (QKD) can be achieved when the sources and detectors operate at cryogenic temperatures down to $T = 4$ K. We compare single-input single-output and multiple-input multiple-output (MIMO) continuous

variable THz quantum key distribution (CVQKD) schemes and find the positive secret key rate in the frequency ranges between $f$ = 100 GHz and 1 THz. Moreover, we find that the maximum transmission distance could be extended, the secret key rate could be improved at lower temperatures, and achieve a maximum secret communication distance of more than 5 km at $f$ = 100 GHz and $T$ = 4 K by using 1024 × 1024 antennas. Our results for the first time show the possibility of mm-waves and THz MIMO CVQKD with the system operating at temperatures below $T$ = 50 K, which may contribute to the efforts to develop next-generation secure wireless communication systems and quantum internet for applications from intersatellite and deep space to indoor and short-distance communications.

## 2.2 Introduction

With the extension of wireless communication and the fast development of information security, higher carrier frequencies and more spectral resources are required [1, 2]. Millimetre (mm)- and terahertz (THz)- waves [12-15] offer ultrawide bandwidth and high-speed data rate communication and are considered to build next-generation (6G) communication systems [3-7]. Mm-waves and THz bands lie between the mature microwave and optical bands as less explored area [10, 11, 16-18]. A gap in the electromagnetic spectrum exists at these frequency ranges due to the inefficiency and impracticality of the devices and circuits [1-7, 10-21]. However, the recent development of electronic, photonic and plasmonic-based mm-waves and THz technologies helps close this gap with the demonstration of power-efficient sources [22-28], antennas [30-34], filters [75-77], waveguides [32, 78-82], modulators [35-45], and detectors [15, 44, 48-50]. Demands for 6G include, but are not limited to, Terabit per second (Tb/s), mm-precision sensing and positioning, seamless connectivity, and ultrafast wireless communications [3-7]. Moreover, practical implementation of quantum processors and quantum computers operating at low temperatures (cryogenics) [83-85], requires massive open-air and free-

space data transfer from and to high-performance classical processors, computers, and communication systems. Therefore, to realise a robust building block for practical quantum information processing, attention should be on both security and low-temperature operation. Electromagnetic waves travelling through the free space channel will be impacted by a number of atmospheric effects, such as atmospheric attenuation caused by absorption and scattering, atmospheric radiance, and atmospheric turbulence [86]. The atmospheric attenuation from molecules, particles or liquid droplets including gases, aerosols (dust), fog or precipitation are frequency dependence [52]. Compared with the free-space optical link, the THz link is more stable against the scattering under harsh environments such as fog [8] and dust [9] conditions. The limit of mm-waves [87] and THz links [88, 89] in long distances is mainly caused by the absorption from different gases in air, such as gaseous water vapor ($H_2O$) and carbon dioxide ($CO_2$) [51, 52]. So it is important to find the window with low atmospheric absorption through this band. High-level security is also an important aspect of realising mm-waves and THz communications, which is quite challenging to maintain with classical cryptography schemes. Quantum key distribution (QKD) can help to achieve the goal of high-level unconditional security with the power of the quantum physics [53-56]. QKD could be divided into discrete variables (DVQKD based on single photon sources and detectors) and continuous variables (CVQKD based on standard communication systems) [54-56, 58, 60, 61, 90-97]. CVQKD uses coherent homodyne detection instead of single photon detection [90] and could be integrated with next-generation communication systems [58].

Single-input single-output (SISO) is a kind of classical communication system where the transmitter and receiver don't have several antennas. To meet the explosion of data transmission, multiple-input multiple-output (MIMO) technology has been widely used in wireless communication nowadays. MIMO system with multiple antennas at both the transmitter and receiver sides bring benefits on data throughout and communication range with limited bandwidth and transmit power [60]. THz QKD with SISO and MIMO systems

was introduced in Refs [53] and [61], with the main focus on mid- and far-infrared frequency ranges (10THz-40THz) at room temperature ($T$= 296 K).

Motivated by the works of [53] and [61], this work focuses on SISO and MIMO QKD at the temperature of $T$< 50 K. We investigate CVQKD at frequency ranges of mm-waves and THz, from $f$=100 GHz to 1 THz, with antennas and detectors both operating in the cryogenic environment ($T$< 50 K). Moreover, we compare the performance of both the SISO and MIMO CVQKD systems at this frequency range.

## 2.3 System model

For the proposed mm-waves and THz quantum communication scheme, the cryogenic antennas generate electromagnetic (EM) fields that oscillate at an angular frequency ω. This EM field is quantized and the system gets a Hamiltonian $H = h\omega(\hat{a}^{\dagger}\hat{a} + \frac{1}{2})$. The $H$ is similar to the Hamiltonian of a quantum harmonic oscillator with $h$ as Planck's constant, $\hat{a}$ as the annihilation operator, and $\hat{a}^{\dagger}$ as the creation operator. Moreover, the quadrature field operators $\hat{\mathrm{q}} = \frac{\hat{a}+\hat{a}^{\dagger}}{\sqrt{2}}$ and $\hat{\mathrm{p}} = \frac{\mathrm{i}(\hat{a}+\hat{a}^{\dagger})}{\sqrt{2}}$ are dimensionless canonical observables of the system (similar to the position and momentum of the quantum harmonic oscillator) [91]. Finally, coherent states of the system are the eigenstates of the annihilation operator $\hat{a}$, provided by $\hat{a}|\alpha\rangle = \alpha|\alpha\rangle$. Here, $\alpha = q + \mathrm{i}p \in \mathrm{C}$ indicates the coherent state amplitude [61], taken from a two-dimensional Gaussian distribution. Two independent continuous variables $q$ and $p$ are used to create a secret key between Alice and Bob [53].

Notation: Boldface and italic capital letters such as $\boldsymbol{A}$ denote matrices. $\boldsymbol{A}^{\dagger}$ is the conjugate transpose of matrix $\boldsymbol{A}$ while $\boldsymbol{A}^{T}$ is the transpose. $\mathbf{0}_{M\times N} \in \mathbb{C}^{M\times N}$ is a zero complex matrix and $\mathbf{1}_{M\times N} \in \mathbb{C}^{M\times N}$ is a complex matrix of ones. $\boldsymbol{I}_{M}$ represents a $M \times M$ identity matrix. A $M \times M$ diagonal matrix described by $diag(\boldsymbol{a})$ with $\boldsymbol{a} \in \mathbb{C}^{M}$ shows $\boldsymbol{a}$ on its

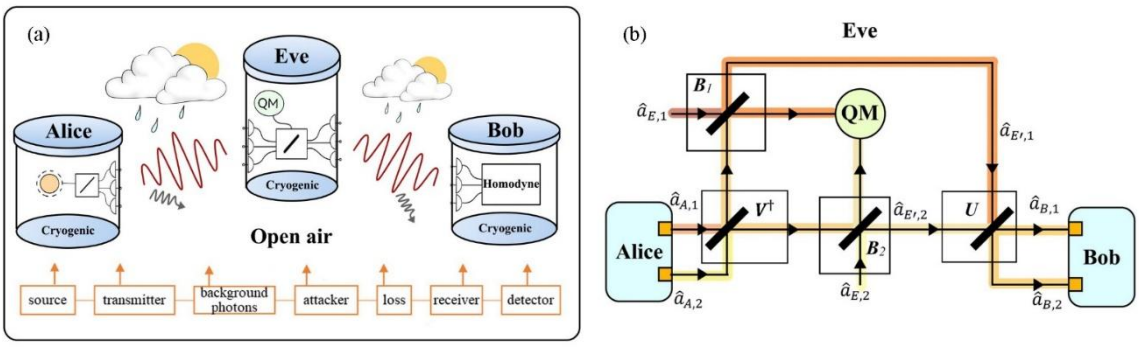



**Fig. 2.1.** (a) The system model of the proposed mm-waves and THz QKD. Alice prepares thermal states at the source which denotes a generator. The transmitter and receiver are antennas distributed in a one-dimensional uniform linear array (ULA). Alice, Bob, and Eve do their job at cryogenic ambient (low temperature). The channel loss through the open-air environment contains atmospheric absorption and free-space loss. Eve's output modes are stored in a quantum memory (QM). Bob uses a homodyne detector to measure quadrature. (b) The schematic of the phase shifters model described for a 2×2 MIMO system. The channel is modelled by 4 beam splitters. Alice generates 2 coherent states $\hat{a}_{A,1}$ and $\hat{a}_{A,2}$ based on random vectors and send them out from her 2 antennas as thermal states. These two states are mixed by the first beam-splitter $\boldsymbol{V}^{\dagger}$. Then Eve operates collective Gaussian attack. She prepares two two-mode squeezed vacuum states and uses beam-splitter $\boldsymbol{B}_1$ and $\boldsymbol{B}_2$ to combine the input and her states. The output and one of the original modes are saved in quantum memory (QM). Before Bob detects the input, the signals are mixed by beam-splitter $\boldsymbol{U}$. At last, Bob uses his two antennas to receive the modes $\hat{a}_{B,1}$ and $\hat{a}_{B,2}$.

diagonal. And $\mathcal{N}(\mu, \boldsymbol{\Sigma})$ is a real multivariate Gaussian distribution in which the vector is $\mu$ and the covariance matrix (CM) is $\boldsymbol{\Sigma}$.

### 2.3.1 Channel

We consider a one-way communication channel to build a secret key between Alice and Bob, as shown in Fig.2.1 (a). A MIMO mm-waves and THz communication channel between Alice and Bob includes a transmitter with $N_t$ antennas at Alice's side and a receiver with $N_r$ antennas at Bob's side. We assume the antennas at both sides are distributed in a one-dimensional uniform linear array (ULA) with each antenna element's gain $G_a$. As the crosstalk between the antennas could be reduced by using proper structure and material, we ignore the crosstalk in this work [98]. So the antenna gains of Alice and Bob are $G_t = N_t G_a$ and $G_r = N_r G_a$ [61]. The Gaussian modulation of the thermal state is a widely used encoding protocol for several frequencies [53]. Alice begins with a vacuum state $|0\rangle$ and generates $N_t$ coherent states $|a_i\rangle$ with amplitudes $a_i = Q_{A,i} +$

$jP_{A,i}$, $i = 1,2,\ldots,N_t$ from the $N_t$ antennas with quadratures being chosen from two independent random vectors $\boldsymbol{Q}, \boldsymbol{P} \sim \mathcal{N}\left(\mathbf{0}_{N_t \times 1}, V_s \boldsymbol{I}_{N_t}\right)$ where $V_s$ is the variance of the initial signal encoding [61]. Two quadratures $\hat{Q}_{A,i}$ and $\hat{P}_{A,i}$ of a quantum THz source (thermal) state are randomly sent by the *i*-th antenna element of Alice and described by $\hat{X}_{A,i} \in \{\hat{Q}_{A,i}, \hat{P}_{A,i}\}$. So the *i*-th mode of Alice can be considered as $\hat{X}_{A,i} = a_i + \hat{0}$, where $\hat{0}$ is the thermal mode (quadrature operator) due to the background thermal noise at mm-waves and THz and $X_{\mathrm{Ai}}$ denotes the classical modulated variable [53, 99]. The total variance of Alice's mode is

$$V_a = V_s + V_0 \tag{1}$$

where $V_0$ is the variance of thermal state (contains variance of vacuum mode and variance of preparation noise) [53]. $V_0$ is defined as

$$V_0 = 1 + 2\bar{n} \tag{2}$$

Here, 1 is the vacuum shot noise unit (SNU) and

$$\bar{n} = \left[\exp\left(\frac{hf_c}{k_B T}\right) - 1\right]^{-1} \tag{3}$$

is the mean thermal photon number, $h$ is Planck's constant, $k_B$ denotes Boltzmann's constant, $T$ is the environment temperature, and $f_c$ is the carrier frequency. Now, let's consider Alice sends her states to Bob (receiver) over an insecure quantum channel. Bob uses a noisy homodyne detection technique, which is based on mm-waves and THz shot-noise limited quantum detector that randomly switches between quadrature $\hat{Q}$ and $\hat{P}$, to measure the incoming thermal states.

The channel matrix between Alice and Bob could be modelled as [61, 92, 93]

$$\boldsymbol{H} = \sum_{l=1}^{L} \sqrt{\gamma_l} e^{j2\pi f_c \tau_l} \psi_{N_r}(\phi_{r,LOS}) \psi_{N_t}^{\dagger}(\phi_{t,LOS}) \tag{4}$$

where, $\boldsymbol{H} \in \mathbb{C}^{N_r \times N_t}$, $L$ is the full number of multipath components, $\tau_l$ is the propagation delay of the $l$-th multipath. We only consider the line-of-sight (LOS) path with $L$=1 in this work. So the path loss $\gamma_l$ is given by [61]

$$\gamma_{l=1} = G_t G_r \left(\frac{\lambda}{4\pi d}\right)^2 10^{-\frac{\delta d}{10}} \tag{5}$$

where $d$ is the distance (km) between Alice and Bob and $\delta$ is the atmospheric loss and is defined as dB/km [53, 92]. It contains both the free space path and the atmospheric absorption losses of mm-waves and THz waves. $\phi_{r,LOS}$ and $\phi_{t,LOS}$ is the angle of arrival seen by Bob, and the angle of departure from Alice, respectively. $\psi_K(\theta)$ represents the array response vector of a ULA, which contains $K$ number of antennas.

The derivation details of the channel model are described by a singular-value decomposition (SVD) scheme introduced by Ref. [61] and presented in Appendix A.

Although the coherent attack is the general attack, the works reported in Refs. [94, 95] proved that once the system is secure against collective attacks, it is also secure against general attacks with the long secret key. In CVQKD, the most realistic and studied collective attack against Gaussian protocols is the entangling cloner attack [53]. So, we assume the channels are totally under Eve's control, and she uses entangling cloners to steal information. Fig.2.1 (b) shows a $2 \times 2$ MIMO system built by 4 beam-splitters as an example [91]. After the two transmitted modes from Alice are combined by the beam-splitter $\boldsymbol{V}^{\dagger}$, Eve will pick up two produced output modes. Eve should prepare two pairs of

entangled Einstein-Podolsky-Rosen $\{\hat{e}_1, \hat{E}_1\}$ and $\{\hat{e}_2, \hat{E}_2\}$ (known also as two-mode squeezed vacuum states) in advance. Once received the input, Eve uses $\boldsymbol{B}_1$ and $\boldsymbol{B}_2$ to combine them with $\hat{E}_1$ and $\hat{E}_2$. The relationship of input and output of $\boldsymbol{B}_i$ can be written as [61, 91]

$$\begin{bmatrix} \hat{a}_{out,1} \\ \hat{a}_{out,2} \end{bmatrix} = \begin{bmatrix} \sqrt{\eta_i} & \sqrt{1-\eta_i} \\ -\sqrt{1-\eta_i} & \sqrt{\eta_i} \end{bmatrix} \begin{bmatrix} \hat{a}_{in,1} \\ \hat{a}_{in,2} \end{bmatrix} \tag{6}$$

Here, $\eta_i$ is the round-trip transmissivity of a two-port beam-splitter $\boldsymbol{B}_i$. Then Eve will save one of the outputs from every beam-splitters $(\hat{E}'_1, \hat{E}'_2)$ and the original modes $(\hat{e}_1, \hat{e}_2)$ in her quantum memory (QM) and measure the ancilla modes to exploit information when Alice and Bob completed their classical communication. The other two output modes will be combined by the beam-splitter $\boldsymbol{U}$ and sent to Bob. We assume Alice applies $\boldsymbol{V}$ as the base of beamforming at her end, and Bob employs $\boldsymbol{U}^\dagger$ as the base of decoding at his side. The whole model could be described by [61, 91]

$$\hat{\boldsymbol{a}}_B = \boldsymbol{U}^\dagger \boldsymbol{H} \boldsymbol{V} \hat{\boldsymbol{a}}_A + \boldsymbol{U}^\dagger \boldsymbol{U} \boldsymbol{S} \hat{\boldsymbol{a}}_E \tag{7}$$

where $\hat{\boldsymbol{a}}_B = [\hat{a}_{B,1}, \dots, \hat{a}_{B,N_r}]^T$ is the received mode of Bob, $\hat{\boldsymbol{a}}_A = [\hat{a}_{A,1}, \dots, \hat{a}_{A,N_t}]^T$ is the transmitted mode of Alice, $\hat{\boldsymbol{a}}_E = [\hat{a}_{E,1}, \dots, \hat{a}_{E,N_t}]^T$ is the injected Gaussian mode of Eve.

$$\boldsymbol{S} = diag\{\sqrt{1-\eta_1}, \dots, \sqrt{1-\eta_r}, \boldsymbol{1}_{(M-r)\times 1}\} \tag{8}$$

is a diagonal matrix with $M = \min(N_t, N_r)$. The calculation details could be found in Appendix A. The efficient channel between Alice and Bob can be disintegrated into *r* parallel SISO channels by utilizing the SVD of $\boldsymbol{H}$ (*r* is the rank of $\boldsymbol{H}$). In this case, the relation between channels' input and output can be written as [61]

$$\hat{\boldsymbol{a}}_{B,i} = \sqrt{t_i}\hat{\boldsymbol{a}}_{A,i} + \sqrt{1-t_i}\hat{\boldsymbol{a}}_{E,i}, \qquad i = 1,2,\dots,r \tag{9}$$

Here, $t_i$ is the *i*-th non-zero eigenvalue of $\boldsymbol{H}^{\dagger}\boldsymbol{H}$ and could also be considered as the *i*-th transmissivity of the channel. Homodyne experiments on one of the randomly selected quadratures will be performed by Bob for every *r*-received mode and get the result detailed in Appendix A.

We set *W* to the variance of the thermal noise introduced by Eve. So, Bob will receive the *i*-th mode with the shot-noise level $V(\hat{X}_{B,i}) = t_i V_0 + (1-t_i)W$ [53]. $\hat{X}_{B,i}$ is Bob's received quadrature described by Eq. (22) in Appendix A. If Eve wants to completely hide in the background noise, she can use $W = V_0$. Then Bob will receive the shot-noise level $V(\hat{X}_{B,i}) = V_0$ which is the same as what Alice sent. Although the value of $V_0$ could be enlarged by frequencies below 1THz, we could gain $V_0 \approx 1\ SNU$ by cooling down the system to low temperatures.

### 2.3.2 Secret key rate

In this mm-waves and THz CVQKD scheme, Alice and Bob replicate the previous quantum communication protocol several times to generate a string. Then they correct errors in their string by using reconciliation protocol. Direct reconciliation (DR) is the scheme in which Bob uses Alice's encoding string to prepare the key while reverse reconciliation (RR) is when Alice prepares the key based on Bob's decoding result. Alice and Bob use a reconciliation protocol to achieve privacy amplification to reduce the knowledge stolen by Eve [61]. In this work, we use an asymptotic secret key rate to study the performance of RR protocol in mm-waves and THz QKD. In RR it is possible to achieve a positive secret key rate when the channel transmissivity is almost 0, while in DR it requires a channel transmissivity larger than 0.5 [99], and is impractical in mm-waves and THz because of the high losses (both atmospheric absorption and path).

According to [61], the secret key rate of the MIMO system could be divided into *r* SISO channels. So we first analyse the secret key rate of a SISO channel. In the RR scheme, Alice and Bob use the decoding outcomes from Bob's side to generate their secret key [96]. Alice and Bob could estimate the mutual information they shared, described as $I(a:b)$, and the accessible information of Eve, described as $I(E:b)$. The asymptotic secret key rate $R^{\blacktriangleleft}$ could be described by the surplus information shared by Alice and Bob and is given by [54]

$$R^{\blacktriangleleft} = I(a:b) - I(E:b) \tag{10}$$

The mutual information between Alice and Bob is

$$\mathrm{I(a:b)} = \frac{1}{2} log_2[1 + \frac{tV_s}{\Lambda(V_0, W)}] \tag{11}$$

$$\Lambda(\mathrm{x,y}) = t\mathrm{x} + (1-t)\mathrm{y} \tag{12}$$

Here, *t* is the transmissivity of the channel, $V_s$ is the variance of the initial signal encoding, $V_0$ is the variance of the thermal state, and $W$ is the variance of the thermal noise introduced by Eve. In Eq.(11), $V_s \gg V_0, W$, and Eve's information is bounded by the Holevo information $\mathrm{I(E:b)}$ which is defined as

$$\mathrm{I(E:b)} = H_E - H_{E|b} \tag{13}$$

where $H_E$ and $H_{E|b}$ are the von Neumann entropy of Eve's total and conditional state given by Eq. (25) and Eq. (26) in Appendix A, respectively [61, 97].

The total secret key rate is finally given by the sum of *r* SISO links' secret key rate [61], assuming $t_i \to 0$

$$R_{MIMO}^{\blacktriangleleft} = \sum_{i=1}^{r} R_i^{\blacktriangleleft} \approx \zeta tr(\boldsymbol{H}^{\dagger}\boldsymbol{H}) - rh(W) \tag{14}$$

where $tr(\boldsymbol{H}^{\dagger}\boldsymbol{H}) = \sum_{i=1}^{r} t_i$, $t_i$ is the $i$-th transmissivity of the channel. And

$$\zeta = 0.72\left[\frac{V_s}{W} - \ln\left(\frac{V_a+1}{V_a-1}\right)\left(\frac{V_a^2 - W^2}{2W} - V_a\right)\right] \tag{15}$$

The function $h(W)$ in Eq. (14) is defined by the following general form $h$(x), where x is a variable:

$$h(\mathrm{x}) = \frac{x+1}{2} log_2\left(\frac{x+1}{2}\right) - \frac{x-1}{2} log_2\left(\frac{x-1}{2}\right) \tag{16}$$

$W$ is the variance of the thermal noise introduced by Eve, $V_s$ is the variance of the initial signal encoding, $V_a$ is given by Eq. (1)-(3).

The analysis in this work considers an idealised Eve with access to cryogenic quantum memory and low-noise hardware, corresponding to a low thermal-noise variance $W$. For a non-cryogenic Eve, the increased thermal photon number at THz frequencies leads to a much larger $W$, introducing additional thermal noise that affects both the Alice–Bob correlation and Eve's accessible information. Moreover, when $W>>V_0$, Eve can no longer remain indistinguishable from the cryogenic background noise, since this condition requires $W=V_0$. In practice, the operating temperature, cooling capability, and thermal-noise performance of Eve's quantum memory and associated hardware therefore impose additional constraints on the implementation of such an attack. Therefore, a cryogenic Eve with low thermal noise is considered in this work to evaluate the secure performance of the THz QKD system under a more challenging eavesdropping condition.

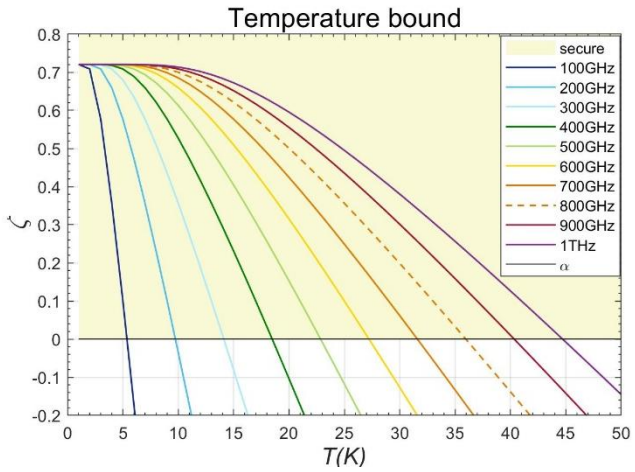



**Fig. 2.2.** The curves show $\zeta$ as a function of temperature for different frequencies. To achieve secure transmission, $\zeta$ should keep above line $\alpha$ (locate in the secure range).

### 2.3.3 System condition

To achieve a positive secret key rate $R_{MIMO}^{\blacktriangleleft} > 0$, $\zeta tr(\boldsymbol{H}^{\dagger}\boldsymbol{H}) > rh(W)$ is required from Eq. (14). Verified from Eq. (1)-(4), only $\zeta tr(\boldsymbol{H}^{\dagger}\boldsymbol{H})$ in Eq. (14) depends on frequency, and $\zeta$ also depends on temperature. With a given frequency, lower temperature could decrease $V_0$, corresponding to Eq.(1)-(3) and therefore increase $\zeta$ in Eq. (15). This also happens with a given temperature and increasing frequency. But higher frequency normally brings higher path loss which may decrease $tr(\boldsymbol{H}^{\dagger}\boldsymbol{H})$. Since $tr(\boldsymbol{H}^{\dagger}\boldsymbol{H})$>0, the limit of $\zeta > \alpha = \frac{rh(W)}{tr(\boldsymbol{H}^{\dagger}\boldsymbol{H})}$ is equal to $\zeta > \alpha = 0$ while $W$=1. This condition helps us find the balance between $\zeta$ and $tr(\boldsymbol{H}^{\dagger}\boldsymbol{H})$ and get a positive secret key rate.

Figure 2.2 shows $\zeta$ as a function of temperature $t_e$ for different frequencies in a MIMO THz QKD system based on Eqs. (1)-(3) and (15) [61]. According to the simulation results, we achieved secure transmission for frequencies between $f$=100GHz and 1THz, at temperatures $T$< 43K. The details of the maximum operating temperature for each frequency calculated from Eq. (1)-(3) and (15) are shown in Table 1.

TABLE I

| Frequency | Atmospheric absorption $\delta$ | Maximum temperature $T_{max}$ (K) | Distance of 32×32 MIMO system at $T_{max}$ (m) |
|---|---|---|---|
| 100GHz | 0.4dB/km | 4 | 700 |
| 200GHz | 3dB/km | 8 | 320 |
| 300GHz | 4dB/km | 13 | 75 |
| 400GHz | 20dB/km | 17 | 86 |
| 500GHz | 50dB/km | 21 | 68 |
| 600GHz | 150dB/km | 26 | 26 |
| 700GHz | 70dB/km | 30 | 38 |
| 800GHz | 100dB/km | 35 | 36 |
| 900GHz | 100dB/km | 39 | 25 |
| 1THz | 100dB/km | 43 | 21 |

## 2.4 Simulation result

We use the secret key rate ($R$) to define whether the system is safe or not. A positive secret key rate reflects a safe transmission. As $R$ of the MIMO system is the sum of the SISO systems, we also compared the different performances of the MIMO and SISO systems at the same conditions.

### 2.4.1 Simulation of the MIMO system

According to [51], [52], [100], the atmospheric absorption for each frequency is shown in Table 1. We assume the target of the secret key rate is $10^{-5}\ bit/use$ [61]. Table 1 also shows the distance of 32×32 MIMO system at maximum temperature for each frequency. While $f$=700GHz and $f$=800GHz could reach more than 35m at $T$>30K, $f$=600GHz could only get to 26m at a lower temperature because of higher absorption at this frequency. Figure 2.3 (a) and (b) shows the secret key rate as a function of secure transmission distance for frequencies from $f$=100GHz to 1THz at $T$=4K in a 32×32 MIMO system. The distance of $f$=100GHz and $f$=200GHz could achieve $d$=700m at $T$=4K, which is the maximum through all frequencies. The secure distance for $f$=300GHz could get to $d$=500m,

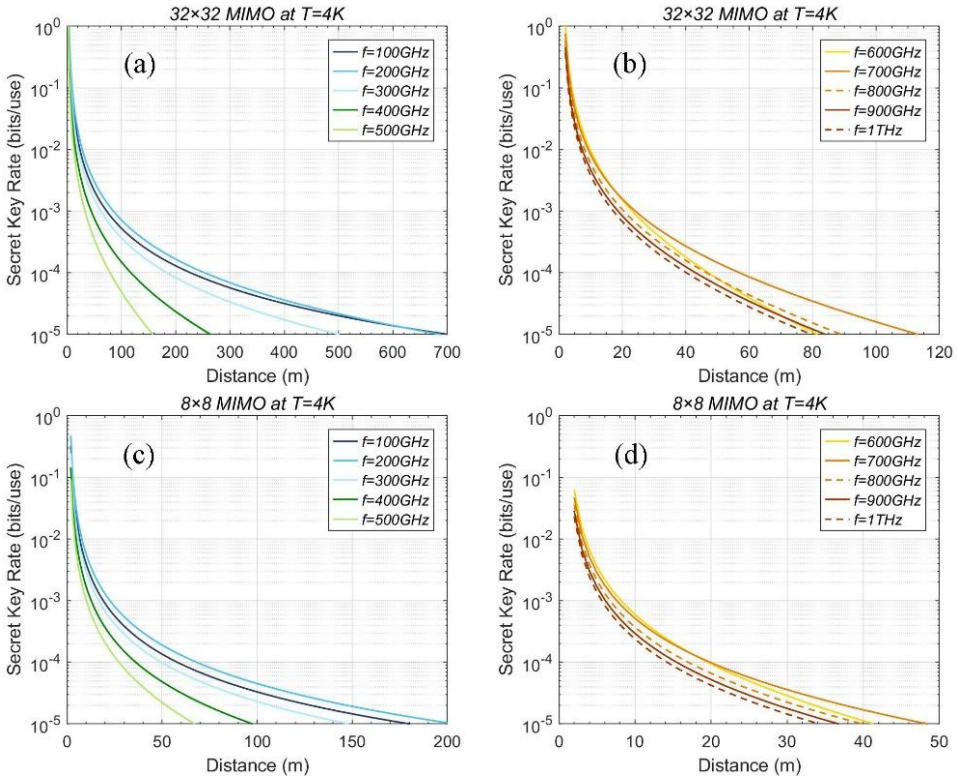



**Fig. 2.3.** (a) The transmission distance of a 32×32 MIMO system for $f$=100GHz to 500GHz at $T$=4K. (b) The transmission distance of a 32×32 MIMO system for $f$=600GHz to 1THz at $T$=4K. (c) The transmission distance of an 8×8 MIMO system for $f$=100GHz to 500GHz under $T$=4K. (d) The transmission distance of an 8×8 MIMO system for $f$=600GHz to 1THz under $T$=4K. Here, parameters are $G_a$=30, $W$=1, $V_a$=1000.

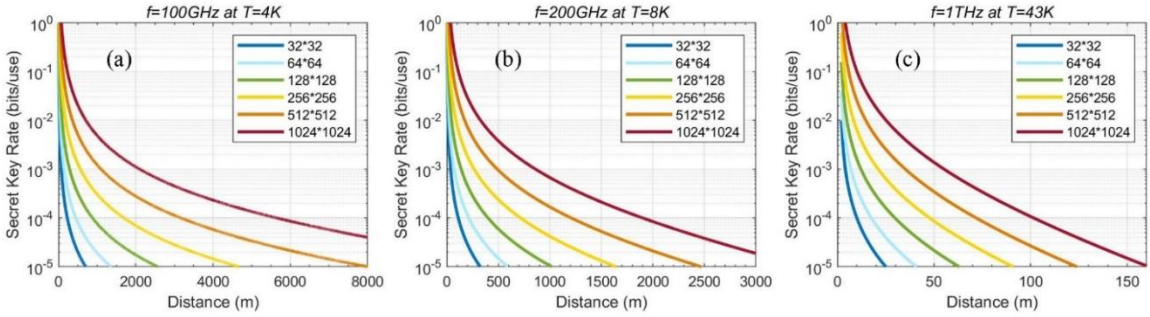



**Fig. 2.4.** The curves show the secret key rate as a function of transmission distance for the different numbers of antennas in MIMO systems. (a) is the result for $f$=100GHz, at $T$=4K. (b) is the result for $f$=200GHz, at $T$=8K. and (c) is the result for $f$=1THz, at $T$=43K.

but it will drop to under $d$=160m for frequencies above $f$=500GHz. If the number of antennas reduces to 8×8, the maximum distance could still reach $d$=200m for $f$=200GHz as shown in Fig. 2.3 (c). But for frequencies above $f$=600GHz in Fig. 2.3 (d), the distances are all below 50m because of the high absorption.

High MIMO configuration could enhance the maximum secure distance as shown in Fig. 2.4. While the maximum distance is $d$=700m for a 32×32 MIMO system, the secure transmission could achieve much more than $d$=8000m for a 1024×1024 MIMO at $f$=100GHz at $T$=4K as shown in Fig. 2.4 (a). The same trend could be found for $f$=200GHz at $T$=8K and $f$=1THz at $T$=43K. For $f$=200GHz, the maximum distance is more than $d$=3000m for 1024×1024 MIMO at $T$=8K. But secure distances for $f$=1THz at $T$=43K are not as much shorter because of the high channel loss caused by atmospheric absorption and thermal noise. It could only get to 160m with a 1024×1024 MIMO antenna system at $T$=43K. And compared with Fig. 2.3(b), the distance for $f$=1THz at $T$=43K is just one-fifth of $T$=4K, with 32×32 antennas.

### 2.4.2 Simulation of the SISO system

Compared with a large MIMO scheme, the maximum distance of a SISO scheme is shorter at frequency range between $f$=100 GHz and $f$=1THz. We assume the target secret key rate is $10^{-5}\ bit/use$ [61]. Figure 2.5 shows the results obtained from Eq. (15) with $r$=1, corresponding to a SISO system. Figure 2.5 (a) shows that the maximum distance in the SISO system is less than 12m for $f$=200GHz at $T$=8K, which is much less than what is observed in a MIMO system shown in Fig. 2.4 (b). Figure 2.5 (b) shows the distance for $f$=100GHz-1THz in a SISO scheme at $T$= 4K. We could find that the maximum distance decreases with higher frequency at 200GHz-1THz range, caused by the path loss. Comparing Figs. 2.5 (a) and (b), it is obvious that lower temperature increases the maximum distance for the same frequency.

Comparing Fig. 2.5 (b) with Fig. 2.3, we find that at the same temperature, the MIMO scheme could achieve a longer distance than the SISO scheme. So it is necessary to use multiple antennas in mm-wave and THz QKD systems. As frequencies $f$=800GHz, $f$=900GHz, and $f$=1THz have the same atmospheric absorption, Fig. 2.5 (b) shows that the transmission distance improved by the lower frequencies. This may be caused by the

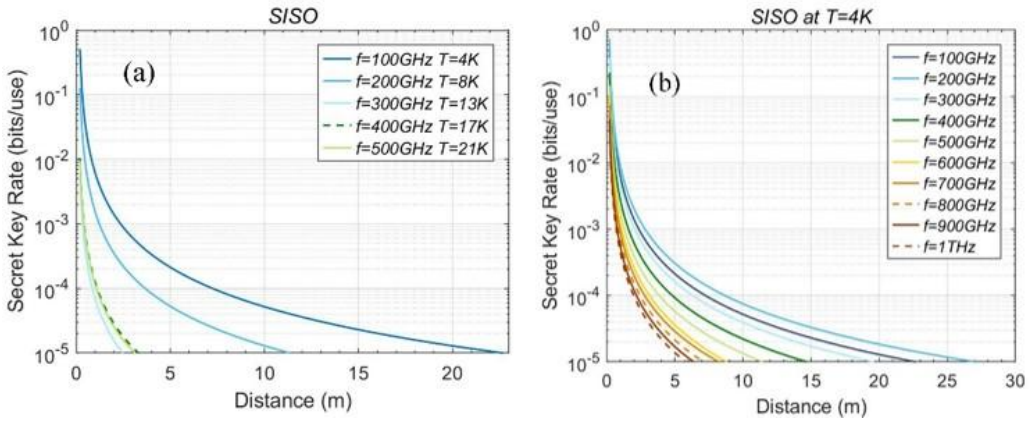



**Fig. 2.5.** (a) The secret key rate R as a function of transmission distance for SISO for frequency ranges between *f*=100GHz and *f*=500GHz at the highest operational temperature. Atmospheric absorptions in the channel are shown in table 1. (b) The secret key rate R as a function of transmission distance for SISO for frequency ranges between *f*=100GHz and *f*=1THz at *T*=4K.

increase of $tr(\boldsymbol{H}^{\dagger}\boldsymbol{H})$ as lower frequencies have less free-space path loss and matter more than the increase of $V_0$ (which in turn decreases $\zeta$) at this range. As a result, to enhance the secure distance, we could use more antennas, cool down the temperature or choose lower frequencies.

## 2.5 Discussion

We study through simulations of MIMO CVQKD protocol on mm-waves to THz open-air link with an ideal LOS path and crosstalk-free antennas. The influences of cryogenic operating temperature for THz circuits and the number of antennas are considered. Although the simulation results indicate that secure wireless communication is achievable and show a nice transmission range, the hardware realisation and complex channel loss of the proposed system should be discussed.

We assumed the perfect quality of the beam-splitter and communication channel in this study. Although the MIMO array may overcome high path loss by using proper beamforming protocol and reduce the interference by using highly-directional antennas [101], for the realisation of the THz CVQKD in the future, except for the channel loss

caused by atmospheric absorption, the co-channel interference, inter-cell interference, non-line-of-sight path, and multipath effect all should be considered in the channel loss [102, 103].

Recently, devices for mm-waves to THz frequency range based on different kinds of superconductors operating at temperatures from 4K to 77K [15], such as efficient emitters [20], THz photonic circuits [41], have been proposed, which could be the possible solution for building the cryogenic mm-wave to THz quantum communication link. The superconducting-based coherent THz source has been reported to generate high-power THz radiation(around 0.5μW) below 50K [67], that abandon the complicated terahertz-optics conversion and is suitable for on-chip THz transmission. Recent terahertz hybrid circuit cavities show the opportunity of the realisation of ultrasensitive THz detectors at 20K [104].

Even so, there are still many research efforts to be performed to accomplish the whole scheme in practical hardware. For example, highly directional antennas or sources for THz on-chip circuits are one of the important foundations to against interference and achieve long-distance communication. THz detector without optical-terahertz conversion may increase the flexibility and efficiency of the communication. As the optical CVQKD has been realised and proved to be achievable with megabits per second (Mbps) rate over kilometres [105, 106], we believe the mm-waves to THz CVQKD system is not so far from accomplishment.

## 2.6 Conclusion

In this work, we first time developed the study of SISO and MIMO QKD schemes in mm-waves and THz frequency ranges, from $f$= 0.1 to $f$= 1 THz, with the cryogenic operation of sources and detectors below 50K. We found that a positive secret key rate can be observed

at the targeted frequency range. MIMO technology could improve the secure transmission distance compared with the SISO scheme. Moreover, we showed that the more antennas are in the system, the longer the transmission distance can be achieved. To build a long-way secure communication channel, more antennas, low-temperature operation and lower frequencies are required. We also discussed the practical hardware realisation possibility of the cryogenic mm-waves and THz system, and have given our views on the development direction in both experimental and theoretical aspects for the mm-waves and THz QKD field. Our work may guide the effort in the development of next-generation secure wireless communication systems and the establishment of quantum internet for applications, from satellites to indoor and short-distance communications.

## 2.7 Appendix A

### 2.7.1 Computation of channel model

The channel matrix between Alice and Bob could be modelled as Eq. (4)

$$\boldsymbol{H} = \sum_{l=1}^{L} \sqrt{\gamma_l} e^{j2\pi f_c \tau_l} \psi_{N_r}(\phi_{r,LOS}) \psi_{N_t}^{\dagger}(\phi_{t,LOS})$$

where, $\boldsymbol{H} \in \mathbb{C}^{N_r \times N_t}$, $L$ is the full number of multipath components, $\tau_l$ is the propagation delay of the $l$-th multipath. The path loss $\gamma_l$ for the line-of-sight (LOS) path ($L$=1) is given by Eq. (5)

$$\gamma_{l=1} = G_t G_r \left(\frac{\lambda}{4\pi d}\right)^2 10^{-\frac{\delta d}{10}}$$

where $d$ is the distance (km) between Alice and Bob and $\delta$ is the atmospheric loss. $\phi_{r,LOS}$ and $\phi_{t,LOS}$ is the angle of arrival seen by Bob, and the angle of departure from Alice,

respectively. $\psi_K(\theta)$ represents the array response vector of a ULA which contains *K* number of antennas [61]:

$$\psi_K(\theta) = \frac{1}{\sqrt{K}}\left[1, e^{j2\pi\frac{d_a}{\lambda}sin\theta}, \dots, e^{j2\pi\frac{d_a}{\lambda}(K-1)sin\theta}\right]^T \tag{17}$$

Here, $d_a$ and $\lambda$ denote the inter-antenna spacing and wavelength of the carrier signal, respectively. We assume $d_a = \frac{\lambda}{4}$ in this work. The channel model could be described by a singular-value decomposition (SVD) scheme introduced by Ref. [61]:

$$\boldsymbol{H} = \boldsymbol{U}\boldsymbol{\Sigma}\boldsymbol{V}^{\dagger} \tag{18}$$

Here, $\boldsymbol{U} \in \mathbb{C}^{N_r \times N_r}$ and $\boldsymbol{V} \in \mathbb{C}^{N_t \times N_t}$ are unitary matrices represent *K* phase shifters [91], and $\boldsymbol{\Sigma}$ is given as

$$\boldsymbol{\Sigma} = \begin{bmatrix} diag\{\sqrt{\eta_1}, \dots, \sqrt{\eta_r}\} & \mathbf{0}_{r\times(N_t-r)} \\ \mathbf{0}_{(N_r-r)\times r} & \mathbf{0}_{(N_r-r)\times(N_t-r)} \end{bmatrix} \tag{19}$$

where *r* is the rank of $\boldsymbol{H}$ and $\sqrt{\eta_1}, \dots, \sqrt{\eta_r}$ are the *r* non-zero singular values of $\boldsymbol{H}$ generated by the transmissivity of beam-splitters in the system [91].

As shown in Fig.2.1 (b), the whole model of a MIMO system could be described by [61, 91]

$$\hat{\boldsymbol{a}}_B = \boldsymbol{U}^{\dagger}\boldsymbol{H}\boldsymbol{V}\hat{\boldsymbol{a}}_A + \boldsymbol{U}^{\dagger}\boldsymbol{U}\boldsymbol{S}\hat{\boldsymbol{a}}_E \tag{20}$$

where $\hat{\boldsymbol{a}}_B = [\hat{a}_{B,1}, \ldots, \hat{a}_{B,N_r}]^T$ is the received mode of Bob, $\hat{\boldsymbol{a}}_A = [\hat{a}_{A,1}, \ldots, \hat{a}_{A,N_t}]^T$ is the transmitted mode of Alice, $\hat{\boldsymbol{a}}_E = [\hat{a}_{E,1}, \ldots, \hat{a}_{E,N_t}]^T$ is the injected Gaussian mode of Eve.

$$\boldsymbol{S} = diag\{\sqrt{1-\eta_1}, \ldots, \sqrt{1-\eta_r}, \mathbf{1}_{(M-r)\times 1}\} \tag{21}$$

is a diagonal matrix with $M = \min(N_t, N_r)$. We get $\boldsymbol{U}^\dagger \boldsymbol{U} = \boldsymbol{I}_{N_r}$ and $\boldsymbol{V}^\dagger \boldsymbol{V} = \boldsymbol{I}_{N_t}$ as $\boldsymbol{U}$ and $\boldsymbol{V}$ are unitary matrices. Considering Eq. (18) $\boldsymbol{H} = \boldsymbol{U}\boldsymbol{\Sigma}\boldsymbol{V}^\dagger$, diagonal matrix $\boldsymbol{\Sigma}$ and $\boldsymbol{S}$, Eq. (20) would turn to $\hat{\boldsymbol{a}}_B = \boldsymbol{U}^\dagger \boldsymbol{U}\boldsymbol{\Sigma}\boldsymbol{V}^\dagger \boldsymbol{V}\hat{\boldsymbol{a}}_A + \boldsymbol{U}^\dagger \boldsymbol{U}\boldsymbol{S}\hat{\boldsymbol{a}}_E = \boldsymbol{\Sigma}\hat{\boldsymbol{a}}_A + \boldsymbol{S}\hat{\boldsymbol{a}}_E$. So the efficient channel between Alice and Bob can be disintegrated into *r* parallel SISO channels.

To accomplish the proposed SVD-based beamforming and combining in the MIMO THz CV-QKD system, the right singular vectors in V can be used as transmit beamforming vectors, while the corresponding left singular vectors in U can be used as receive combining vectors. For single-mode transmission, the singular vectors corresponding to the largest singular value can be selected to maximise the effective channel gain. In practical implementation, these beamforming and combining weights can be realised through digital signal processing and appropriate amplitude and phase control in the THz front-end. It is important to distinguish these spatial beamforming weights from the quadratures that carry the continuous-variable quantum information. The beamforming operation determines how the same quantum state is distributed across the antenna array, while the quadratures remain the quantum variables used for modulation and detection. Therefore, the resulting parallel SISO channels can be treated as effective channels for subsequent CV-QKD parameter estimation and secret-key-rate analysis.

Bob randomly chooses quadratures for his input and performs homodyne measurements. Then the input-output relationship of the *i*-th parallel channel between Bob's received

quadrature $\hat{X}_{B,i}$, and Alice's transmitted quadrature $\hat{X}_{A,i}$, can be written by a generic quantum channel as [61]

$$\hat{X}_{B,i} = \sqrt{t_i}\hat{X}_{A,i} + \sqrt{1-t_i}\hat{X}_{E,i}, \qquad i = 1,2,\dots,r \tag{22}$$

with $t_i$ and $\hat{X}_{E,i}$ as transmittance, and Eve's excess noise quadrature, respectively. We can write for Eve's ancilla mode:

$$\hat{X}_{E',i} = -\sqrt{1-t_i}\hat{X}_{A,i} + \sqrt{t_i}\hat{X}_{E,i}, \qquad i = 1,2,\dots,r \tag{23}$$

### 2.7.2 Computation of the secret key rate

The secret key rate $R^{\blacktriangleleft} = I(a:b) - I(E:b)$ is given defined by mutual information. Assuming Gaussian statistic for simulating purposes, the mutual information between Alice and Bob is

$$\mathrm{I(a:b)} = \frac{1}{2} log_2[1 + \frac{tV_s}{\Lambda(V_0, W)}]$$

$$\Lambda(\mathrm{x},\mathrm{y}) = t\mathrm{x} + (1-t)\mathrm{y}$$

Here, $t$ is the transmissivity of the channel, $V_s$ is the variance of the initial signal encoding, $V_0$ is the variance of the thermal state, and $W$ is the variance of the thermal noise introduced by Eve. And Eve's information is bounded by the Holevo information $\mathrm{I(E:b)}$, which is defined as

$$\mathrm{I(E:b)} = H_E - H_{E|b} \tag{24}$$
$$H_E = h(v_1) + h(v_2) \tag{25}$$
$$H_{E|b} = h(v_3) + h(v_4) \tag{26}$$

where $H_E$ and $H_{E|b}$ are the von Neumann entropy of Eve's total and conditional state respectively [61, 97]. The von Neumann entropy depends on the symplectic eigenvalues is given by [61]

$$v_1 = \Lambda(\mathrm{W}, V_a), v_2 = \mathrm{W}, \tag{27}$$

$$v_3, v_4 = \sqrt{\frac{1}{2}(\Delta \pm \sqrt{\Delta^2 - 4\Upsilon})}, \tag{28}$$

and

$$\Delta = \frac{V_a W \Lambda(W, V_a) + W\Lambda(WV_a, 1)}{\Lambda(V_a, W)} \tag{29}$$

$$\Upsilon = \frac{V_a W^2 \Lambda(W, V_a)\Lambda(WV_a, 1)}{\Lambda^2(V_a, W)} \tag{30}$$

The function $\mathrm{h(x)}$ is defined as

$$\mathrm{h(x)} = \frac{x+1}{2} log_2\left(\frac{x+1}{2}\right) - \frac{x-1}{2} log_2\left(\frac{x-1}{2}\right) \tag{31}$$

# Chapter 3
# Orthogonal Frequency Division Multiplexing Continuous Variable Terahertz QKD for Large-Scale Wireless Quantum Communication

**Publication statement:** *©2026 IEEE. Reprinted, with permission, from [M. Zhang and K. Delfanazari, "Orthogonal Frequency-Division Multiplexing Continuous-Variable Terahertz QKD for Large-Scale Wireless Quantum Communication," in IEEE Transactions on Quantum Engineering, vol. 7, pp. 1-13, 2026, Art no. 4100913, doi: 10.1109/TQE.2026.3669050.]*

## 3.1 Abstract

We introduce a continuous-variable quantum key distribution (CVQKD) protocol that combines orthogonal frequency-division multiplexing (OFDM) with terahertz (THz) carriers to deliver high-throughput and hardware-compatible quantum communication. By distributing quantum states across multiple subcarriers, our approach achieves a step-change in spectral efficiency while mitigating dispersion and atmospheric losses that limit existing optical and microwave CVQKD systems. A full security analysis under collective Gaussian attacks is presented, incorporating realistic noise models for both terrestrial and inter-satellite channels. In terrestrial free-space links, our simulations show secret key rates approaching 72 bits per channel use, with secure distances up to 4.5 m under strong humidity-induced absorption. For inter-satellite links, where propagation losses are

minimal, secure transmission is sustained over >100 km. A distinctive feature of our work is its direct link to practical hardware. We evaluate implementation using emerging on-chip coherent THz sources based on superconducting Josephson junctions. These compact, voltage-tunable emitters provide wideband coherent radiation ideally matched to our protocol, enabling scalable, chip-integrated quantum networks. Incorporating their measured characteristics into our models, we demonstrate secure communication up to 3 m in ambient conditions and ~26 km under cryogenic or vacuum operation. By uniting advanced protocol design, rigorous security modelling, and hardware-driven performance analysis, this work establishes THz CVQKD as a viable and scalable route to next-generation terrestrial and space-based quantum communication.

## 3.2 Introduction

Terahertz (THz) frequency region, located between microwaves and infrared, has caught the attention for its wide range of applications in quantum communication, biomedicine, material science, nondestructive evaluation, and sensing [15, 107, 108]. THz communication has been considered a key enabling technology of next-generation space-air-ground integrated networks, with wide operating bandwidth and high data rate capacity [5, 109]. However, THz hardware, including efficient sources, modulators, resonators, detectors, etc., is the core factor restricting the development of THz communication. Recent advancements in optical-to-THz conversion and compact solid-state THz sources offer promising solutions to bridge the THz gap [15], especially the superconducting coherent THz emitter technology, which offers wideband tunability [65-67], and on-chip frequency modulation with gigahertz bandwidth [110]. Such advanced hardware facilitates the development of THz communication and paves the way for novel applications in THz quantum technology. To enhance the security of THz communication, quantum key distribution (QKD), including both discrete variable (DV) and continuous variable (CV) approaches, is implemented to establish a secure link between two parties [57]. CVQKD is

particularly appealing for THz communication due to its high achievable rates, tolerance to high thermal noise, and compatibility with systems that do not require single-photon components [55, 111]. Recent research has demonstrated that THz CVQKD offers high data rate capacity and reliable wireless transmission in complex environments such as open-air, indoor, and inter-satellite scenarios while ensuring security through quantum cryptography [10, 59]. Furthermore, compared to single-carrier CVQKD protocols, utilising multi-carrier communication protocols has been shown to significantly extend the secure transmission distance and enhance the secret key rate [58, 61]. The multi-carrier protocol, which employs multiple transmitters and receivers, faces limitations in operating temperature within the mm-wave to low THz range and requires complex hardware implementation with on-chip integrated antennas [108]. However, by dividing a single high-speed data stream into multiple low-speed data streams and modulating them onto narrowband orthogonal subcarriers, multicarrier multiplexing (MCM) technology, particularly the orthogonal frequency-division multiplexing (OFDM) scheme, enables parallel key distribution using a single transmitter and receiver while efficiently utilising spectrum resources [62]. Although current research has demonstrated a promising increase in the secret key rate for THz MCM QKD, the underestimation of crosstalk and strong modulation noise introduced during imperfect processes, as well as the neglect of highly variable transmissivity for each subcarrier frequency in practical applications, may result in inaccurate performance estimations. To address this, we have introduced and analysed the impact of additional excess noise and incorporated the absorption coefficient for each subcarrier to more accurately evaluate the practical performance of the OFDM CVQKD scheme in the THz frequency range, bringing it closer to real-world applications. This chapter is organised as follows: Section 3.3 presents the system model of the THz OFDM-based CVQKD protocol and introduces the modulation noise. Section 3.4 analyses the security of the scheme and computes the secret key rate. In Section 3.5, we provide simulation results for open-air, indoor, and inter-satellite environments. Section 3.6 discusses the protocol's performance concerning the latest advancements in THz hardware. Finally, we conclude the chapter in Section 3.7.

## 3.3 System modeling

### 3.3.1 THz OFDM CVQKD protocol

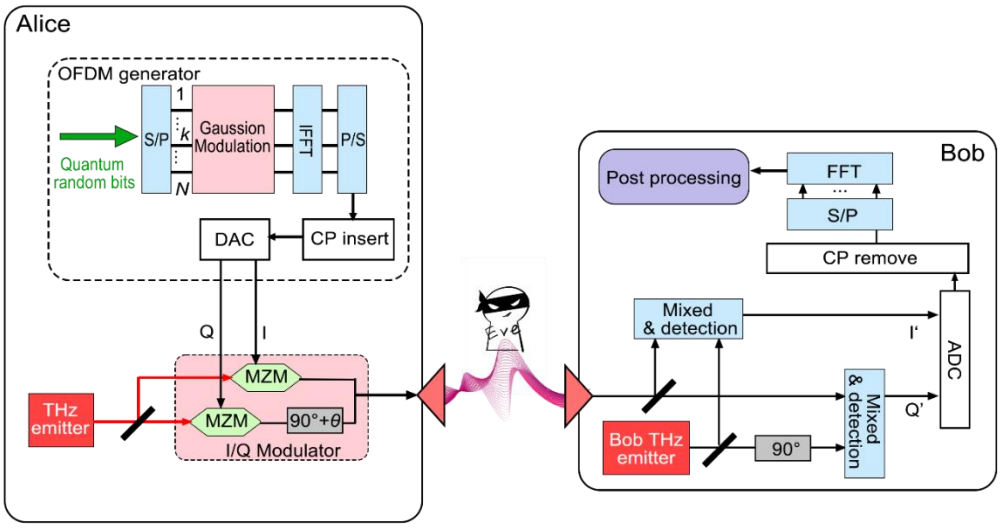



**Fig. 3.1.** The schematic of the THz wireless OFDM-CVQKD system. Components include: MZM (Mach-Zehnder modulator), S/P (serial to parallel conversion), IFFT (inverse fast Fourier transform), P/S (parallel to serial conversion), CP (cyclic prefix), DAC (digital to analogue conversion), ADC (analogue to digital conversion), and FFT (fast Fourier transform).

The THz OFDM-based CVQKD system scheme is illustrated in Fig. 3.1. Alice generates a THz wave with an initial frequency $f_1$ and $N$ equally spaced frequency intervals $\Delta f$ orthogonal in the frequency domain from a THz emitter and then splits the wave into two signals with 90° phase difference. The two signals are fed into the local oscillator ports of two identical mixers, where they are combined with the I and Q signals from the OFDM generator. In the OFDM generator, Alice generates a stream of quantum random bits as vacuum states $|0\rangle$ and employs serial-to-parallel (S/P) conversion to transform the serial stream into $N$-independent parallel bit streams at the baseband. Each bit stream is modulated by a $q/p$-Gaussian modulator with a coherent state $|\alpha\rangle$, resulting in $|\alpha_k\rangle = |q_k + jp_k\rangle, (k = 1,2, \dots, N)$. The quadrature components $q_i$ and $p_i$ are drawn from two independent random variables $Q$ and $P$, both following a normal distribution $Q \sim P \sim N(0, V_{mod})$, where $V_{mod}$ is the modulation noise of the Gaussian distribution. The $N$-modulated

states are then mapped onto their respective subcarrier $f_k=f_1+k\Delta f$ using an inverse Fourier transform (IFFT). The THz carriers are modulated by signals $I_s$ and $Q_s$ defined as [112]

$$I_s = \sum_{k=1}^{N} I_k \cos(2\pi f_k t) - \sum_{k=1}^{N} Q_k \sin(2\pi f_k t) \tag{32a}$$

$$Q_s = \sum_{k=1}^{N} I_k \sin(2\pi f_k t) + \sum_{k=1}^{N} Q_k \cos(2\pi f_k t) \tag{32b}$$

where $N$ is the number of subcarriers, $f_k=f_1+k\Delta f$ is the frequency of $k$-th subcarrier. The cyclic prefix (CP) is inserted into the signal to equalise the time domain at Bob's site, effectively mitigating inter-symbol and inter-channel interference during transmission [113]. Once the real and complex-valued outputs are converted to analogue signals, the encoded multi-carrier quantum state at Alice's side is represented as follows [112]

$$|X_{sig} + jP_{sig}\rangle = \otimes_{k=1}^{N} |X_k + jP_k + \Delta X_k + j\Delta P_k\rangle \tag{33}$$

where $X_k$ and $P_k$ are the modulated quadrature components for the $k$-th subcarrier, with modulation noise $\Delta X_k$ and $\Delta P_k$, respectively. The total variance of the $k$-th quantum mode prepared by Alice is $V_{A(k)}=V_{mod}+V_0$, where $V_0$ is the variance of the vacuum state given by [53]

$$V_0 = 2\bar{n} + 1 \tag{34}$$

with the vacuum shot noise unit (SNU) 1 and the mean thermal photon number

$$\bar{n} = \frac{1}{\exp\left(\frac{hf_k}{k_B T}\right) - 1} \tag{35}$$

where $h$ is Planck's constant, $f_k$ is the frequency, $k_B$ is the Boltzmann constant, and $T$ is the absolute temperature. The modulation noise in a practical OFDM-CVQKD protocol mainly arises from I/Q imbalance, which is caused by differences in signal amplitudes between the in-phase (I) and quadrature (Q) arms of the I/Q modulator. In addition, it is influenced by quadrature skew from the angular error $\theta$ of the 90° phase difference in the local oscillating signal, as well as intermodulation distortion. The quantum signal transmitted to Bob via an open-air, indoor or inter-satellite channel, with potential eavesdropping by Eve, can be written as [112]

$$E_{sig}(t) = 2A_{sig}e^{j2\pi f_A t}\left\{\begin{array}{l} G_1 \sin\left[\sum_{k=1}^{N}\gamma_k \cos(2\pi f_k t+\varphi_k)\right] \\ +jG_2 \sin\left[\sum_{k=1}^{N}\gamma_k \sin(2\pi f_k t+\varphi_k)\right] \end{array}\right\} \tag{36}$$

$$\gamma_k = \mu_k\sqrt{{I_k}^2+{Q_k}^2} \tag{37a}$$

$$\cos\varphi_k = \frac{I_k}{\sqrt{{I_k}^2+{Q_k}^2}} \tag{37b}$$

$$G_1 = \frac{1+\kappa_k e^{j\theta_k}}{2}, G_2 = \frac{1+\kappa_k e^{-j\theta_k}}{2} \tag{37c}$$

where $A_{sig}$ is the amplitude of the signal, $f_A$ is the central frequency of the subcarriers, $G_1$ and $G_2$ are the I/Q imbalance factors, $0 \le \kappa_k \le 1$ is the transmitter gain imbalance, $0 \le \theta_k \le \frac{\pi}{2}$ is the quadrature skew and $\mu_k$ in Eq.(37a) is the modulation index of the $k$-th subcarrier with a given number $\mu_k$=0.01 in the following part. At Bob's site, the received signal is combined with a locally generated signal in a coherent receiver to offset the carrier frequency. The signal is then digitised, the cyclic prefix is removed, and the serial

quantum signal is converted into parallel form. A fast Fourier transform (FFT) is applied for demodulation to recover the signals. Finally, post-processing, including reconciliation and privacy amplification, is performed to finalise the secret keys.

The architecture in Fig. 3.1 represents a general implementation of the IQ modulation and coherent detection processes. In particular, the MZM-based IQ modulator is used as a representative implementation of IQ modulation and does not imply that an optical-fibre link is required for the THz CVQKD system. For THz wireless CVQKD systems, the required signal modulation can be performed in the optical domain before the signal is converted to or coupled to a THz source [114]. For cryogenic THz sources, electrical or microwave modulation provides an alternative implementation route [115]. Dedicated THz modulation hardware remains an important area for further development, particularly for achieving high bandwidth, low loss, and compact integration across the 0.1–1 THz range.

### 3.3.2 Modulation noise

Non-linear devices, such as amplifiers and mixers, can generate additional signals known as intermodulation products, including second-order distortion ($2f$) and third-order distortion ($3f$) from a single frequency, $f$. The amplitude of these distortions decreases with higher orders. When two frequencies pass through a nonlinear component, they mix, producing complex distortions across different orders. While most distortions occur far from the base frequencies $f_1$ and $f_2$, in-band signals from third-order distortion, such as $2f_1$-$f_2$ and $2f_2$-$f_1$, can be close to the fundamental signals and are difficult to eliminate using filters. Third-order distortions may overlap with the fundamental signals for three input frequencies with the same gap $\Delta f$, such as $f_3=f_2+\Delta f=f_1+2\Delta f$. For example, $2f_2$-$f_3=f_1$ and $2f_2$-$f_1=f_3$. In OFDM-based multi-carrier modulation, multiple subcarrier signals with a fixed frequency interval transmit information in parallel. We assume the frequency gap between two subcarriers is $\Delta f$ and use $N$ subcarriers in the system from the fundamental frequency

*f*. We consider the worst-case scenario where the third-order distortions of $f_m$,$f_n$,$f_l$ coincide with the signal $f_k$, when $m$, $n$, $l$, $k$∈[1,$N$].

To estimate the modulation noise, previous work [112] applies the Jacobi-Anger expansion and uses Bessel functions to express the quadrature $X_{sig(k)}$ of the $k$-th subcarrier as

$$\begin{aligned} X_{sig(k)} &= X_k + \Delta X_k \\ &= 2A_{sig}\mu_k I_k + \Delta X_{k1} + \Delta X_{k2} + \Delta X_{k3} \end{aligned} \tag{38}$$

Here, $X_k$ represents the $k$-th subcarrier component without intermodulation distortion or I/Q imbalance ($\kappa_k = 1, \theta_k = 0$), and the extra modulation noise $\Delta X_k$ consists of three parts [112]:

1) The modulation noise from the I/Q imbalance

$$\Delta X_{k1} = A_{sig}\mu_k[(\kappa_k cos\theta_k - 1)I_k + \kappa_k sin\theta_k Q_k] \tag{39a}$$

2) The modulation noise from the third-order intermodulation with $f_k$=2$f_m$-$f_n$ and $f_k$=2$f_m$+$f_n$, with condition $k$=2$m$-$n$ and $k$=2$m$+$n$+2$f$/Δ$f$, respectively

$$\begin{aligned} \Delta X_{k2} = \frac{1}{4}A_{sig}\mu_m^2\mu_n \times \\ \left\{ (1+\kappa_k cos\theta_k) \left\{ \begin{matrix} [M_1(N,k)+M_2(N,k)]Q_m^2 I_n \\ +2[M_1(N,k)-M_2(N,k)]I_m Q_m Q_n \\ -[M_1(N,k)+M_2(N,k)]I_m^2 I_n \end{matrix} \right\} \right. \\ \left. +\kappa_k sin\theta_k \left\{ \begin{matrix} [M_1(N,k)+M_2(N,k)]I_m^2 Q_n \\ +2[M_1(N,k)-M_2(N,k)]I_m Q_m I_n \\ -[M_1(N,k)+M_2(N,k)]Q_m^2 Q_n \end{matrix} \right\} \right\} \end{aligned} \tag{39b}$$

3) The modulation noise from the third-order intermodulation with $f_k$=$f_m$+$f_n$+$f_l$, $f_k$=$f_m$+$f_n$-$f_l$ and $f_k$=$f_m$-$f_n$-$f_l$, with condition $k$=$m$+$n$+$l$+2$f$/Δ$f$, $k$=$m$+$n$-$l$ and $k$= $m$-$n$-$l$ -2$f$/Δ$f$, respectively

$$\Delta X_{k3} = \frac{1}{4} A_{sig} \mu_m \mu_n \mu_l \times \left\{ \begin{array}{c} (1 + \kappa_k cos\theta_k) \times \\ \left\{ \begin{array}{c} [W_1(N,k) - W_2(N,k) + W_3(N,k)] I_m Q_n Q_l \\ +[W_1(N,k) - W_2(N,k) - W_3(N,k)] Q_m I_n Q_l \\ +[W_1(N,k) + W_2(N,k) - W_3(N,k)] Q_m Q_n I_l \\ -[W_1(N,k) + W_2(N,k) + W_3(N,k)] I_m I_n I_l \end{array} \right\} \\ +\kappa_k sin\theta_k \times \\ \left\{ \begin{array}{c} [W_1(N,k) + W_2(N,k) - W_3(N,k)] I_m I_n Q_l \\ +[W_1(N,k) - W_2(N,k) - W_3(N,k)] I_m Q_n I_l \\ +[W_1(N,k) - W_2(N,k) + W_3(N,k)] Q_m I_n I_l \\ -[W_1(N,k) + W_2(N,k) + W_3(N,k)] Q_m Q_n Q_l \end{array} \right\} \end{array} \right\} \quad (39c)$$

Here, $M_1(N,k)$ and $M_2(N,k)$ are the combinatorial numbers of the conditions $k$=2$m$-$n$ and $k$=2$m$+$n$+2$f$/$\Delta f$, respectively. Similarly, $W_1(N,k)$, $W_2(N,k)$, and $W_3(N,k)$ are the combinatorial numbers of the conditions $k$=$m$+$n$+$l$+2$f$/$\Delta f$, $k$=$m$+$n$-$l$, and $k$= $m$-$n$-$l$ -2$f$/$\Delta f$, respectively. The modulation indices $\mu_k$, $\mu_m$, $\mu_n$, and $\mu_l$ correspond to the $k$, $m$, $n$, $l$-th subcarriers and are approximately equal to one another. The quadrature $I_g$ and $Q_g$ ($g$=$k$, $m$, $n$, $l$) are mutually random and independent, sampled from the distribution $Q \sim P \sim N(0, V_{mod})$ with variance $\langle {I_g}^2 \rangle = \langle {Q_g}^2 \rangle = {\sigma_1}^2 = V_{mod}$ and forth moments $\langle {I_g}^4 \rangle = \langle {Q_g}^4 \rangle = {\sigma_2}^2 = 2{\sigma_1}^4$ [112]. Therefore, the variance of $\Delta X_k$ can be described as [112]

$$\langle {\Delta X_k}^2 \rangle = \langle {\Delta X_{k1}}^2 \rangle + \langle {\Delta X_{k2}}^2 \rangle + \langle {\Delta X_{k3}}^2 \rangle \quad (40)$$

$$\langle {\Delta X_{k1}}^2 \rangle = {A_{sig}}^2 {\mu_k}^2 {\sigma_1}^2 ({\kappa_k}^2 + 1 - 2\kappa_k cos\theta_k) \quad (41a)$$

$$\langle {\Delta X_{k2}}^2 \rangle = \frac{{A_{sig}}^2 {\mu_m}^4 {\mu_n}^2}{8} (1 + 2\kappa_k cos\theta_k + {\kappa_k}^2) \times \left\{ \begin{array}{c} [M_1(N,k) + M_2(N,k)]^2 {\sigma_2}^2 {\sigma_1}^2 \\ +2[M_1(N,k) - M_2(N,k)]^2 {\sigma_1}^6 \end{array} \right\} \quad (41b)$$

$$\langle {\Delta X_{k3}}^2 \rangle = \frac{{A_{sig}}^2 {\mu_m}^2 {\mu_n}^2 {\mu_l}^2}{4} (1 + 2\kappa_k cos\theta_k + {\kappa_k}^2) \times [W_1^2(N,k) + W_2^2(N,k) + W_3^2(N,k)] {\sigma_1}^6 \quad (41c)$$

Based on Eq. (40) and (41), the modulation noise of the k-th subcarrier can be expressed as

$$\begin{aligned}\varepsilon_{mod}(k) &= \langle \Delta X_k{}^2 \rangle \\ &= A_{sig}{}^2 \mu_k{}^2 \sigma_1{}^2 (\kappa_k{}^2 + 1 - 2\kappa_k cos\theta_k) \\ &\quad + \frac{A_{sig}{}^2 \mu_k{}^6 \sigma_1{}^2}{8} (1 + 2\kappa_k cos\theta_k + \kappa_k{}^2) \times \\ &\left\{ \begin{matrix} [M_1(N,k) + M_2(N,k)]^2 \sigma_2{}^2 \\ +2 \left\{ \begin{matrix} [M_1(N,k) - M_2(N,k)]^2 \\ +W_1^2(N,k) + W_2^2(N,k) + W_3^2(N,k) \end{matrix} \right\} \sigma_1{}^4 \end{matrix} \right\}\end{aligned} \tag{42}$$

By choosing a lower modulation index $\mu_k$=0.01, an amplitude $A_{sig}$=1, a gain imbalance $\kappa_k$=0.98 and a quadrature $\theta_k$=π/50, $V_{mod}$=100, we show the modulation noise $\varepsilon_{mod}(k)$ of the $k$-th subcarrier in Fig. 3.2 (a) with an example frequency $f$=800GHz, $\Delta f$=5GHz under different total carrier numbers $N$. The highlighted points on each line represent the maximum modulation noise in the $N$-subcarrier system, defined as $\varepsilon_{mod}(k_{worst})$. It is evident that the middle subcarriers experience higher modulation noise, and the modulation noise level across all subcarriers increases as the total carrier number grows. Figure 3.2 (b) further demonstrates the exponential growth of the $\varepsilon_{mod}(k_{worst})$ as more subcarriers are used in the protocol. The maximum modulation noise grows significantly from $N$=10 and reaches 27 SNU at $N$=120, making it too large to ignore. Therefore, it is essential to account for the modulation noise at Alice's site.

The modulation noise is considered as part of the excess noise at Alice's side [116]. In multi-carrier CVQKD, the modulation noise $\varepsilon_{mod}(k)$ represents extra noise added to the excess noise $\varepsilon_{single}$ of a single-carrier CVQKD scheme. Consequently, the total excess noise of the $k$-th subcarrier can be written as [112]

$$\varepsilon_{multi}(k) = \varepsilon_{single}(k) + \varepsilon_{mod}(k) \tag{43}$$

where, $\varepsilon_{single}(k)$ represents the loss-induced vacuum noise associated with the transmissivity $T_{ch}(k)$ of the $k$-th subcarrier frequency [117]

$$\varepsilon_{single}(k) = \frac{1 - T_{ch}(k)}{T_{ch}(k)} \tag{44}$$

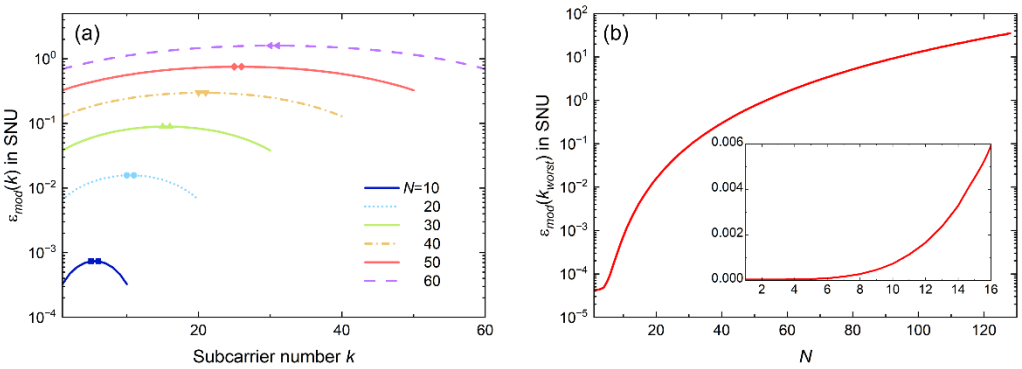



**Fig. 3.2.** (a) Simulated modulation noise $\varepsilon_{mod}(k)$ of the $k$-th subcarrier with $N$ ranging from 10 to 60. The solid points on each line indicate the maximum modulation noise achieved by the $k_{worst}$-th subcarrier among the $N$ subcarriers. (b) Worst modulation noise $\varepsilon_{mod}(k_{worst})$ of the $k_{worst}$-th subcarrier across $N$ subcarriers. The inset is the zoomed-in view for smaller values of $N$.

## 3.4 Secret key rate

To evaluate the security and achievable distance of the THz OFDM CVQKD scheme, we compute the secret key rate (SKR) $R$ using reverse reconciliation in this section. The multi-carrier scheme is considered an $N$-independent orthogonal transmission occurring simultaneously [62, 118]. Hence, the secret key rate of the OFDM CVQKD system is the sum of the secret key rates of the $N$ subcarriers given by [61]

$$R_{OFDM} = \sum_{k=1}^{N} R_k \tag{45}$$

For the *k*-th subcarrier, the secret key rate (bits/channel use) quantifies the extra private information shared by Alice and Bob compared to the information accessible to Eve. It is expressed as

$$R_k = \beta I_{AB_k} - I_{BE_k}$$

where $I_{AB_k}$ is the Shannon mutual information between Alice and Bob, $I_{BE_k}$ is the accessible information of Eve bounded by the Holevo information, and $\beta$=1 represents the efficiency of reverse reconciliation. The mutual information is defined as [53]

$$I_{AB_k} = \frac{1}{2} log_2 \frac{V_b}{V_{b|a}} \tag{46a}$$

where $V_b$ is the variance of Bob's mode and is given by

$$V_b = \eta T_{ch}(V_A + \varepsilon_{multi}) + \eta(1 - T_{ch})W + (1 - \eta)S \tag{46b}$$

where the detection efficiency $\eta$=0.1 and the trusted thermal noise at Bob's site is $S$=1 [53]. The conditional variance is similar to Eq. (46b) but with the Gaussian modulation variance $V_{mod}$=0, yielding: $V_{b|a} = \eta T_{ch}(V_0 + \varepsilon_{multi}) + \eta(1 - T_{ch})W + (1 - \eta)S$. Here, the total excess noise $\varepsilon_{multi}$ in both $V_b$ and $V_{b|a}$ are following Eq. (43) and related to the modulation noise $\varepsilon_{mod}$ we discussed in Section II for each subcarrier.

We assume Eve employs a collective entangling cloner attack, the most powerful and practical attack against Gaussian protocol in the channel. The thermal noise $W$ is injected by Eve using her two-mode squeezed state. Eve's information about Bob's measurement, derived from the Holevo bound is $I_{BE_k} = S_{E_k} - S_{E|B_k}$ with the von Neumann entropy

$$S = \sum h(x) \tag{47a}$$

$$h(x) = \frac{x+1}{2} log_2 \frac{x+1}{2} - \frac{x-1}{2} log_2 \frac{x-1}{2} \tag{47b}$$

where $x$ represents the symplectic eigenvalues of the covariance matrix. After transmission, the covariance matrix for Eve's information in the $k$-th subcarrier is given by

$$\mathbf{V}_{E_k} = \begin{bmatrix} W\mathbf{I} & \sqrt{T_{ch_k}(W^2-1)}\mathbf{Z} \\ \sqrt{T_{ch_k}(W^2-1)}\mathbf{Z} & [(1-T_{ch_k})V_{A_k} + T_{ch_k}W]\mathbf{I} \end{bmatrix} \tag{48}$$

where **I**=diag(1,1), **Z**=diag(1,-1). We set $a = W$, $b = (1-T_{ch_k})V_{A_k} + T_{ch_k}W$, and $c = \sqrt{T_{ch_k}(W^2-1)}$. The symplectic eigenvalues $v_1$ and $v_2$ for the two-mode covariance matrix $\mathbf{V}_{E_k}$ can be calculated from $v=|i\mathbf{\Omega}\mathbf{V}_{E_k}|$, with $\mathbf{\Omega}$ defining the symplectic form given by $\Omega := \bigoplus_{k=1}^{n} \begin{pmatrix} 0 & 1 \\ -1 & 0 \end{pmatrix}$ and $\oplus$ is the direct sum denoting adding matrices on the block diagonal [119]. The symplectic eigenvalues can be described as

$$v_{1,2} = \frac{1}{2}[z \pm (a-b)] \tag{49}$$

where $z = \sqrt{(a+b)^2 - 4c^2}$ [119].

The conditional covariance matrix for Eve's information in the $k$-th subcarrier can be calculated from

$$\mathbf{V}_{E|B_k} = \mathbf{V}_{E_k} - {V_{B_k}}^{-1}\mathbf{D}\mathbf{\Pi}\mathbf{D}^{\mathrm{T}} \tag{50}$$

with

$$\mathbf{D} = \begin{pmatrix} X\mathbf{I} \\ Y\mathbf{Z} \end{pmatrix}, \mathbf{\Pi} \coloneqq \begin{pmatrix} 1 & 0 \\ 0 & 0 \end{pmatrix} \tag{51}$$

where $X = \sqrt{\eta T_{ch_k}(1 - T_{ch_k})(W - V_{A_k})}$ and $Y = \sqrt{\eta(1 - T_{ch_k})(W^2 - 1)}$ [58, 97, 119]. $V_{B_k}$ can be calculated from Eq. (46b) for the k-th subcarrier. Using Eq. (50), Eve's conditional covariance matrix can be written as

$$\mathbf{V}_{E|B_k} = \begin{pmatrix} \mathbf{A} & \mathbf{C} \\ \mathbf{C}^{\mathrm{T}} & \mathbf{B} \end{pmatrix} \tag{52}$$

where

$$\mathbf{A} = \begin{pmatrix} b - \dfrac{X^2}{V_{B_k}} & 0 \\ 0 & b \end{pmatrix}, \mathbf{B} = \begin{pmatrix} a - \dfrac{Y^2}{V_{B_k}} & 0 \\ 0 & a \end{pmatrix},$$
$$\mathbf{C} = \begin{pmatrix} c - \dfrac{XY}{V_{B_k}} & 0 \\ 0 & -c \end{pmatrix} \tag{53}$$

The symplectic eigenvalues $v_3$ and $v_4$ of the matrix in Eq.(52) are given by [97, 119]

$$v_{3,4} = \sqrt{\frac{\Delta \pm \sqrt{\Delta^2 - 4 \det \mathbf{V}_{E|B_k}}}{2}} \tag{54}$$

where $\Delta \coloneqq \det \mathbf{A} + \det \mathbf{B} + 2 \det \mathbf{C}$ and det denote the determinant. Finally, the mutual information between Eve and Bob using Eq.(46b), (49), and (54) is

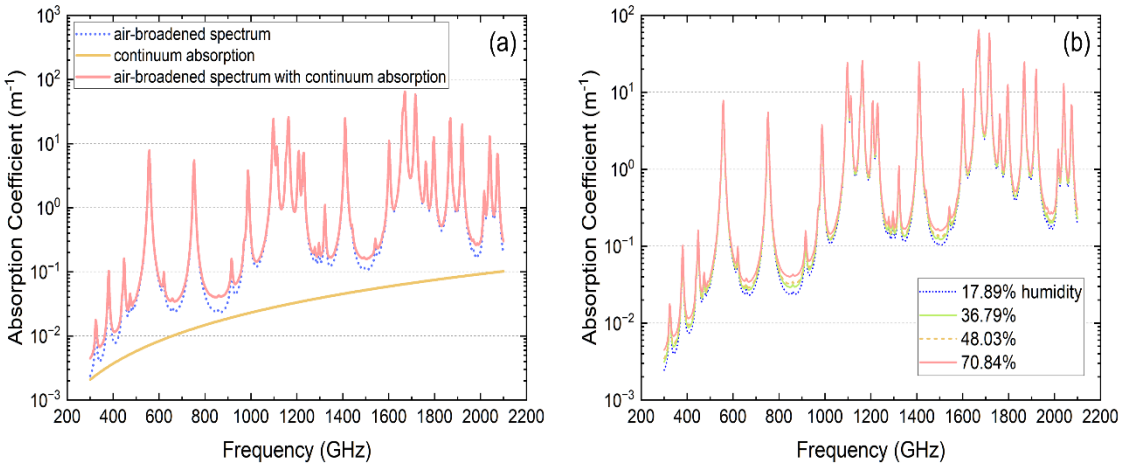



**Fig. 3.3.** (a) Simulated air-broadened spectrum and continuum absorption at 70.84% relative humidity and room temperature. (b) Simulated air-broadened spectrum with continuum absorption for relative humidity levels of 17.89%, 36.79%, 48.03%, and 70.84% at room temperature.

$$I_{BE_k} = S_{E_k} - S_{E|B_k} = h(v_1) + h(v_2) - h(v_3) - h(v_4) \quad (55)$$

## 3.5 Results

### 3.5.1 Open-air channel

Water vapour, oxygen, and other atmospheric species can absorb electromagnetic waves across a wide range, from radio waves to the THz region, and even cause opacity in certain frequency bands. This absorption significantly degrades signal propagation quality through the channel. In the THz frequency bands, water vapour is the dominant absorption component in both open-air and indoor environments. Therefore, obtaining an accurate water vapour absorption spectrum is crucial for identifying atmospheric windows between strong absorption lines, enabling efficient THz communication.

Water vapour absorption consists of two components: resonant line absorption, which can be modelled as the sum of all resonant lines using spectroscopic database data and line shape functions, and continuum absorption, which is experimentally observed as the

difference between the measured total absorption and the resonant line absorption [120]. Using the method described in [121], we simulated the absorption coefficient $\alpha_f = \alpha_l + \alpha_c$ from 300 GHz to 2.1 THz. This includes the air-broadened spectrum $\alpha_l$ and the continuum absorption $\alpha_c$, as shown in Fig. 3.3 (a). The blue dashed line shows the air-broadened spectrum due to all the resonant absorption lines, calculated using parameters from HITRAN 2020 [122], under a relative humidity of 70.84% with 15.23 Torr of water vapour and 746.77 Torr of air. The yellow solid line represents the continuum absorption spectrum, which accounts for deviations between calculation and observation. The pink solid line shows the accurately modelled absorption coefficient $\alpha_f$. In Fig. 3.3 (b), we compare the absorption coefficient at humidity levels of 17.89%, 36.79%, 48.03%, and 70.84% corresponding to water vapour pressures of 3.60, 8.04, 10.05, 15.23 Torr, respectively. The results indicate several atmospheric windows with low absorption coefficients, making them suitable for applications. The relative humidity strongly influences these windows.

The transmissivity of the open-air link depends on the absorption coefficient $\alpha_f$ at frequency $f$ and transmission distance $d$, given by the Beer-Lambert Law [121]:

$$T_{ch} = \exp(-\alpha_f d) \tag{56}$$

We select three main frequency regions that cover absorption peaks and windows, based on recent hardware advances [16, 19, 39, 78]. Figure 3.4 shows the simulation results for the secure distance from fundamental frequencies $f$=300 GHz, $f$=580 GHz, and $f$=780 GHz, with a bandwidth of $\Delta f$=5 GHz at 300 K. Different modulation variances, specifically 1000 and 100, were considered for each frequency range. The increase in subcarriers from $N$=1 to $N$=32 in Fig. 3.4 (a), (c), and (e) enhances the SKR for communication. Previous studies, which did not account for modulation noise, suggested that the SKR increases linearly with the number of subcarriers in the scheme [58, 123]. However, for all three

communication bands as shown in Fig. 3.4 (a), (c), and (e), the SKR of $N$=64 is much lower than $N$=16, and for $N$=128, it is even smaller than that of a single carrier.

Therefore, the impact of high modulation noise between multiple subcarriers becomes significant, causing a substantial reduction in the SKR from $N$=32 to $N$=128. While the secure distance decreases for all frequencies and subcarrier counts when the modulation variance is reduced to $V_{mod}$=100, as shown in Fig. 3.4 (b), (d), and (f), the system becomes more robust against modulation noise. This is evidenced by the relatively stable SKR for $N$=32 to $N$=128 under lower $V_{mod}$. However, even with $V_{mod}$=100, the increase in SKR is hindered at $N$=128 due to the effects of modulation noise, especially for higher frequencies in Fig. 3.4 (d) and (f) compared with $f$=300 GHz in Fig. 3.4 (b). The highest SKR can be reached by $N$=128, $V_{mod}$=100 in Fig. 3.4(b) as ~72 bit/channel use, while the longest distance with multicarrier can be reached > 4.5 m in Fig. 3.4 (a) by $N$=4, $V_{mod}$=1000.

The initial SKRs for $N$<32 with $V_{mod}$=100 are slightly lower compared to $V_{mod}$=1000 for each frequency range. Therefore, while a higher $V_{mod}$ enables longer distances and higher SKRs, it is highly sensitive to modulation noise. Conversely, a lower $V_{mod}$ reduces the transmission distance and SKR but enhances robustness against modulation noise across multiple carriers. The cutoff distance is related to $N$ and highly depends on the THz absorption coefficient at the chosen operating frequency. Therefore, choosing the proper THz hardware with designed modulation variance is essential to control the modulation noise and secure performance. Further information can be find in Fig.B2 (a), Appendix B, about the influence between modulation variance, modulation noise, and subcarrier number.

The influence of the modulation variance $V_{mod}$ on the SKR and achievable transmission distance also provides practical guidance for the transmitter hardware design. Since $V_{mod}$ represents the variance of the Gaussian modulation applied to both quadratures, $Q \sim P \sim N$

(0, $V_{mod}$), the corresponding standard deviation is $\sqrt{V_{mod}}$. Therefore, $V_{mod}$=100 and $V_{mod}$=1000 correspond to standard deviations of 10 and approximately 31.6, respectively. Under the same normalisation and linear calibration, this ten-fold increase from 100 to 1000 in modulation variance corresponds to a 3.16-fold increase in the required modulation amplitude range for both quadratures and an increase in the modulation-related signal energy. In practical hardware, this places higher requirements on the output range and resolution of the DAC and driving electronics, the linear dynamic range and modulation depth of the modulation stage, and the available output capability of the THz source. In particular, the source and modulation chain must provide sufficient THz signal power and modulation range without introducing significant saturation, nonlinear distortion, or additional modulation noise. The results therefore reveal a practical trade-off, where $V_{mod}$=1000 can support a longer transmission distance but requires a larger modulation range and higher signal-energy capability and is less robust to modulation noise, whereas $V_{mod}$=100 requires less demanding hardware and provides better robustness to modulation noise at the cost of a shorter transmission distance. The practical selection of $V_{mod}$ should therefore consider the required transmission distance, modulation-noise level, and the modulation and output capabilities of the available THz source and transmitter hardware.

In addition, the significant increase of modulation noise can be inhibited by using a high-linearity modulator, and low distortion amplifier with a sufficient bandwidth linear-operating-area [124, 125]. By optimising the hardware, we can suppress the generation of nonlinear products such as intermodulation distortion and third-order intermodulation at the physical level to the greatest extent possible, which are the main sources of nonlinear noise. Furthermore, adding a proper cyclic prefix and using advanced digital signal processing compensation, such as digital predistortion and frequency domain equalization, is useful to defend against the modulation noise.

Unlike Figs 3.4 (c)-(f), where higher subcarrier counts can extend the secure distance, a single carrier achieves the greatest secure distance in the carrier frequency range starting from $f$=300 GHz in Fig. 3.4 (a) and (b). This is because $f$=300 GHz corresponds to the lowest absorption point in the exponential increase of the absorption coefficient.

Consequently, each additional subcarrier beyond $f$ encounters higher absorption, reducing the secure distance for its transmitted information compared to 300 GHz. The same reason causes the non-linear relationship of large $N$ and distance, that the significant absorption peak in the carrier frequency range leads to a short secure distance for the subcarrier located on the peak. Considering 100-200GHz has even lower absorption coefficient, we provide the simulation results in Fig.B1, Appendix B. It is impressive that the secure distance can be reached over 170m with 32 subcarriers in Fig.B1 (a).

Drawing on the humidity-induced absorption data from Fig. 3.3(b), we analysed the OFDM CVQKD protocol's performance at $f$=780 GHz with $V_{mod}$=1000 and 300 K under varying relative humidity in Fig. 3.5. For both single-carrier ($N$=1) and multi-carrier ($N$=32) configurations, reducing the humidity extends the transmission distance without affecting the initial secret key rate. The humidity influence of security distance is related to the absorption of THz electromagnetic waves by the water vapor in air, where the absorption coefficient shown in Fig. 3.3 (b) influenced the transmissivity $T_{ch}$ of the open-air channel in Eq.(56) that is deeply involved in the calculation of SKR from Eq. (46b) to Eq.(51). The higher absorption with high humidity environment highly decrease the THz signal amplitude for longer distance. When the THz signal is attuned to dark count level, Bob is hard to identify the information and background noise. More detailed analysis can be found in Fig.B2 (b) in Appendix B. By using 32 subcarriers spanning 780 GHz to 935 GHz in 5 GHz increments, a secure distance of 2.25m could be achieved at 17.89% relative humidity- almost triple that of a single carrier. Additionally, the secret key rate increases by over 15-fold. Compared with other THz CVQKD protocols, such as normal MIMO THz

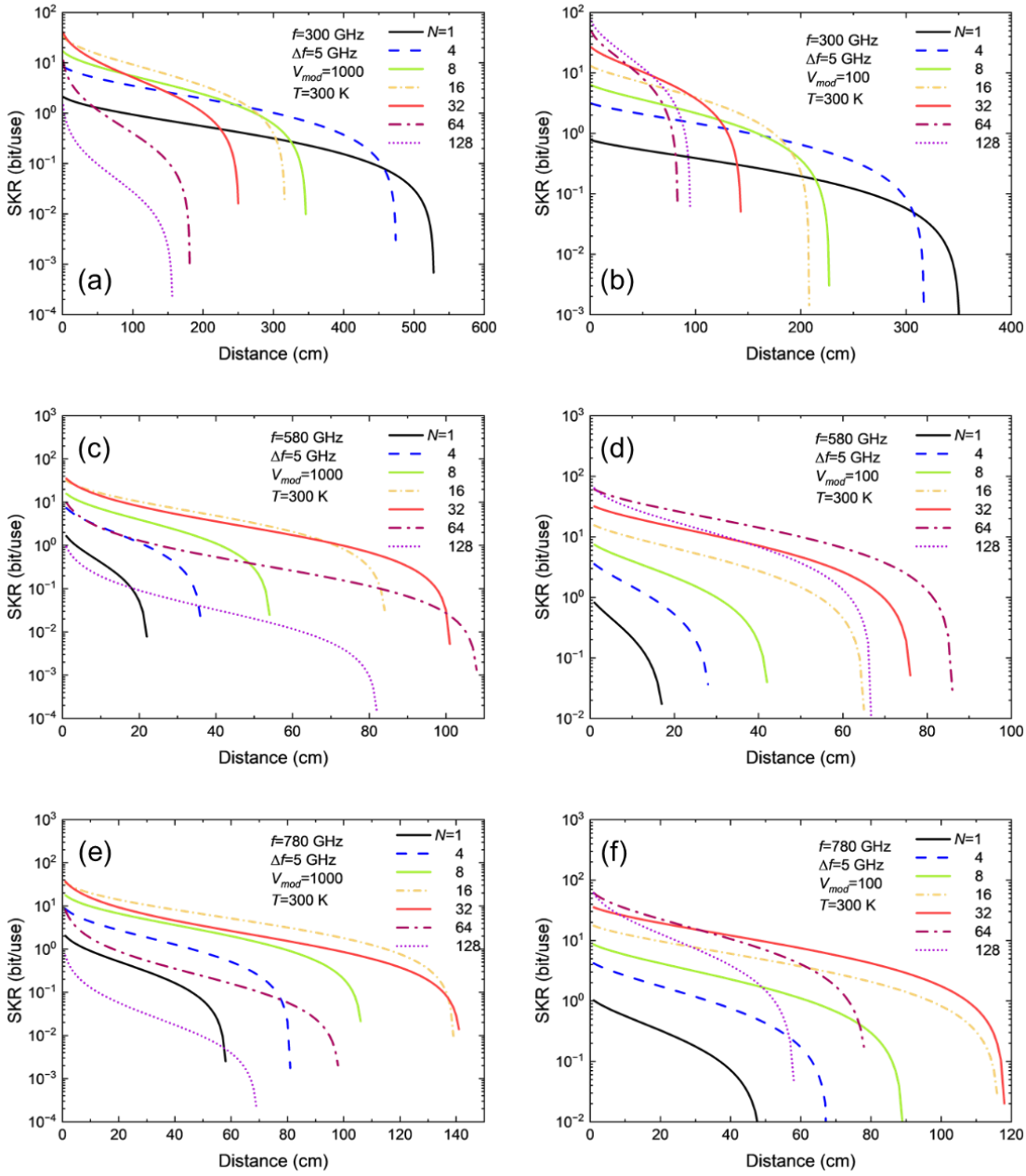



**Fig. 3.4.** SKR of THz-OFDM-CVQKD as a function of transmission distance using homodyne detection for different frequencies and modulation variances. (a) $f = 300$ GHz, $\Delta f = 5$ GHz, $V_{mod}$= 1000; (b) $f = 300$ GHz, $\Delta f = 5$ GHz, $V_{mod}$= 100; (c) $f = 580$ GHz, $\Delta f = 5$ GHz, $V_{mod}$= 1000; (d) $f = 580$ GHz, $\Delta f = 5$ GHz, $V_{mod}$= 100; (e) $f = 780$ GHz, $\Delta f = 5$ GHz, $V_{mod}$= 1000; (f) $f = 780$ GHz, $\Delta f = 5$ GHz, $V_{mod}$= 1000, all evaluated at 300K temperature, 70.84% relative humidity. The number of subcarriers $N$ varies as $N$=1, 4, 8, 16, 32, and 128, considering the worst-case modulation noise $\varepsilon_{mod}(k_{worst})$ for each $N$.

QKD, the SKR above 10 bits/use can be reached by the OFDM THz QKD, which is more than ten times higher [108].

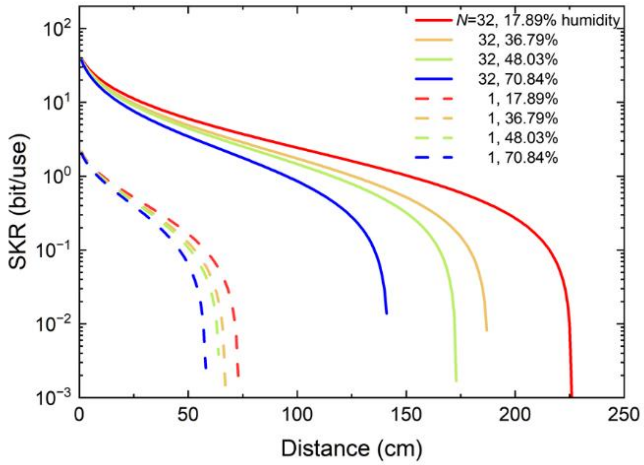



**Fig. 3.5.** SKR as a function of transmission distance using homodyne detection at $f = 780$ GHz, with $\Delta f = 5$ GHz evaluated under relative humidities of 17.89%, 36.79%, 48.03%, and 70.84%. The dashed lines represent the single-carrier configuration ($N$=1), and the solid lines correspond to the multi-carrier case ($N$=32). The modulation variance is $V_{mod}$=1000, and the worst modulation noise $\varepsilon_{mod}(k_{worst})$ is considered for each $N$.

In practice, the choice of operating frequencies (based on the absorption coefficient) and the balance among modulation noise, achievable SKR, and secure distance must align with specific application requirements. For instance, short-range indoor wireless links between quantum computers may only need a few meters of secure transmission. Under these circumstances, using multiple subcarriers and maintaining low humidity levels can be highly beneficial.

The OFDM THz CV-QKD system considered in this chapter is based on a single-antenna architecture. However, OFDM is commonly combined with MIMO in wireless communication systems, and the integration of MIMO with the proposed OFDM THz CV-QKD system provides a potential direction for future development. Based on the comparison between SISO and MIMO THz CV-QKD in the previous study, the use of multiple antennas at the transmitter and receiver has the potential to improve the transmission distance and achievable SKR. This suggests that extending the current OFDM THz CV-QKD system to a MIMO-OFDM architecture may provide further performance improvements. However, the introduction of MIMO would also increase the system

complexity and require additional consideration of channel estimation, antenna coordination, signal processing, and the associated noise and security effects. Therefore, extending the current OFDM THz CV-QKD scheme to a MIMO-OFDM architecture represents a promising direction for future investigation.

### 3.5.2 THz OFDM CVQKD Cryogenic links

Employing wireless communication within a quantum computer or cryostat can free valuable space by eliminating the need for bulky transmission lines, which often restrict the number of quantum circuits. In a cryogenic environment, the transmission link behaves similarly to inter-satellite channels, typically modelled as diffraction-limited, with transmissivity given by [88]

$$\mathrm{T}_{ch} = 1 - \exp\left(\frac{2{r_a}^2}{\omega^2(d)}\right) \tag{57}$$

where $\omega(d)$ is the beam radius at distance $d$, and $r_a$ is the receiver aperture radius. We set the beam-waist radius equal to the receiver aperture radius, i.e., $\omega_0 = r_a = 10$ cm. Therefore, the beam radius is calculated as

$$\omega(d) = \omega_0 \times \sqrt{1 + \left(\frac{\lambda d}{\pi \omega_0^2}\right)^2} \tag{58}$$

where $\lambda$ is the wavelength of the sub-carrier beam [88].

Figure 3.6 shows the simulation results of the SKR in a vacuum channel at 30 K with $f$=780 GHz and $\Delta f$=5 GHz, for (a) $V_{mod}$=100 and (b) $V_{mod}$=1000. Unlike open-air links, the secure distance increases linearly with the number of subcarriers due to the absence of atmospheric absorption. For a minimum SKR of $10^{-5}$ bit/channel use, a 128-sub-carrier

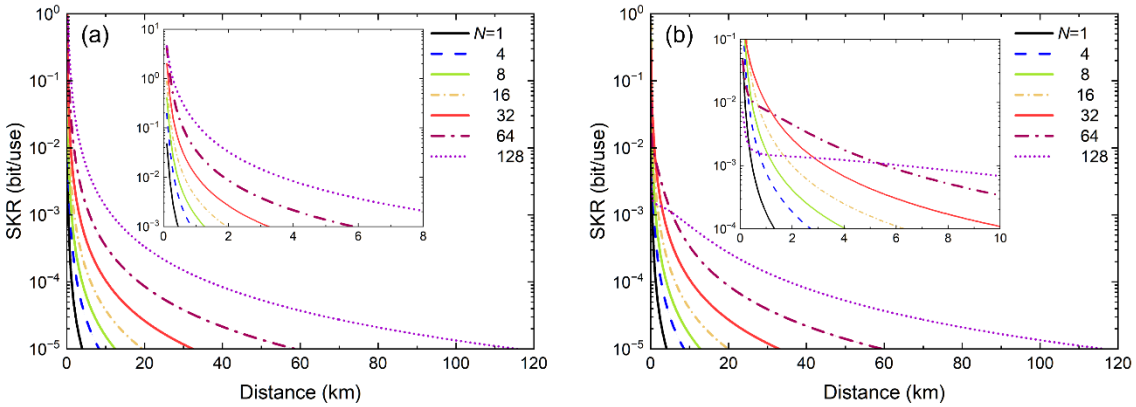



**Fig. 3.6.** SKR as a function of transmission distance in vacuum channel at 30K using homodyne detection with $f = 780$ GHz, and $\Delta f = 5$ GHz. (a) $V_{mod}$=100. (b) $V_{mod}$=1000. The analysis accounts for the worst-case modulation noise $\varepsilon_{mod}(k_{worst})$ for each subcarrier number $N$.

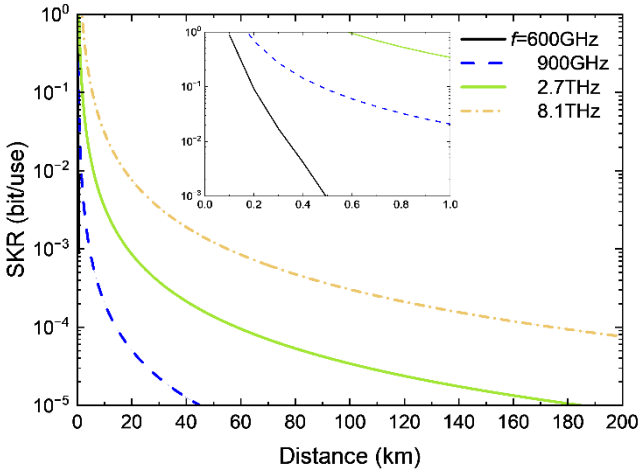



**Fig. 3.7.** SKR as a function of transmission distance in a vacuum channel at 30K using homodyne detection. The starting frequencies are $f$=600 GHz, 900 GHz, 2.7 THz, and 8.1 THz, with $\Delta f = 5$ GHz. The system employs 32 subcarriers ($N$=32) and a modulation variance of $V_{mod}$=100. The worst-case modulation noise $\varepsilon_{mod}(k_{worst})$ has been considered.

system with $V_{mod}$=1000 achieves a link distance of up to 116 km. However, in Fig. 3.6(b), the higher modulation variance leads to more pronounced SKR decay starting from $N$=64, as the modulation noise between subcarriers begins to significantly impact the SKR. In comparison, Fig. 3.6(a), with a lower modulation variance, shows only a slight decrease in SKR even at $N$=128. Thus, in both open-air and cryogenic vacuum channels, employing a lower modulation variance enhances robustness against inter-subcarrier modulation noise.

In Fig. 3.7, we examine a 32-subcarrier system operating across various frequencies. As the starting frequency increases from $f$=600 GHz to $f$=8.1 THz, the secure distance largely improves. It reaches over 200 km at $f$=8.1 THz with $V_{mod}$=100 at 30 K while the single carrier protocol requires 20 THz to reach similar distance [88]. Additionally, the SKR experiences a modest enhancement at these higher frequencies. Thus, to extend secure distances and boost SKR, it is essential to employ high frequencies along with an optimal subcarrier count that effectively mitigates modulation noise.

## 3.6 Proposal for THz QKD with Superconducting Coherent Photon Sources

To achieve THz-range quantum communication with multi-subcarriers, a tunable THz source with a broad radiation bandwidth is essential. High-temperature superconducting coherent THz emitters, integrating large arrays of phase-synchronised Josephson junctions, generate powerful and wideband THz waves at temperatures near or above 77 K (liquid nitrogen boiling point), demonstrating significant potential for quantum applications [67, 69, 70]. Without requiring a complex and bulky optical setup, these THz emitters operate with a DC voltage, generating 0.1–11 THz waves at the μW power scale with on-chip integrated availability based on its μm-scale mesa structures [65, 126, 127]. The laser-free superconducting THz source has recently been proven with an over 12-year life time, and achieves photon-level radiation over an open air channel up to nearly half a meter [68]. Moreover, these emitters can generate continuously modulated carrier waves with bandwidths up to 40 GHz, centred at 840 GHz [110, 115]. While a large gap remains between current technological advancements and the practical deployment of a THz QKD system, this work computationally explores the feasibility and potential of an OFDM-CVQKD protocol utilising these emerging THz sources. In Fig. 3.8(a), we simulate a wet open-air system ranging from single-carrier operation to $N$=12 subcarriers under different modulation variances. The results indicate that secure distances of up to 1.8 m (with

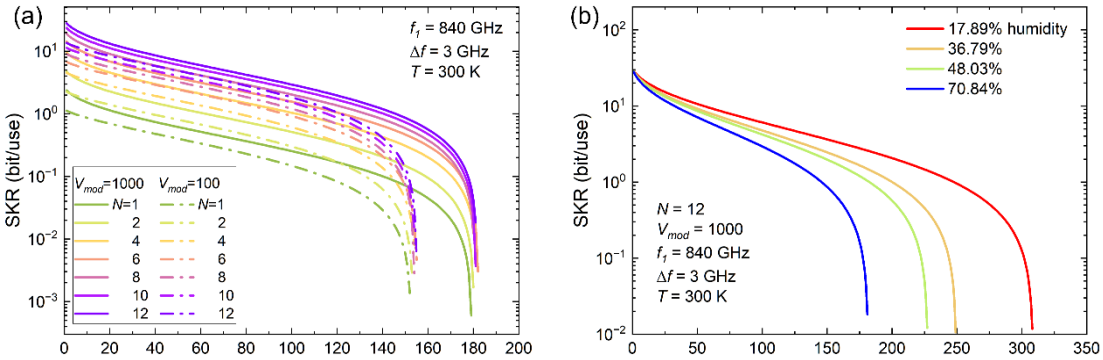



**Fig. 3.8.** (a) SKR as a function of transmission distance using homodyne detection at $f = 840$ GHz, with $\Delta f = 3$ GHz and 70.84% relative humidity. Solid lines represent $V_{mod}$=1000 while dash-dotted lines indicate $V_{mod}$=100. (b) SKR as a function of transmission distance using homodyne detection at $f = 840$ GHz, with $\Delta f = 3$ GHz under relative humidities of 17.89%, 36.79%, 48.03%, and 70.84% for a system with $N$=12 subcarriers and $V_{mod}$=1000.

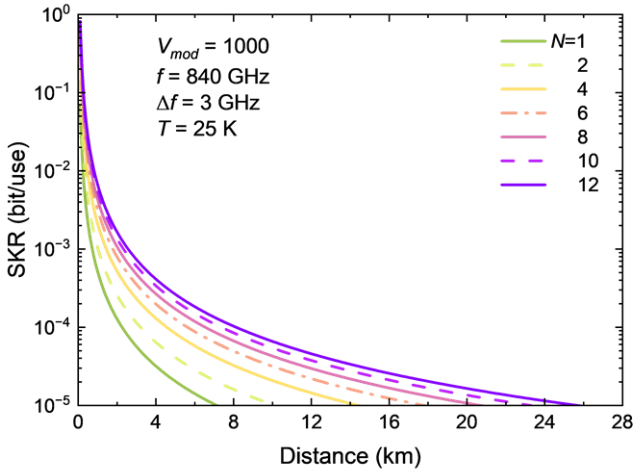



**Fig. 3.9.** SKR as a function of transmission distance in a vacuum channel at 25 K using homodyne detection with $f$=840 GHz, and $\Delta f = 3$ GHz. The modulation variance is $V_{mod}$=1000.

$V_{mod}$=1000) and 1.55 m (with $V_{mod}$=100) are largely unaffected by the number of subcarriers, as the frequency lies within a THz atmospheric window. In this region, modulation noise is relatively weak and does not significantly degrade the SKR. It is also evident that higher modulation variance extends both the secure distance and the SKR. Therefore, achieving optimal performance requires balancing the robustness against modulation noise provided by low modulation variance in multi-subcarrier systems with the improved transmission capabilities associated with high modulation variance. In the scenario presented in Fig. 3.8(b), the optimal configuration (with 12 subcarriers in a dry open-air environment) yields secure links of over 3 m, making it well-suited for short-

range wireless communications or local area networks between quantum computers. Considering that high-temperature superconducting coherent THz sources operate in cryostats, we evaluated their performance in a cryogenic or vacuum channel (see Fig. 3.9). With a 12-subcarrier configuration, the wireless link can extend up to roughly 26 km, presenting a promising solution for secure local area networks in quantum information processing as well as in space applications.

Currently, one of the most serious limitations for large-scale quantum computers is the physical area requirement to place the cables for superconducting quantum chips. The attractive advantage of using a high-temperature (High-Tc) superconducting THz source and THz QKD is their compatibility with superconducting quantum computers and the reduction of additional fibers that may require more space. Furthermore, wireless quantum communication by THz provides the possibility for mobile users, especially with the small size and feasibility of the High-Tc THz source, which can potentially operate using liquid-nitrogen-based cooling and relatively low DC bias voltages[66, 69, 70]. Without fine alignment requirements like optical fiber and being less fragile/bulky than optical lens systems, the mobility and durability of short-distance THz wireless quantum communication draw an attractive blue map for future mobile quantum communication.

In addition to the THz source, practical THz QKD systems also require suitable amplifiers, modulators, and detectors. THz amplifiers may be required to compensate for propagation and coupling losses. However, the available output power, gain, bandwidth, and operating frequency of current THz amplifiers remain limited at higher THz frequencies [128-130]. THz modulation is another important consideration, as existing THz modulators still face challenges in terms of modulation bandwidth, modulation speed, and modulation depth [36]. In the proposed architecture, IQ modulation can be implemented in the optical domain before THz generation, while dedicated THz modulation hardware could further improve the integration of the system. At the receiver, sensitive and low-noise THz detectors or coherent receivers are required to recover the quantum signal [131]. Their

sensitivity, bandwidth, and noise performance directly affect the practical performance of THz QKD systems. Compared with optical communication technologies, these THz components are still less technologically mature, which represents an important challenge for practical THz CV-QKD implementation [59]. Therefore, although High-Tc THz sources provide an attractive route towards compact and mobile THz QKD, the development of efficient THz hardware remains important for the practical implementation of wireless THz quantum communication.

## 3.7 Conclusion

This study provides a thorough security analysis of the THz OFDM-CVQKD protocol in both open-air and inter-satellite environments, addressing key physical-layer challenges such as excess noise from I/Q imbalance and third-order intermodulation effects. Our findings demonstrate that utilising multiple subcarriers can enhance the secret key rate SKR to ~72 bits/channel use, a 94 times improvement over single-carrier implementations. However, this advantage is offset by increased modulation noise, particularly in high-subcarrier regimes, necessitating an optimised trade-off between subcarrier count, SKR, and secure transmission distance. In inter-satellite QKD, higher fundamental frequencies and an increased number of subcarriers enable secure transmission beyond 100 km. Unlike terrestrial channels, modulation noise remains the primary limitation rather than absorption losses, highlighting the need for high-fidelity THz modulation sources to fully exploit the OFDM architecture. While lower modulation variance enhances resilience against intermodulation noise, it demands precision-engineered THz sources for practical implementation and limit the secret key rate and secure distance. Our research highlights both the potential and limitations of the OFDM THz QKD protocol, with application-level considerations. We explored the feasibility of implementing an OFDM-CVQKD protocol in the THz regime, supported by recently developed superconducting THz sources. Using these properties as input to our protocol, we simulated secure key rates under various

environmental conditions. Our results show that in wet or dry open-air channels, secure communication is possible over distances up to 170 m, while cryogenic or vacuum environments can support secure links up to ~26 km. These findings demonstrate that superconducting THz sources offer a viable platform for future chip-scale and wireless quantum communication systems. However, the current THz hardware development still remains a gap to the practical THz QKD platform. The simulation in our work requires highly separated subcarriers with ideal orthogonal and sufficiently suppressed crosstalk to reduce the channel correlation, which requires high synchronization between the source and receiver. Further research on the integration of the superconducting THz hardware is essential and urgent for the accomplishment of the THz QKD. As THz device technology advances, particularly in chip-scale superconducting Josephson junction emitters, coherent THz modulators, and detectors, our findings provide a foundation for the next generation of high-speed, wireless quantum networks spanning terrestrial and space-based QKD infrastructures. We are continuing to work on the THz hardware at the photon level and hoping to provide the physical solution for THz QKD in the near future.

## 3.8 Appendix B

Fig.B1 shows the performance down to 100GHz and 200GHz of the OFDM QKD protocol. The transmissivity of the open-air link depends on the absorption coefficient $\alpha_f$ in dB/km at frequency $f$ and transmission distance $d$, given by [53]:

$$T_{ch} = 10^{-\alpha_f d/10}$$

with $\alpha_f$=0.6 dB/km at 100GHz and $\alpha_f$=1.2 dB/km at 200GHz. Similar to the results in higher frequencies, the low modulation variance $V_{mod}$ leads to a much smaller modulation

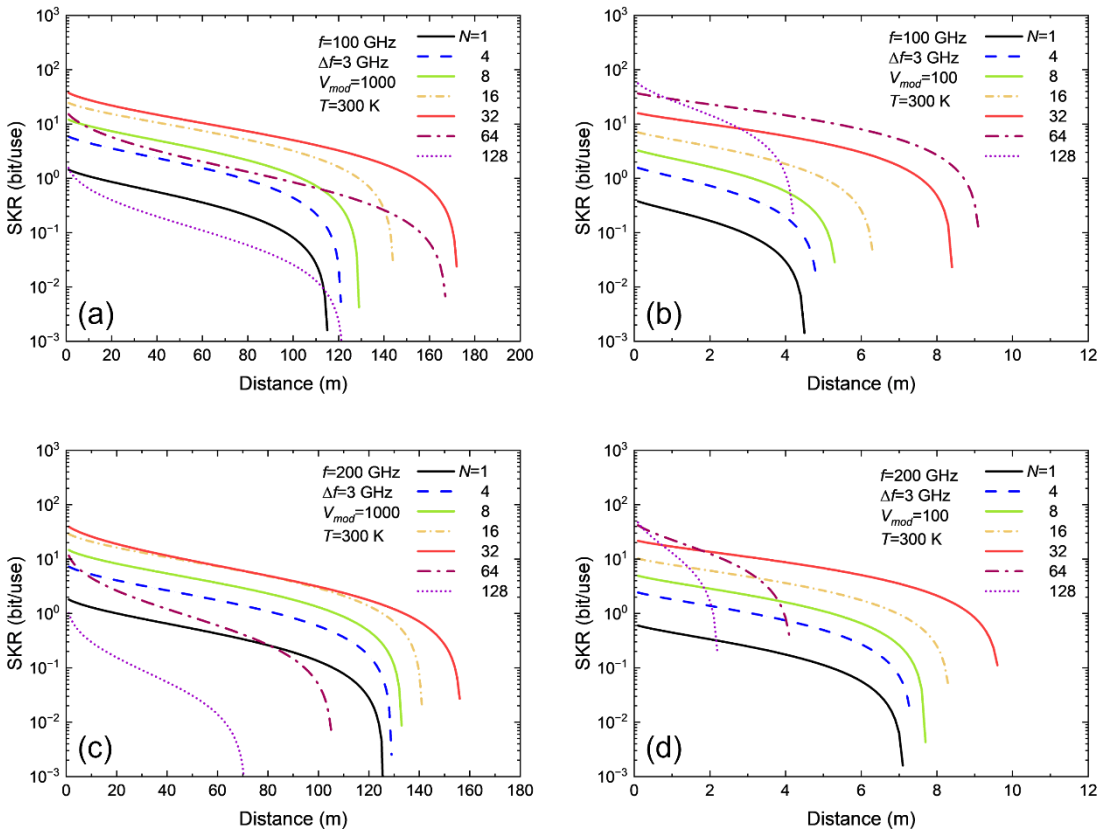



**Fig. B1.** SKR of THz-OFDM-CVQKD as a function of transmission distance using homodyne detection for different frequencies and modulation variances. (a) $f = 100$ GHz, $\Delta f = 3$ GHz, $V_{mod}$= 1000; (b) $f = 100$ GHz, $\Delta f = 3$ GHz, $V_{mod}$= 100; (c) $f = 200$ GHz, $\Delta f = 3$ GHz, $V_{mod}$= 1000; (d) $f = 200$ GHz, $\Delta f = 3$ GHz, $V_{mod}$= 100, all evaluated at 300K temperature. The number of subcarriers $N$ varies as $N$=1, 4, 8, 16, 32, and 128, considering the worst-case modulation noise $\varepsilon_{mod}(k_{worst})$ for each $N$.

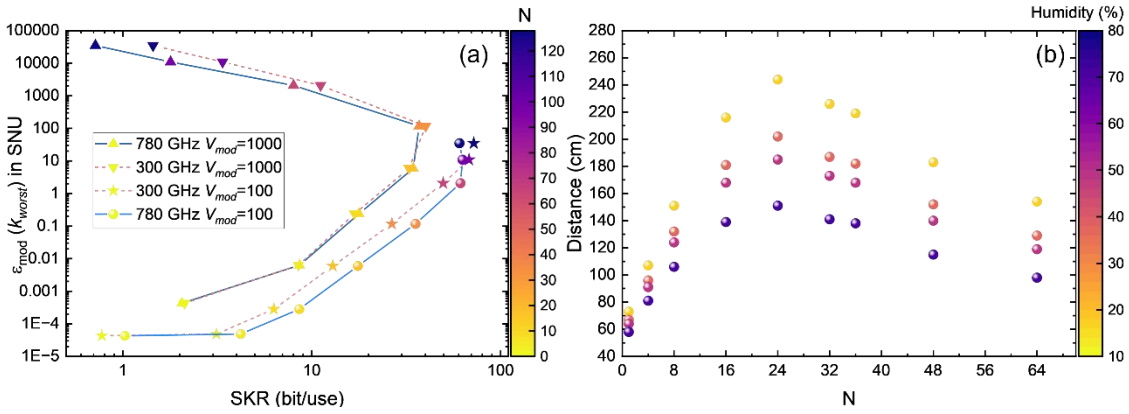



**Fig. B2.** (a) Worst modulation noise $\varepsilon_{mod}(k_{worst})$ across $N$ subcarriers at 300GHz and 780GHz OFDM QKD systems versus secret key rate peak level, $\Delta f = 5$ GHz. (b) The humidity influence on the distance at different $N$ subcarriers OFDM QKD systems at 780GHz, $\Delta f = 5$ GHz, $V_{mod}$=1000.

noise $\varepsilon_{mod}$ with large $N$ in the system, but limits the distance and the highest SKR. This can be supported by the results shown in Fig.B2 (a). The modulation noise doesn't relate to the frequency used in the system, but is highly related to the modulation variance $V_{mod}$ and the subcarrier number $N$. The modulation noise started to highly decrease the SKR from a few hundred SNU, where the exact number is also related to the frequency and subcarrier number due to the difference in absorption coefficient. Considering the cost-effectiveness between hardware, distance, and SKR, higher modulation variance is a better choice than lower. The longest distance can be reached by 100GHz with 32 subcarriers, over 170m with its low absorption coefficient at 70.84% relative humidity.

Notably, from Fig.B2, the lower humidity can lead to a longer distance even with large subcarrier number N when the modulation noise starts to harm the system. This is because the lower humidity leads to lower absorption coefficient and results in a higher transmissivity at each distance.

# Chapter 4
# Tunable terahertz source on a chip with decade-long stability using layered-superconductor elliptical microcavities

**Publication statement:** *This chapter is based on the following publication: Mingqi Zhang, Shungo Nakagawa, Yuki Enomoto, Yoshihiko Kuzumi, Ryuta Kikuchi, Yuki Yamauchi, Toshiaki Hattori, Richard A. Klemm, Kazuo Kadowaki, Takanari Kashiwagi, and Kaveh Delfanazari， "Tunable terahertz source on a chip with decade-long stability using layered-superconductor elliptical microcavities." Physical Review Applied 24.5 (2025): 054012.* *Copyright © 2025 by American Physical Society. All rights reserved.*

## 4.1 Abstract

Chip-scale, electrically tunable, continuous-wave, coherent terahertz (THz) radiation sources are critical for emerging applications in sensing, imaging, spectroscopy, communications, space, and quantum technologies. Here, we demonstrate a robust source-on-a-chip THz emitter based on a layered high-temperature superconductor, engineered with an elliptical microcavity and capable of sustained coherent emission over an unprecedented operational lifetime exceeding 11 years. This compact THz source operates up to 60 K (with $T_c \approx 90$ K), delivering stable radiation in the 0.7–0.8 THz range, with on-chip electrical tunability from 100 GHz to 1 THz. Coherence arises from the phase-locked oscillation of intrinsic Josephson junction arrays, resonantly coupled to transverse electromagnetic modes within the cavity, analogous to a laser cavity, yielding collective

macroscopic oscillations. THz emission remains detectable across an approximately 0.5-m free-space open-air link at room temperature. We analyse the cavity-mode structure and extract THz photon generation rates up to approximately 503 photons $fs^{-1}$ in cryogenic conditions and 50–260 photons $ps^{-1}$ over the air. These results demonstrate, for the first time, sustained and electrically tunable coherent THz emission from superconductors over multiyear timescales, defining another class of robust, chip-integrated THz lasers with applications in scalable THz and quantum technologies.

## 4.2 Introduction

Terahertz (THz) waves, spanning 0.1–10 THz between microwave and optical frequencies, have gained significant attention in recent decades due to their potential in fundamental research and diverse applications. Beyond classical uses in biomedical imaging, chemical identification, nondestructive inspection, and next-generation communication, recent advances in quantum technology suggest the feasibility of THz quantum communication and quantum sensing [5, 10, 53, 59, 107, 108, 127, 132-134]. The advantages of THz waves, including high stability in dust, fog, and atmospheric turbulence compared to free-space optical links, and higher operating temperatures in quantum computing compared to microwaves, highlight the untapped potential of the THz region as a key research focus [135]. However, efficient THz hardware, including sources, modulators, and detectors essential for practical applications, is still in its early stages [16, 19, 21, 39, 104, 110, 115]. High-temperature superconducting $Bi_2Sr_2CaCu_2O_{8+\delta}$ (BSCCO) emitters, composed of two-dimensional van der Waals (vdWs) layers with naturally formed intrinsic Josephson junctions (IJJs) arising from alternating $Bi_2O_2$ insulating layers and $CuO_2$ superconducting layers, have been shown to generate broadband terahertz (THz) radiation spanning from 150 GHz to 11 THz, using both on-chip and off-chip detection techniques. The mesa structures in these devices support a macroscopic coherent electromagnetic state through cavity resonance, wherein a large number of stacked IJJs are

phase synchronized, resulting in coherent THz emission, a phenomenon extensively reported and validated in foundational studies [15, 65, 67, 71]. For sustained over-the-air applications, the stability and longevity of a THz source are as crucial as its power and bandwidth for practical viability. This study introduces several key contributions to solid-state THz technology, including (i) robust, long-lasting, and electrically tunable elliptical cavity BSCCO THz source, emitting within the 100 GHz–1 THz range, with intense radiation at 700–800 GHz. Fabricated and measured in early 2012, and remeasured in late 2023, the device retains its superconducting phase transition, electrical response, and THz output power, demonstrating exceptional long-term stability and operational resilience. Elliptical microcavities offer a key advantage for generating circularly polarised THz radiation over other geometries, such as rectangular cavities, since their asymmetry supports two orthogonal resonant modes with nearly degenerate frequencies, which can couple with a 90° phase difference under suitable excitation forms. This property allows efficient circular polarisation, especially useful for wireless communication applications, directly from the cavity itself. (ii) The THz emissions were detected across a 44-cm free-space channel nearly 12 years after fabrication, highlighting the device's viability for sustained cryogenic and free-space applications. (iii) The unique elliptical cavity design optimises transverse electromagnetic modes, enabling efficient photon generation and tunable THz emission from 100 GHz to 1 THz. (iv) High THz photon generation rate and achieving approximately 503 photons per femtosecond ($fs^{-1}$) in cryogenic conditions and 50–260 photons per picosecond ($ps^{-1}$) over-the-air transmission, highlighting the device’s usefulness for various applications, especially in classical or quantum communication and computation.

## 4.3 Tunable coherent THz source fabrication and measurement setup

The BSCCO elliptical cavity THz source was fabricated from a BSCCO single crystal grown using the traveling-solvent floating-zone (TSFZ) method [23, 136]. The crystal was exfoliated into thin flakes using Scotch tape, and a flat, optimally thick flake was selected, transferred, and affixed to a sapphire substrate. A focused ion-beam (FIB) system was employed to etch the elliptical geometry, creating three elliptical cavity structures, named devices 1, 2, and 3, arranged in a parallel array on the surface of the BSCCO chip, as shown in Fig. 4.1(a). The three elliptical cavities are nearly identical in size, with dimensions $a \approx 245$ μm, $b \approx 52$ μm, and $d \approx 1$ μm, as shown in Fig. 4.1(b). The cavity (mesa) thickness $d$ was estimated from the number of Josephson junctions using the ac Josephson effect, with each junction $d_j \approx 1.533$ nm [137], as the FIB may not etch through the entire BSCCO flake on the substrate. Gold wires were attached to the top of each elliptical device and the edge of the BSCCO crystal to apply an electric field across the

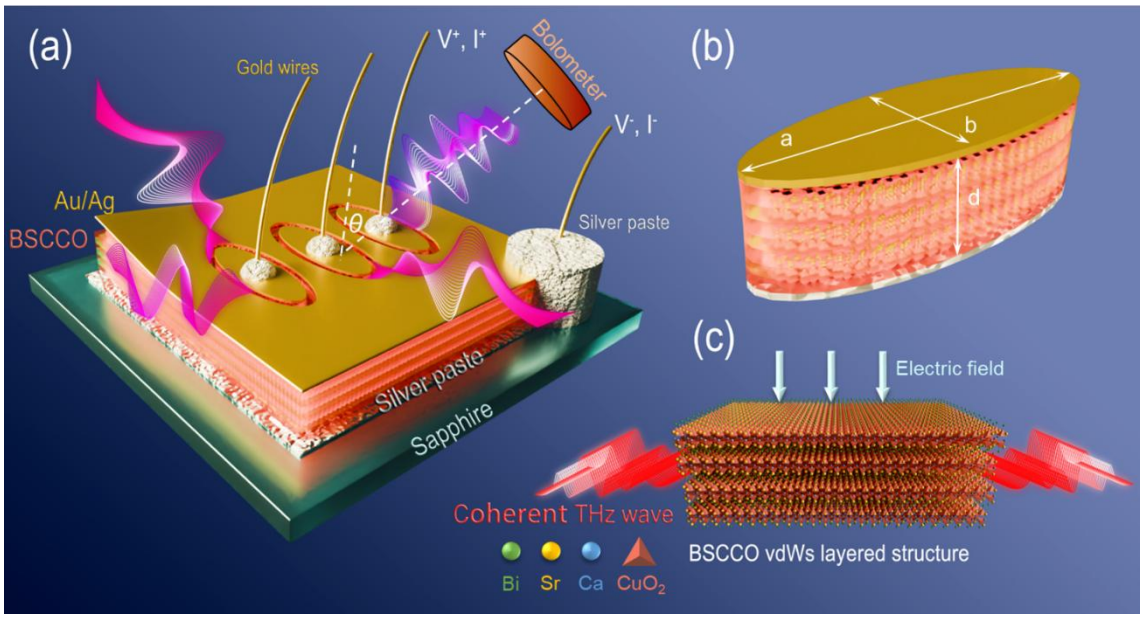



**Fig. 4.1** (a) Schematic of the BSCCO elliptical cavity THz source array. (b) Detailed schematic of an individual elliptical cavity on the device, with dimensions $a \approx 245$ μm, $b \approx 52$ μm, and $d \approx 1$ μm. (c) Illustration of the BSCCO van der Waals (vdWs) layered structure, forming nanoscale intrinsic Josephson junctions within the BSCCO cavity. In this study, the devices were operated and measured individually within the array structure.

IJJs. For the storage, the sample box was sealed with tape to prevent exposure to fresh air and stored in an indoor environment. This simple method ensures high durability and practicality for applications without complex requirements. The fabrication process is detailed in Appendix C, Fig. C1(a), and a scanning electron microscope (SEM) image of the device is shown in Fig. C1(b). For the measurements, the sample was mounted to the cold finger using silver paste in 2012, copper clamps and thermal grease in 2023, then cooled in a $^4$He flow cryostat. For basic measurements such as temperature-dependent resistance and current-voltage characteristics, a voltage source was used to apply an external dc voltage across the device. The bias voltage and current were monitored using two separate digital multimeters. Radiation output was detected using a Si bolometer (for the 2012 measurement) or an InSb hot electron bolometer (HEB) (for the 2023 measurement), with an optical chopper operating at 70 Hz for amplitude modulation, employed in the lock-in technique.

This is a standard method for THz measurement widely used for the characterization of BSCCO devices [15, 65, 67, 71, 115]. The setup was positioned in front of the THz window of a $^4$He flow cryostat, as illustrated in Fig. C2 in Appendix C. The angle between the normal of the device and the bolometer is defined as $\theta$, illustrated in Fig. 4.1(a). The frequency-measurement setup and results are discussed in detail in Sec. 4.5.

## 4.4 Tunable coherent THz radiation source sustained over 11 years

For the first time, we have successfully measured and confirmed stronger THz radiation output from a device almost 12 years after its fabrication, along with its experimentally determined frequency. In this section, we will discuss the measurement results of critical temperature, current-voltage characteristics (IVCs), and emission from the 2012 and 2023 measurements. Comparing the IVCs of device 1 in Fig. 4.2(a) at different bath temperatures for the 2012 (red) and 2023 (blue) measurements, both sets exhibit the typical

hysteresis and branching structure characteristic of IJJ stacks [137]. The sharp voltage jump from <0.7 V to >0.9 V, $I \gtrsim 40$ mA, observed in the 2012 IVCs reflects the generation of hot spots, leading to a significant temperature increase in the device [138]. On the return branches, the backbending in the 2023 measurements is less pronounced than in 2012, across all bath temperatures. Considering the sudden voltage jump to its highest value at bath temperatures of 20 and 30 K, the thermal release of the device's local temperature in 2023 appears to be improved compared to 2012 [70, 138]. Therefore, using copper clamps to securely attach the device directly to the cold finger with thermal grease beneath the sapphire substrate enhances heat removal during the measurement, compared to using silver paste. The emission directed to the Si or the HE bolometer can be observed through the bolometer's output voltage, $V_{\text{output}}$. However, the optical responsivity $\alpha$ differs between the two types of bolometers. To compare the radiation output in 2012 and 2023, we estimated the output voltage in terms of the radiation power reaching the detector at a bath temperature $T_b = 40$ K, as shown in Figs. 4.2(b) and 4.2(c). The relationship between the output voltage and detected power is given by

$$\mathrm{P} = 2\sqrt{2}\frac{V_{output}}{\alpha} \tag{59}$$

where the optical responsivity $\alpha_{\text{HEB}}$=3.3 mV/nW for the 2023 HEB detection and $\alpha_{\text{Si}}$=11 mV/nW for the 2012 Si-bolometer detection, both calibrated by black body radiation, and with coefficient number $2\sqrt{2}$ [126]. This factor arises because, when the THz beam is mechanically chopped such that the detected power varies approximately sinusoidally with time, as is typical for the bolometer setups used in the present measurement, a lock-in amplifier calibrated for a square-wave signal reports an rms signal amplitude that is smaller than the actual peak-to-peak amplitude by a factor of approximately $2\sqrt{2}$. The emission occurred at a lower bias voltage and current in 2023, which is primarily attributed to the doping change of the BSCCO crystal, consistent with the critical temperature $T_c$ increase from approximately 85 K in 2012 to approximately 90 K in Fig. 4.2(d). This

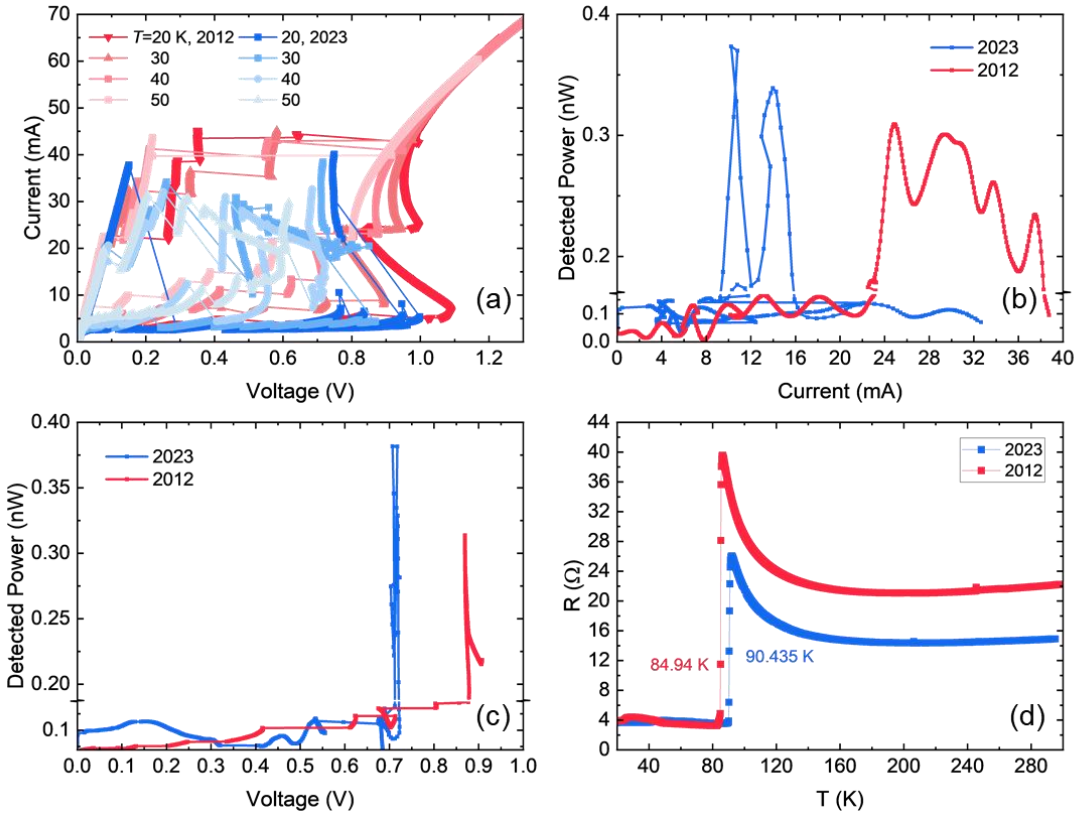



**Fig. 4.2** (a) Current-voltage characteristic for device 1 at different bath temperatures in 2012 (red set) and 2023 (blue set). (b) Over-the-air detected power versus bias current for device 1 at 40 K, at $\theta$=0° in 2023 and $\theta$=30° in 2012. (c) Over-the-air detected power versus bias voltage for device 1 at 40 K, at $\theta$=0° in 2023 and $\theta$=30° in 2012. (d) Temperature-dependent resistance (RT) curves for device 1 in 2012 and 2023.

suggests the device was nearly optimally doped in 2023 [139]. Improved heatsinking can mitigate self-heating effects in the IVCs; however, the superconducting transition temperature $T_c$, determined from equilibrium resistance versus temperature measurements, is not expected to be significantly affected by substrate heatsinking or long-term relaxation of crystalline defects introduced during the focused ion-beam etching process.

Considering the emission in 2023 is more substantial than in 2012 at 40 K, the device achieved higher radiation efficiency in 2023, with lower bias power and higher detected power. Moreover, the operating temperature of this device in 2023 reached $T_b = 55$ K, still achieving about half of the highest output at $T_b = 40$ K, as shown in Figs. 4.3(b) and 4.3(c). While the bias current remains relatively stable across different bath temperatures in Fig. 4.3(b), the emission occurred at a lower bias voltage along the backbending region at

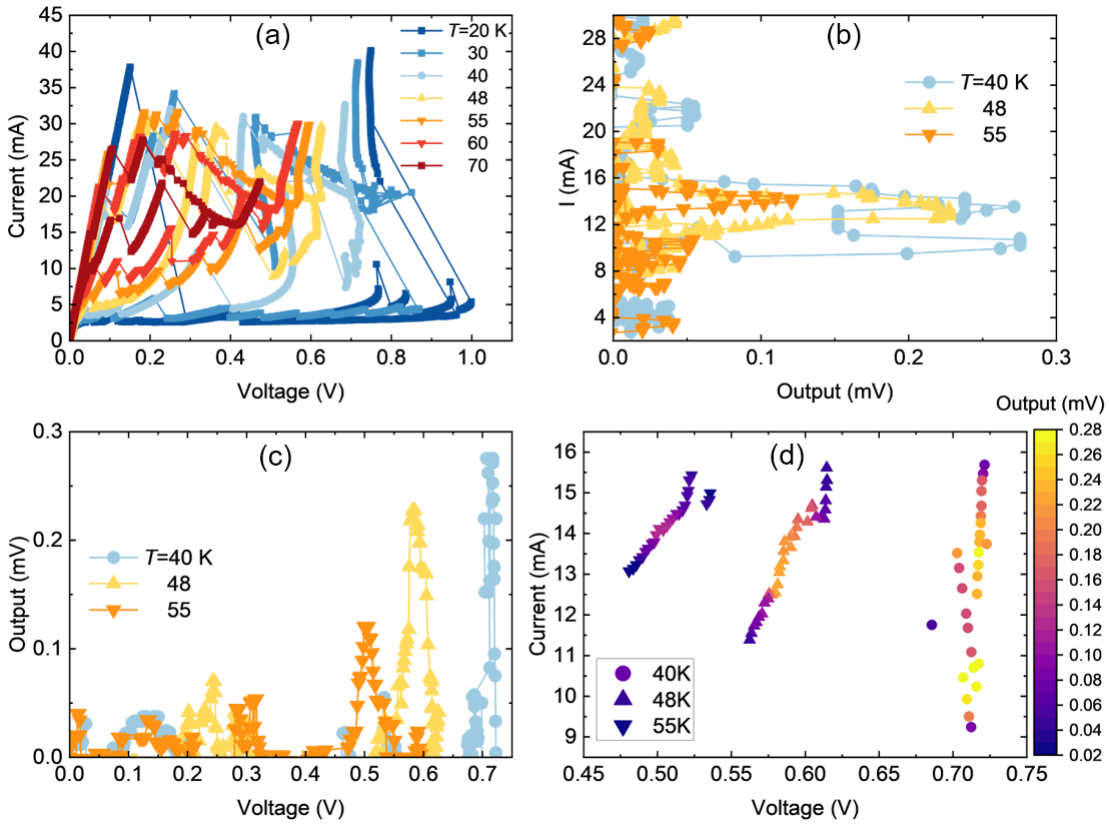



**Fig. 4.3** (a) Current-voltage characteristics (IVCs) at different bath temperatures for device 1 in 2023. Output from device 1 detected by the HEB vs (b) bias current at different temperatures, at $\theta = 0°$ in 2023, and vs (c) bias voltage at different temperatures, at $\theta = 0°$ in 2023. A standard median filter has been used to reduce the background noise level in these figures. (d) IVCs at the THz radiation range at different temperatures.

higher bath temperatures, as seen in Fig. 4.3(c). The backbending in the 2023 IVCs in Fig. 4.3(a) became increasingly less noticeable at higher temperatures and eventually disappeared at around 60 K. This behavior is related to Newton's law of heating, which leads to the device overheating at lower bias voltages as the bath temperature increases [140]. The resistance-temperature (RT) curves and IVCs for the other devices from the 2012 measurement are provided in Fig. C3.

It is worth noting that the development of BSCCO-based THz sources has undergone intensive theoretical and experimental investigation over the past two decades, ranging from fundamental studies of IJJ dynamics to practical device geometries and radiation enhancement schemes, and more recently to application-oriented integration efforts [18, 25, 30, 66, 69, 127, 141-152]. From Fig. 4.3(d), we can gain a clearer view of the radiation

intensity at different bias points at different temperatures. The double radiation peaks in Fig. 4.3(b) at 40 K are related to the jump into a different branch at the backbending region caused by the unreleased hot spot, as illustrated in Fig. 4.3(d). Together with the radiation region *I-V* with less pronounced backbending at higher temperature, these characteristics match the former study, which suggests that the higher radiation intensity at 40 K is related to the presence of a hot spot [150, 153]. Due to long-term storage, the top electrode gold wires, attached with silver paste on devices 2 and 3, were found to be broken in 2023. Therefore, improving the electrical feeding method and device packaging is critical for future device generations. This chapter focuses specifically on THz emitters with elliptical cavities, investigating the mechanisms of electromagnetic wave radiation and the associated cavity modes. However, we have also observed THz emission from BSCCO devices fabricated concurrently on a separate chip. A detailed analysis of those results will be presented in a forthcoming publication.

## 4.5 Free-space over-the-air THz radiation frequency measurement

Considering the free-space detected power of device 1 after a 10 cm over-the-air link via the HEB setup in Fig. C2(b), which is around 0.5 nW and highly sensitive to changes in bias voltage, this presents a significant challenge for frequency measurement over long-distance over-the-air channels.

To address this, we replaced the dc source (Keithley 2400 Sourcemeter) and optical chopper with a wave generator (Agilent 33220A), which superimposes a 1-kHz sinusoidal wave onto the dc voltage with a 70 $mV_{pp}$ peak-to-peak amplitude, as shown in Appendix C, Fig. C4. This setup provides an accurate bias voltage and enables the fast switching of the signal pulse simultaneously. The frequency was measured using a Michelson interferometer in over-the-air (room temperature), as shown in Fig. C4. Notably, the THz wave measured from our device passed through a free-space link of over 44 cm,

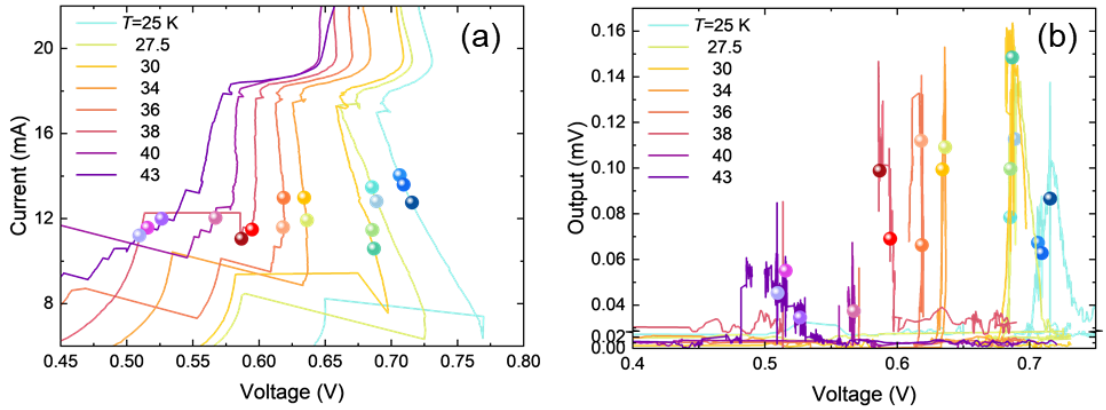



**Fig. 4.4** (a) Current-voltage characteristic for device 1 at different bath temperatures in 2023. The highlighted points are the bias points for frequency measurement at $\theta$=0°. (b) The output voltage from the HEB detector at different temperatures, and $\theta$=0°. The highlight points are output points for frequency measurement.

and only half of the power radiation reached the detector through the beam splitter, which is promising for applications requiring wireless channels over-the-air.

The IVC curves of device 1, driven by the wave generator at different bath temperatures, are shown in Fig. 4.4(a). The highlighted points on each curve indicate the bias points corresponding to the frequency spectrum measurement, as shown in Fig. 4.5(a). These bias points were selected around the output measurement peaks from the HEB, illustrated in Fig. 4.4(b). In this measurement setup, the lowest temperature at which THz radiation was measured was 25 K, with strong radiation detectable between 30 and 40 K. The highest detected power was approximately 0.137 nW (approximately 0.16-mV output voltage) after the 44-cm propagation at $\theta = 0°$ with the setup in Fig. C4. Similar measurements were also conducted at $\theta = 30°$, as shown in Fig. 4.5(b) with the IVCs and output in Appendix C, Fig. C5.

From the frequency spectrum in Fig. 4.5, THz radiation was observed between 100 GHz and 1 THz, with the most powerful radiation frequency tunable around 650–800 GHz. The sampling frequency of the Michelson interferometer limited the resolution of the spectrum. In Fig. 4.5(a) and 4.5(b), we observe a slight shift in the frequency peak, influenced by

both bias voltage and bath temperature. The relationship between frequency and bias voltage at the same bath temperature is consistent with the ac-Josephson relation, given by

$$f = \frac{2eV}{hN} \tag{60}$$

where $e$ is the electronic charge, $V$ is the voltage across the junctions, $h$ is Planck's constant, and $N$ is the number of junctions. The number of active junctions in device 1 changes between 300 and 500, and is inversely related to the bath temperature, as shown in Fig. C6.

The tunable relation between $f$ and $N$ at each temperature in Fig. C6 is similar to the branch effect observed in previous studies [18]. The variation in the number of active junctions in different measurements at the same temperature may be due to jumps into different

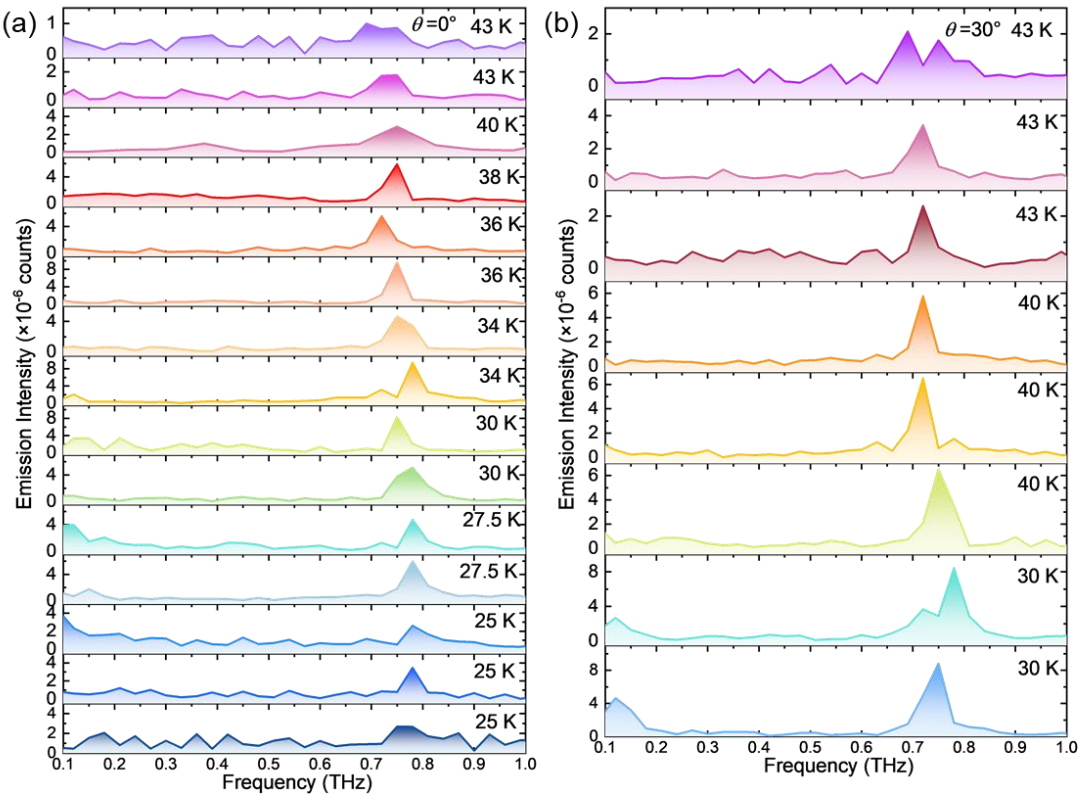



**Fig. 4.5** (a) Frequency spectra from 100 GHz to 1 THz for the elliptical cavity at different bath temperatures at $\theta$=0°. The intensities are scaled by factors of 3, 3, and 2 for 43 K and 40 K. Grey dashed lines indicate the frequency shift trend. (b) Frequency spectra from 100 GHz to 1 THz for the elliptical cavity at different bath temperatures at $\theta$=30°. The intensities are scaled by factors of 3, 2, and 3 for 43 K. The intensity in (a) and (b) is offset for clarity.

branches in the backbending region. In addition to the strong frequency peaks from the ac-Josephson effect, smaller peaks around 120 and 210 GHz are observed in the measurements shown in Fig. 4.5 (for a zoomed-in area see Fig. C9). Weak peaks in the 0.3–0.6 THz range also appear at certain temperatures. While the geometry of the BSCCO mesa can activate cavity modes alongside the ac-Josephson effect [71], further investigation is needed to fully determine the origin of the low-intensity peaks in the spectrum. Studies using newly fabricated elliptical cavity devices with higher-intensity radiation will be crucial for a deeper understanding of these peaks. By rotating the sample at different angles $\theta$, as defined in Fig. 4.6(b), we plot the angle-dependent radiation pattern of device 1 at $T_b = 45$ K as shown in Fig. 4.6(a) (red dots). The angular range in this figure was constrained by the hardware's degrees of freedom. The power is calculated from the highest output voltage at each angle of the HEB by Eq. (59). Since the primary radiation intensity is concentrated around 700–800 GHz, the resonance frequency two-dimensional (2D) far-field pattern of the elliptical cavity structure was simulated in COMSOL within the same frequency range to analyze the electric-field distribution. The 2D far-field pattern, taken from the same direction as the measurement, shows a square relationship with power. To identify the optimal radiation mode and frequency for comparison with the radiation pattern, we employed both mathematical analysis and simulations in the following section. Building on previous research, a BSCCO THz emitter can be modeled as an antenna with Neumann boundary conditions along the edge of the ellipse, where the normal derivative of the wave function vanishes at the boundary [30].

In the simulation model, the boundary can also be defined using the surface current density boundary condition [141]. The antenna's TM mode can be estimated from the modified Mathieu function, applying the Neumann boundary condition for the TM(m, r) mode as given by [154]

$$0 = \begin{cases} \partial_\mu Ce\left(\mu_0, q_{mr}^{(1)}\right) \\ \partial_\mu Se\left(\mu_0, q_{mr}^{(2)}\right) \end{cases} \tag{61}$$

where *C*e and *S*e represent the even and odd solutions, $\mu_0 = \operatorname{atanh}\left(\frac{b}{a}\right)$, is the eccentricity of the ellipse. Note that the TM mode described here differs from the 2D model in [154], that is based on the microstrip antenna model and the boundary conditions outlined in [30]. The resonance frequency $\omega$ is related to [154]

$$q_{mr} = \frac{k^2 {l_f}^2}{4} \tag{62}$$

$$k^2 = \frac{n^2\omega^2}{c^2} \tag{63}$$

with the focal length of the ellipse $l_f$, the refractive index *n* of BSCCO, and the speed of light *c*. The relative permittivity of BSCCO is set to be $n^2$=17.76. We have ignored the transverse wave vector here as the thickness of the mesa is small, and only considered the wave vector *k* of the mode in the plane of the layer. The value of $q_{mr}$ can be determined in Wolfram Mathematica by scanning the zero point of the curve for Eq. (61), provided in Appendix C, Table I. As a result, this device has the $TM_{even}$ (0,1) mode at 701.66 GHz, $TM_{even}$ (1,1) mode at 749.55 GHz and $TM_{even}$ (2,1) mode at 798.87 GHz, which are close to the radiation frequencies. We first consider a stand-alone elliptical mesa with 1 μm thickness without a gold wire as a feedline, groove, or substrate. The electric-field distribution at (0,1), (1,1), and (2,1) modes is provided in Fig. C10 and Figs. 4.6(c) and 4.6(d) by eigenfrequency simulation in COMSOL with perfectly matched frequencies at 701.45, 749.5, and 798.9 GHz. However, the device is more complex than a single stand-alone mesa. In our simulation, we consider the remaining bottom layer (due to imperfect FIB milling) and the surrounding BSCCO crystal together with the groove cavity and the central feedline. Although the wave function and eigenfrequency for a stand-alone mesa suggest a (1,1) mode around 750 GHz, closely matching the device's radiation frequency, strong resonance with a similar (1,1) pattern is not observed in the device simulation within the 0.7–0.8 THz range. On the other hand, between 0.768 and 0.78 THz, the elliptical mesa exhibits a strong TM(2,1) mode with a matching electric-field

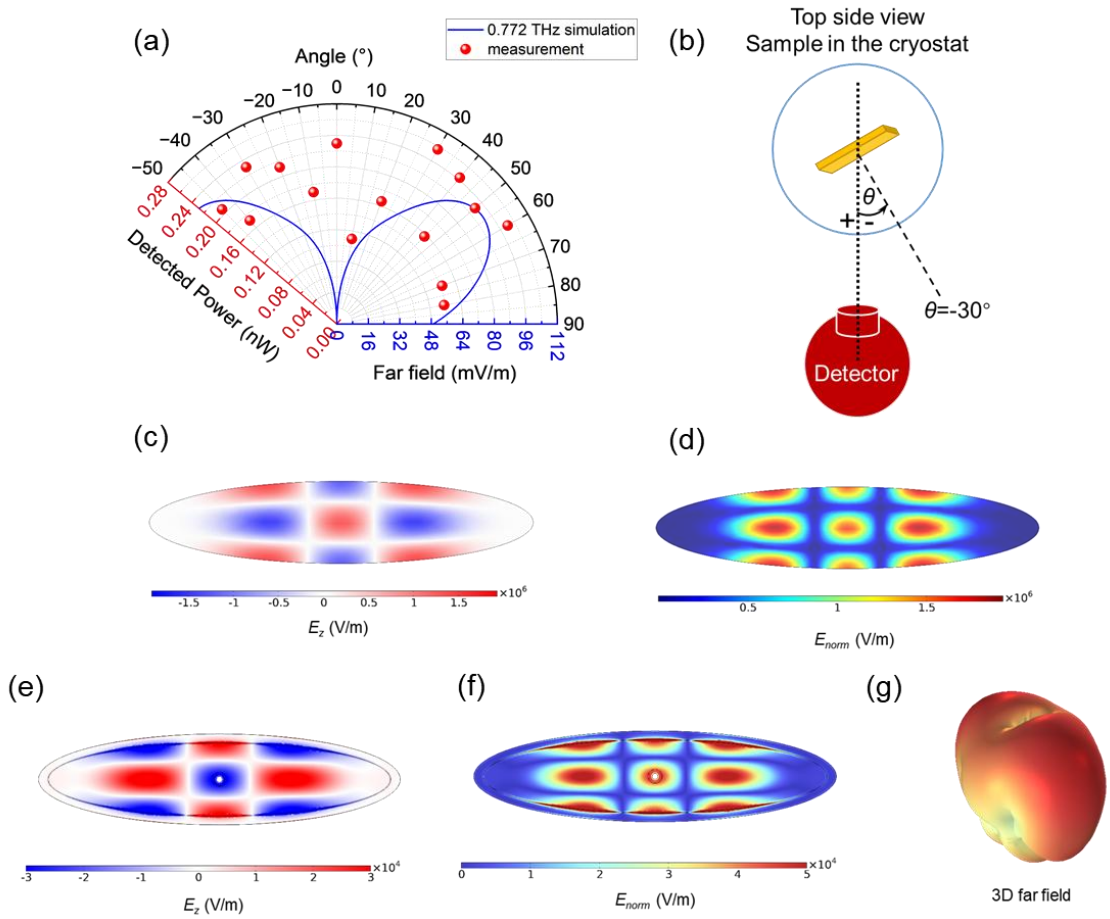



**Fig. 4.6** (a) Angle-dependent radiation pattern of device 1 from the late 2023 measurement, showing detected power through a 10cm room temperature over-the-air link (red) at $T_b$=45 K, along with the simulated 2D far-field patterns at 0.772 THz from COMSOL with central feedline. (b) The illustration of measurement angle $\theta$, which is the angle between the normal line of the device and the bolometer detector. The power is calculated from the HEB output voltage. (c) and (d) is the $z$-direction and the normal electric field for a stand-alone elliptical antenna without feedline and groove at the eigenfrequency 798.9 GHz, respectively. (e) and (f) is the $z$-direction and the normal electric field for our device with central feedline, groove, and surrounding BSCCO at 772 GHz, respectively. (g) is the 3D far-field at the same condition as (e) and (f).

distribution and far-field pattern, as shown in Figs. 4.6(e)–4.6(g) and Fig. C11. The strongest far-field pattern, plotted at 772 GHz in Fig. 4.6(a), closely resembles the measured radiation pattern. The observed 0.768–0.78 THz (2,1) mode resonance, which differs by approximately 19–30 GHz from the stand-alone mesa, is influenced by the presence of the surrounding BSCCO crystal, the groove, and the central feedline. Discrepancies between the device and the COMSOL model, including variations in the relative permittivity of BSCCO and the size and thickness of the surrounding BSCCO

crystal, may contribute to the slight frequency shift between the true radiation and the simulation.

## 4.6 Coherent THz photon radiation rate

Quantum applications in the THz regime, particularly THz quantum communication, require the ability to generate and precisely manipulate photons. Developing a coherent, stable, and tunable THz source is therefore essential, as it directly influences the feasibility of high-speed and secure quantum information transfer and processing. To analyze radiation at the photon scale, we determined the photon number $N_{\text{photon}}$ emitted by the THz source over a fixed time interval using the following calculation:

$$N_{photon} = \frac{E_d}{E_p} \tag{64}$$

with the emission energy reaching the detector

$$E_d = Pt \tag{65}$$

and the single photon energy with frequency $f$

$$E_p = hf \tag{66}$$

Here, $P$ is the power related to the HEB output voltage, as defined in Eq. (59), using the setup illustrated in Fig. C2 (b), and $t$ is time in seconds. Figures 4.7(a) and 4.7(b) show the photon number detected by the HEB from device 1 over picosecond timescales at different bath temperatures at $\theta = 0°$, shown as a function of bias voltage and frequency, respectively. As the bath temperature increases, the required bias voltage decreases. Notably, the highest photon-number rate is observed at $T_b = 30$ K, where, on average, more than 240 photons per picosecond ($ps^{-1}$) are detected after passing through an approximately 50-cm over-the-air free-space channel. A higher bath temperature of 43 K reduces the radiation rate but maintains it above 50 $ps^{-1}$, supporting high-speed communication. Additionally, as shown in Fig. 4.7(b), the photon frequency shows a general decreasing trend with increasing temperature. Frequency tunability at each temperature can be controlled by bias voltage or by selecting different branches in the

IVCs, though this also influences the photon number, particularly in the sub-100 $ps^{-1}$ range. Additional temperature-dependent results at $\theta = 30°$ and bias voltage-dependent results at $\theta = 0°$ are presented in Appendix C, Figs. C7 and C8. The above discussion is based on the detected power after an approximately 50 cm room-temperature free-space over-the-air link. To better understand the radiation power in a vacuum environment for cryogenic platform applications, such as wireless communication within quantum computers, we calculated the radiation power and photon number near the device inside the cryostat. Considering the radiation pattern in Fig. 4.6(a), the average power from −45° to 80° at the detection point is approximately 0.194 nW. The measurement solid angle is 0.02 sr. Assuming an attenuation factor of 0.75 for the cryostat window made of quartz glass in HEB [126], and THz attenuation around 750 GHz is more than 1000 dB/km [155], we estimate the radiation power from the device to be approximately 250 nW inside the cryostat, with 90% transmission of the polythene window. The total radiation photon number inside the fridge is estimated to be approximately 503 photons per femtosecond ($fs^{-1}$), considering the radiation frequency of 750 GHz. It is noted that a radiation power of approximately 250 nW is typical for this generation of coherent THz devices, without stand-alone BSCCO cavities [156].

The demonstrated THz-photon-generation capability of the proposed BSCCO THz emitter also provides a basis for considering its potential application to THz DV-QKD. Although

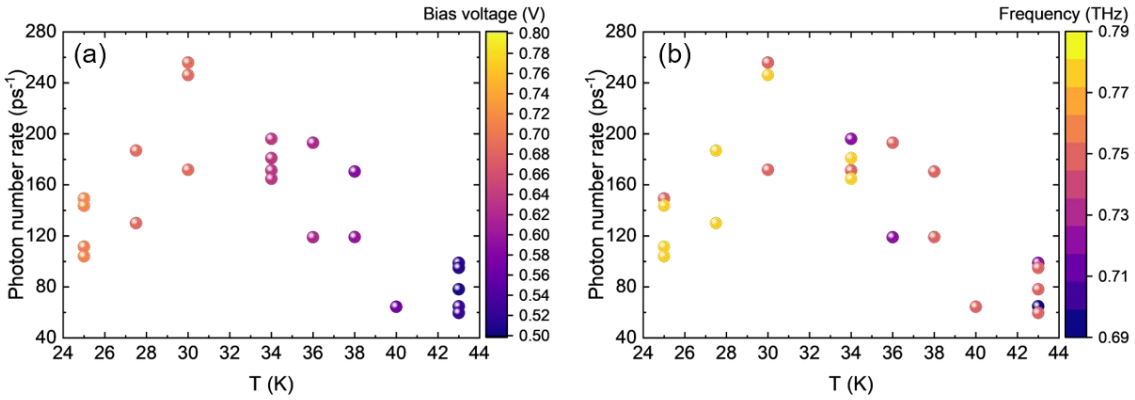



**Fig. 4.7** The detected photon number per picosecond at different bath temperatures is shown as a function of (a) bias voltage and (b) frequency, at $\theta$=0°.

the source can provide sufficient THz photon flux, its direct emission is not at the single-photon level typically associated with DV-QKD. Additional attenuation or photon-number control would therefore be required to prepare weak quantum signals suitable for DV-QKD protocols. Furthermore, thermal background photons and the limited availability of sensitive THz single-photon detectors remain important practical challenges. Nevertheless, the photon-generation capability, frequency tunability, and relatively high operating temperature of the BSCCO THz emitter make it a potential candidate for future THz DV-QKD implementations. While the current implementation remains at an early stage, this first estimation opens alternative perspectives for advancing THz quantum circuits and on-chip components based on high-temperature superconducting materials.

## 4.7 Conclusion

In conclusion, we demonstrated that a chip-scale coherent THz source based on IJJs in a high-temperature superconducting BSCCO with an elliptical cavity remains operational over 11 years post-fabrication. The emission is strong enough to propagate through a nearly half-meter combined cryogenic and over-the-air channel. Changes in the doping level of the device resulted in a higher critical temperature of up to 90 K while maintaining comparable emission power to that observed over a decade ago. The thin Ag and Au layers on top of the device effectively protected against atmospheric degradation. We successfully measured the frequency spectrum with strong intensity in the 700–800 GHz range using a Michelson interferometer at room temperature and compared the radiation pattern with simulations. Additionally, we demonstrated a method for determining the transverse mode of electromagnetic radiation using the modified Mathieu function. The evaluation of THz photon generation in the 50–260 $ps^{-1}$ range highlights the device's high-speed potential for quantum applications, while also underscoring the importance of photon-level modulation and detection. While the current implementation remains at an early stage, this first

estimation opens alternative perspectives for advancing THz quantum circuits and on-chip components based on high-temperature superconducting materials.

## 4.8 Appendix C

In this section, we provide extended details on the THz device fabrication, simulation, characterisation, and hybrid cryogenic-free-space measurement setup, as illustrated in Figs. C1–C11. Table I presents the eigenfrequency analysis based on the modified Mathieu function, employed in the modelling of BSCCO THz microcavities. The corresponding figures are presented on the following pages.

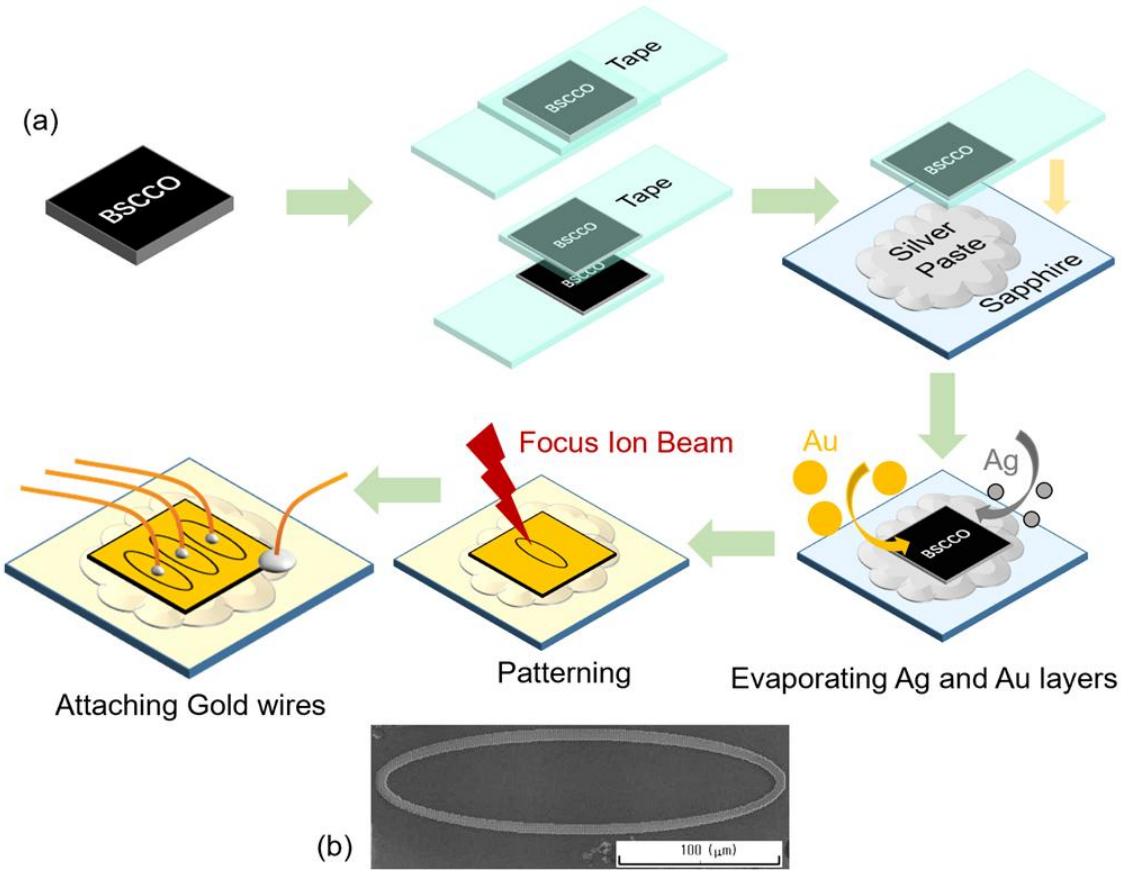



**Fig. C1** (a) Schematic illustrating the fabrication process of the coherent THz device. (b) SEM image of a single coherent THz emitter with an elliptical microcavity captured in 2012.

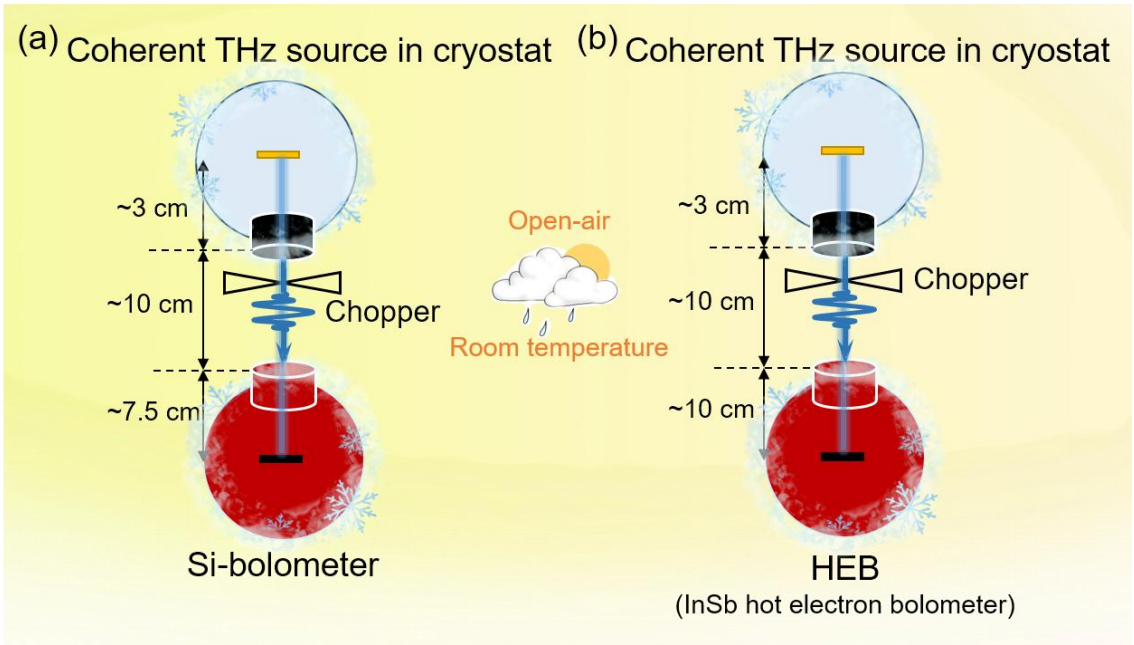



**Fig. C2** Schematic diagram of the coherent THz radiation setup, including cryogenic operation, free-space transmission at room temperature, and cryogenic detection, as implemented in (a) 2012 and (b) 2023.

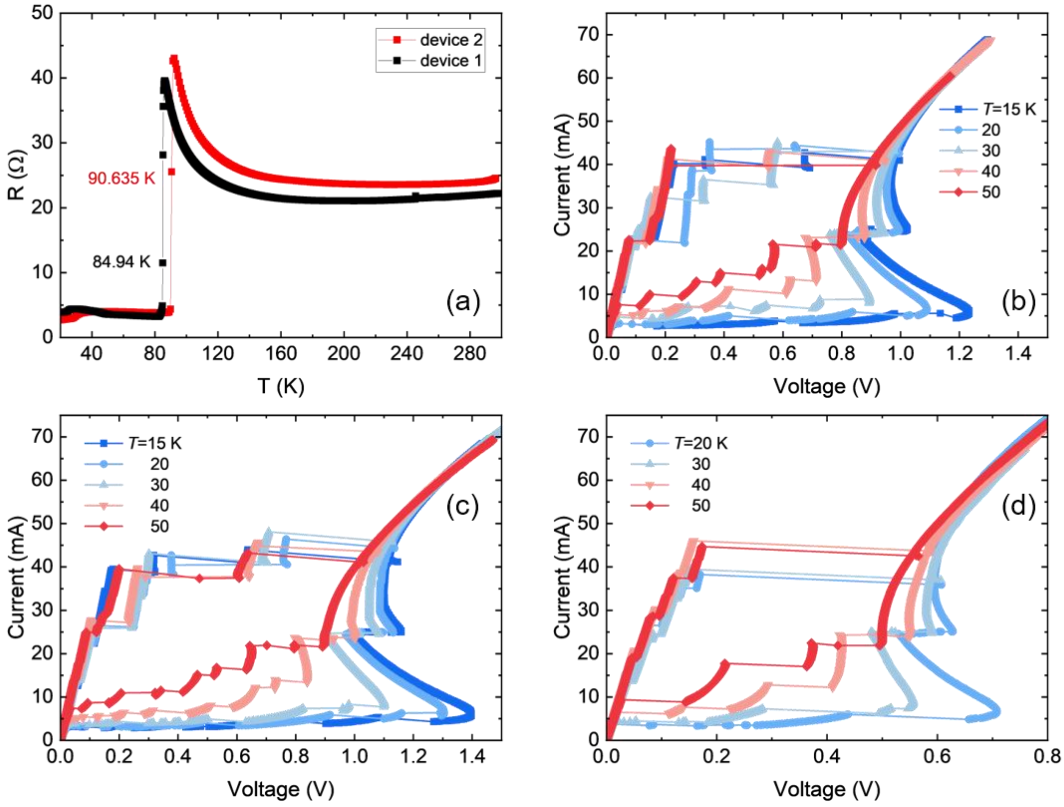



**Fig. C3** (a) The temperature-dependent resistance of the elliptical cavity device 1 and device 2 in 2012. (b) The current-voltage characteristic at different bath temperatures in 2012 for device 1. (c) The current-voltage characteristic at different bath temperatures in 2012 for device 2. (d) The current-voltage characteristic at different bath temperatures in 2012 for device 3.

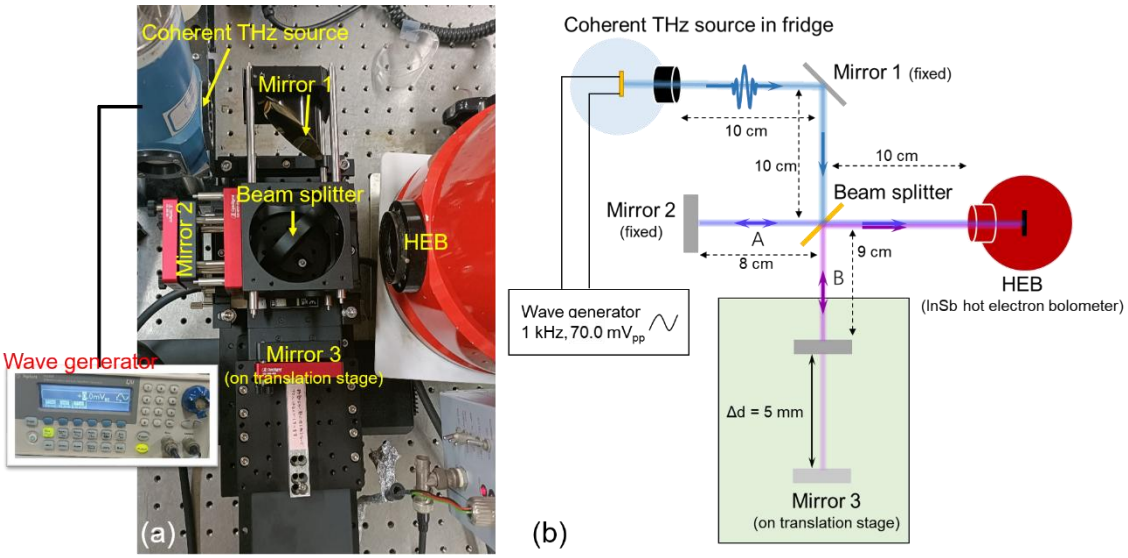



**Fig. C4** (a) The photo of the THz frequency measurement setup: hybrid cryogenic-free space room temperature over-the-air THz link. (b) The schematic of the THz frequency hybrid cryogenic-free space over-the-air testbed.

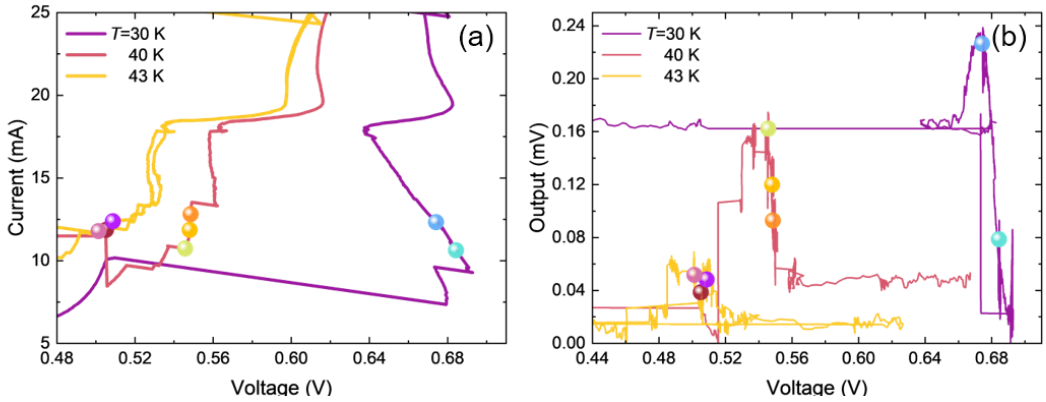



**Fig. C5** (a) The current-voltage characteristic at different bath temperatures. The highlight points are bias points for frequency measurement at $\theta$=30°. (b) The output voltage from the HEB detector at different temperatures, $\theta$=30°. The highlight points are output points for frequency measurement.

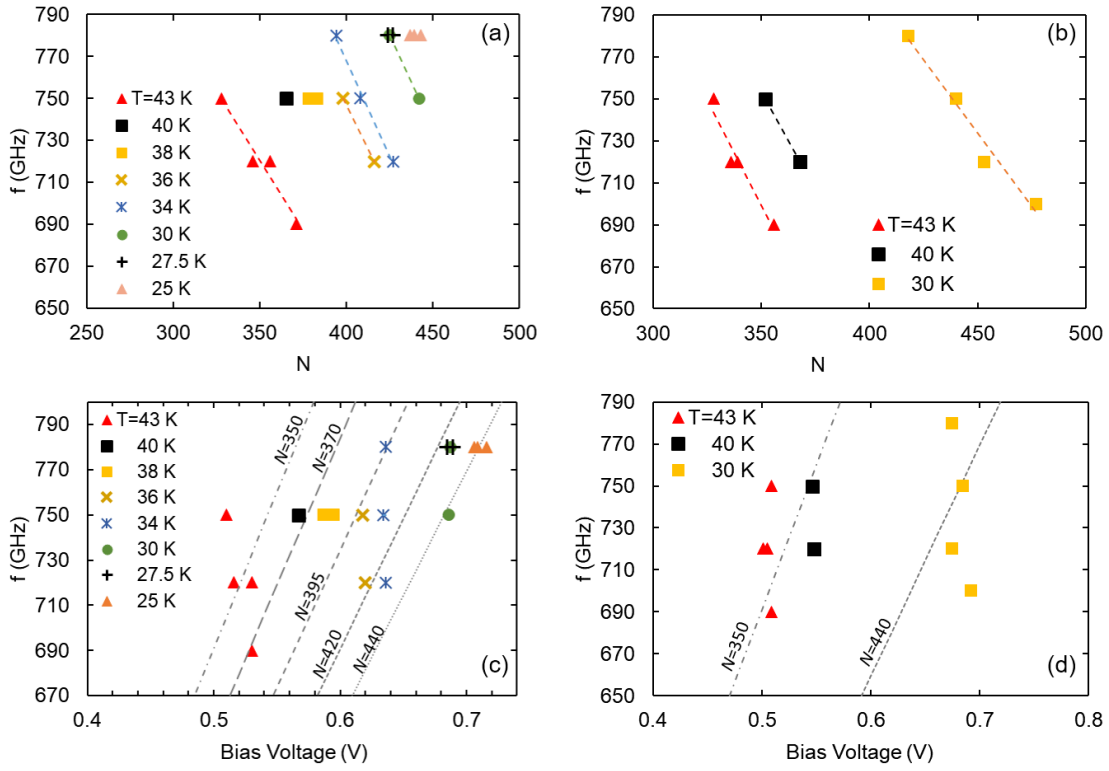



**Fig. C6** The emission frequency and the number of active Josephson junctions $N$ in device 1 calculated from the ac-Josephson relation at different bath temperatures in 2023. (a) $\theta$=0°and (b) $\theta$=30°. (c) and (d) show the frequency relations with bias voltage and the fit junction number lines at (c) $\theta$=0°and (d) $\theta$=30°.

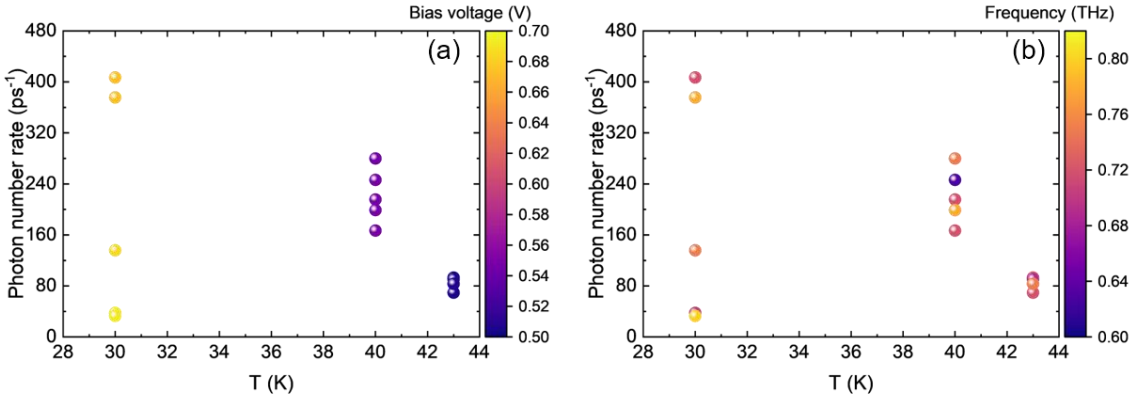



**Fig. C7** The photon number detected per picosecond at different bath temperatures, with (a) varying bias voltages and (b) different frequencies, at $\theta$=30° in 2023.

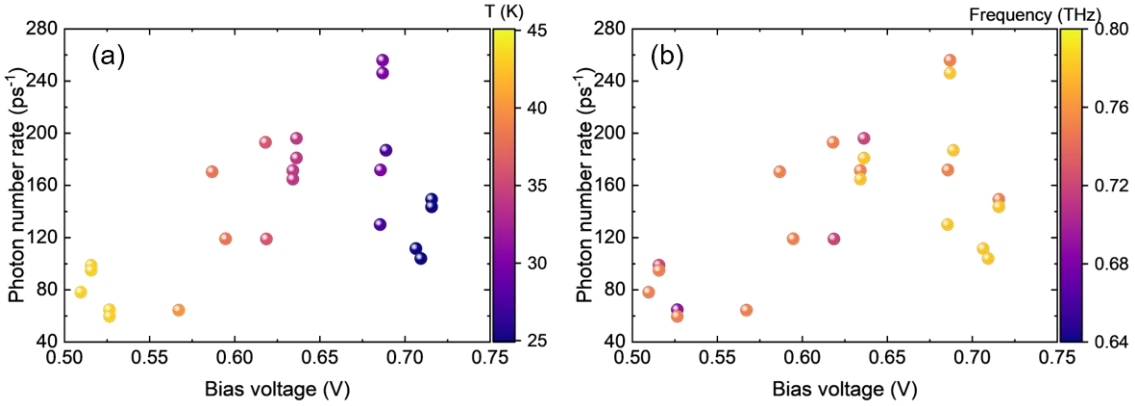



**Fig. C8** The photon number approached the detector at bias voltage per picosecond, with (a) different bath temperatures and (b) different frequencies, at $\theta$=0° in 2023.

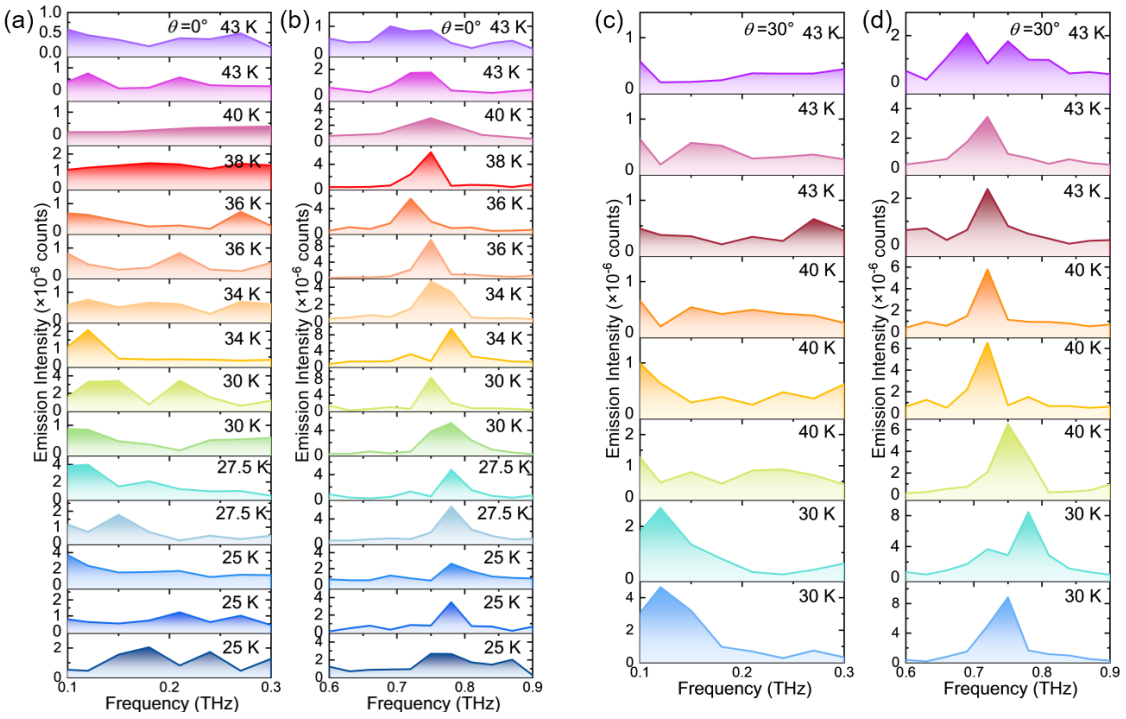



**Fig. C9** Zoom-in spectra for the elliptical cavity at different bath temperatures. (a) 0.1-0.3 THz and (c) 0.6-0.9 THz, at $\theta$=0°. The intensities are multiplied by factors of 3, 3, and 2 in 43 K and 40 K. (b) 0.1-0.3 THz and (d) 0.6-0.9 THz, at $\theta$=30°, with intensity multipliers of 3, 2, and 3 for 43 K. The intensities in all plots are offset for clarity.

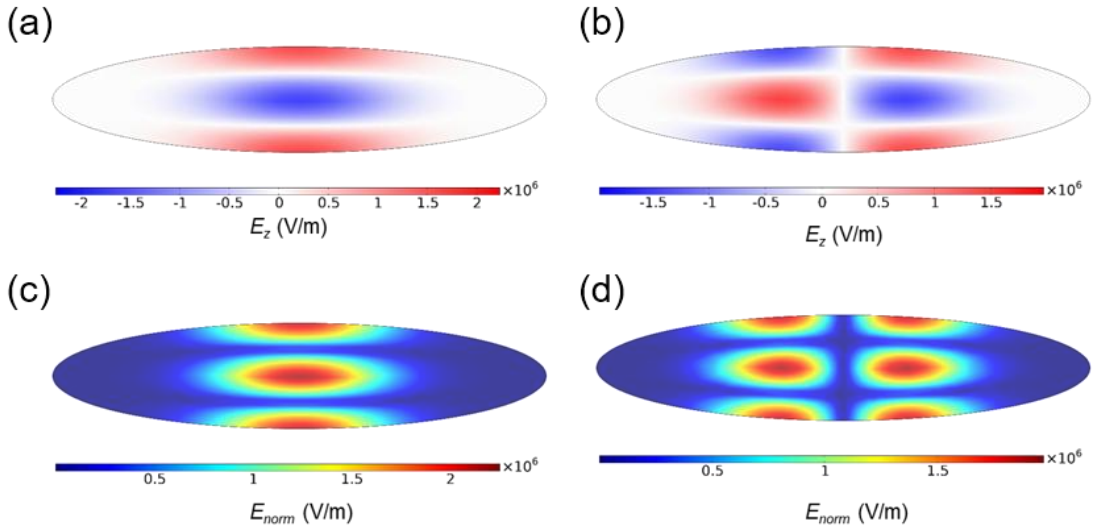



**Fig. C10** (a) and (b) are the z-direction electric field distributions for a stand-alone mesa at eigenfrequencies 701.45 GHz and 749.5 GHz, respectively. (c) and (d) is the norm electric field for a stand-alone mesa at eigenfrequencies 701.45 GHz and 749.5 GHz, respectively.

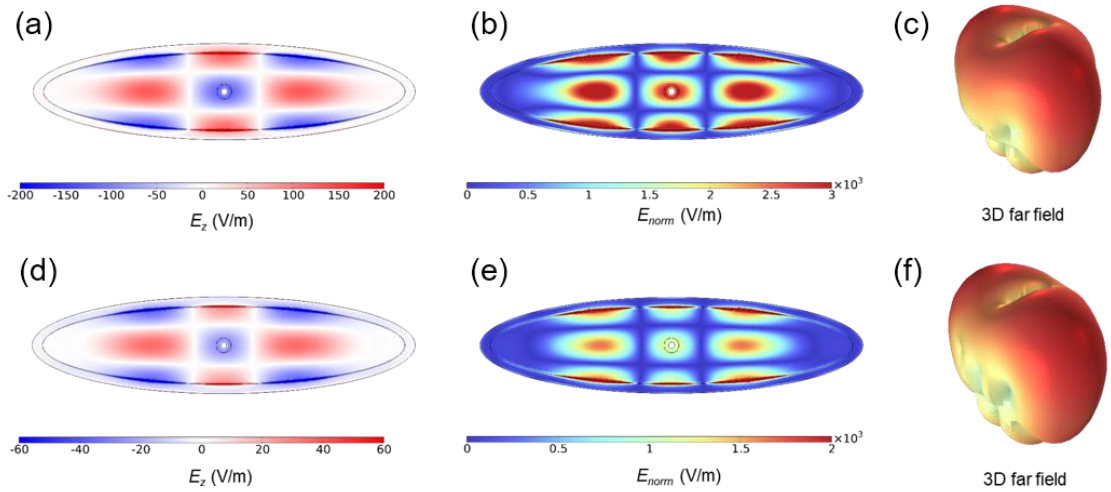



**Fig. C11** (a), (b) and (c) are the z-direction electric field, norm electric field, and 3D far field for the device simulation with central feedline and groove at 768 GHz, respectively. (d), (e) and (f) are the z-direction electric field, norm electric field, and 3D far field for the device simulation with central feedline and groove at 780 GHz, respectively.

**Table C1** Eigenfrequency analysis based on the modified Mathieu function.

| | ***m*** | ***r*** | ***q*** | ***f* (GHz)** |
|---|---|---|---|---|
| ∂Ce=0<br>Even solution | 0 | 1 | 55.20466 | 701.66 |
| | | 2 | 213.9617 | 1381.35 |
| | 1 | **1** | **62.99719** | **749.55** |
| | | 2 | 228.843 | 1428.59 |
| | 2 | **1** | **71.56025** | **798.87** |
| | | 2 | 244.4761 | 1476.58 |
| ∂Se=0<br>Odd solution | 1 | 1 | 14.6126 | 361 |
| | | 2 | 121.652 | 1041.59 |
| | 2 | 1 | 18.8 | 409.47 |
| | | 2 | 132.99 | 1089.05 |

# Chapter 5
# Conclusions and Outlook

This thesis investigated the feasibility of secure wireless quantum communication in the millimetre-wave (mm-wave) and terahertz (THz) frequency ranges by integrating quantum communication mechanisms, realistic channel and protocol modelling, and emerging superconducting THz hardware.

First, the performance of continuous-variable quantum key distribution (CVQKD) systems operating under cryogenic conditions was studied in the 100 GHz–1 THz frequency range with both single-input single-output (SISO) and multiple-input multiple-output (MIMO) schemes. The results demonstrated that positive secret key rates can be achieved at low temperatures and that MIMO architectures significantly improve secure transmission distance compared with conventional SISO systems. These findings highlight the potential of combining low-temperature operation and spatial multiplexing for future THz quantum communication networks, especially for wireless links between and inside quantum computers.

Second, a realistic OFDM-based THz CVQKD framework was developed by incorporating practical impairments, including modulation-induced excess noise and frequency-dependent atmospheric absorption. The results showed that multicarrier transmission can substantially enhance secret key generation performance compared with single-carrier systems. However, the benefits are accompanied by increased sensitivity to hardware

imperfections, emphasising the need for joint optimisation of communication protocols and THz hardware.

Finally, the thesis investigated superconducting BSCCO-based terahertz emitters as potential hardware platforms for future quantum communication systems. Experimental measurements demonstrated stable coherent THz emission more than eleven years after fabrication, confirming the long-term reliability of the device. The observed emission characteristics and photon generation capability indicate the promise of superconducting THz sources for both classical and quantum applications.

Overall, this thesis bridges the gap between THz hardware development and quantum communication schemes by providing a unified perspective that links source technology, channel characteristics, and secure communication protocols. The results support the feasibility of future high-capacity and quantum-secure wireless networks operating in the THz regime.

Although the results presented in this thesis demonstrate the potential of THz quantum communication, several challenges remain.

Future work should focus on the experimental implementation of THz CVQKD systems using superconducting sources and integrated circuits. Further development of integrated THz components, including waveguides, modulators, detectors, and transceiver architectures, will be essential for practical deployment. In addition, combining MIMO or multicarrier techniques within a unified framework may further improve communication capacity and transmission range. More realistic channel models incorporating atmospheric turbulence, non-line-of-sight links (NLOS) and dynamic environmental effects should also be investigated.

As THz hardware continues to advance, particularly in superconducting and quantum-compatible technologies, the integration of secure communication, sensing, quantum information processing, and quantum communication software is expected to become an important research direction. The results presented in this thesis provide a foundation for these future developments and contribute toward the realisation of practical THz quantum networks.

# References


[1] T. Nagatsuma, S. Horiguchi, Y. Minamikata, Y. Yoshimizu, S. Hisatake, S. Kuwano, N. Yoshimoto, J. Terada, and H. Takahashi, "Terahertz wireless communications based on photonics technologies," *Optics Express,* vol. 21, no. 20, pp. 23736–23747, 2013.

[2] D. M. M. Thomas Kürner, Tadao Nagatsuma, *THz Communications: Paving the Way Towards Wireless Tbps*. Springer ISBN: 978-3-030-73738-2.

[3] Z. T. Ma, Z. X. Geng, Z. Y. Fan, J. Liu, and H. D. Chen, "Modulators for Terahertz Communication: The Current State of the Art," *Research,* vol. 2019, 2019.

[4] Z. Chen, X. Ma, B. Zhang, Y. Zhang, Z. Niu, N. Kuang, W. Chen, L. Li, and S. Li, "A survey on terahertz communications," *China Communications,* vol. 16, no. 2, pp. 1–35, 2019.

[5] Z. Chen, C. Han, Y. Wu, L. Li, C. Huang, Z. Zhang, G. Wang, and W. Tong, "Terahertz Wireless Communications for 2030 and Beyond: A Cutting-Edge Frontier," *IEEE Communications Magazine,* vol. 59, no. 11, pp. 66–72, 2021.

[6] H. Sarieddeen, M. S. Alouini, and T. Y. Al-Naffouri, "An Overview of Signal Processing Techniques for Terahertz Communications," *Proceedings of the IEEE,* vol. 109, no. 10, pp. 1628–1665, 2021.

[7] H. J. Song and T. Nagatsuma, "Present and Future of Terahertz Communications," *IEEE Transactions on Terahertz Science and Technology,* vol. 1, no. 1, pp. 256–263, 2011.

[8] Y. H. Yang, M. Mandehgar, and D. R. Grischkowsky, "Broadband THz Signals Propagate Through Dense Fog," *IEEE Photonics Technology Letters,* vol. 27, no. 4, pp. 383–386, 2015.

[9] K. Su, L. Moeller, R. B. Barat, and J. F. Federici, "Experimental comparison of terahertz and infrared data signal attenuation in dust clouds," *J. Opt. Soc. Am. A,* vol. 29, no. 11, pp. 2360–2366, 2012.

[10] I. F. Akyildiz, C. Han, Z. Hu, S. Nie, and J. M. Jornet, "Terahertz Band Communication: An Old Problem Revisited and Research Directions for the Next Decade," *IEEE Transactions on Communications,* vol. 70, no. 6, pp. 4250–4285, 2022.

[11] R. H. Caverly, "Breakthroughs in Microwaves: Programmable Terahertz Chip-Scale Surfaces and Systems—An Interview With Dr. Kaushik Sengupta," *IEEE Journal of Microwaves,* vol. 1, no. 4, pp. 853–863, 2021.

[12] H. Elayan, O. Amin, R. M. Shubair, and M. S. Alouini, "Terahertz communication: The opportunities of wireless technology beyond 5G," in *2018 International Conference on Advanced Communication Technologies and Networking (CommNet)*, 2–4 April 2018 2018, pp. 1–5.

[13] M. J. Fitch and R. Osiander, "Terahertz waves for communications and sensing," *JOHNS HOPKINS APL TECHNICAL DIGEST,* vol. 25, no. 4, pp. 348–355, 2004.

[14] K. Kadowaki, M. Tsujimoto, K. Delfanazari, T. Kitamura, M. Sawamura, H. Asai, T. Yamamoto, K. Ishida, C. Watanabe, S. Sekimoto, K. Nakade, T. Yasui, K. Asanuma, T. Kashiwagi, H. Minami, M. Tachiki, T. Hattori, and R. A. Klemm, "Quantum terahertz electronics (QTE) using coherent radiation from high temperature superconducting $Bi_2Sr_2CaCu_2O_{8+\delta}$ intrinsic Josephson junctions," *Physica C: Superconductivity,* vol. 491, pp. 2–6, 2013.

[15] K. Delfanazari, R. A. Klemm, H. J. Joyce, D. A. Ritchie, and K. Kadowaki, "Integrated, Portable, Tunable, and Coherent Terahertz Sources and Sensitive Detectors Based on Layered Superconductors," *Proceedings of the IEEE,* vol. 108, no. 5, pp. 721–734, 2020.

[16] K. Delfanazari, H. Asai, M. Tsujimoto, T. Kashiwagi, T. Kitamura, K. Ishida, C. Watanabe, S. Sekimoto, T. Yamamoto, H. Minami, M. Tachiki, R. A. Klemm, T. Hattori, and K. Kadowaki, "Terahertz Oscillating Devices Based Upon the Intrinsic Josephson Junctions in a High Temperature Superconductor," *Journal of Infrared, Millimeter, and Terahertz Waves,* vol. 35, no. 1, pp. 131–146, 2014.

[17] K. Delfanazari, H. Asai, M. Tsujimoto, T. Kashiwagi, T. Kitamura, M. Sawamura, K. Ishida, T. Yamamoto, T. Hattori, R. A. Klemm, K. Kadowaki, and IEEE, "Experimental and Theoretical Studies of Mesas of Several Geometries for Terahertz Wave Radiation from the Intrinsic Josephson Junctions in Superconducting $Bi_2Sr_2CaCu_2O_{8+\delta}$ " in *37th International Conference on Infrared, Millimeter, and Terahertz Waves (IRMMW-THz)*, Univ Wollongong, Wollongong, AUSTRALIA, Sep 23–28 2012, in International Conference on Infrared Millimeter and Terahertz Waves, 2012,

[18] M. Tsujimoto, T. Yamamoto, K. Delfanazari, R. Nakayama, T. Kitamura, M. Sawamura, T. Kashiwagi, H. Minami, M. Tachiki, K. Kadowaki, and R. A. Klemm, "Broadly Tunable Subterahertz Emission from Internal Branches of the Current-Voltage Characteristics of Superconducting $Bi_2Sr_2CaCu_2O_{8+\delta}$ Single Crystals," *Physical Review Letters,* vol. 108, no. 10, 2012.

[19] K. Delfanazari, H. Asai, M. Tsujimoto, T. Kashiwagi, T. Kitamura, T. Yamamoto, M. Sawamura, K. Ishida, C. Watanabe, S. Sekimoto, H. Minami, M. Tachiki, R. A. Klemm, T. Hattori, and K. Kadowaki, "Tunable terahertz emission from the intrinsic Josephson junctions in acute isosceles triangular $Bi_2Sr_2CaCu_2O_{8+\delta}$ mesas," *Optics Express,* vol. 21, no. 2, pp. 2171–2184, 2013.

[20] T. Kashiwagi, M. Tsujimoto, T. Yamamoto, H. Minami, K. Yamaki, K. Delfanazari, K. Deguchi, N. Orita, T. Koike, R. Nakayama, T. Kitamura, M. Sawamura, S. Hagino, K. Ishida, K. Ivanovic, H. Asai, M. Tachiki, R. A. Klemm, and K. Kadowaki, "High Temperature Superconductor Terahertz Emitters: Fundamental Physics and Its Applications," *Japanese Journal of Applied Physics,* vol. 51, no. 1, 2012.

[21] T. Kashiwagi, T. Yamamoto, H. Minami, M. Tsujimoto, R. Yoshizaki, K. Delfanazari, T. Kitamura, C. Watanabe, K. Nakade, T. Yasui, K. Asanuma, Y. Saiwai, Y. Shibano, T. Enomoto, H. Kubo, K. Sakamoto, T. Katsuragawa, B. Marković, J. Mirković, R. A. Klemm, and K. Kadowaki, "Efficient Fabrication of Intrinsic-Josephson-Junction Terahertz Oscillators with Greatly Reduced Self-Heating Effects," *Physical Review Applied,* vol. 4, no. 5, p. 054018, 2015.

[22] T. Kashiwagi, T. Yuasa, G. Kuwano, T. Yamamoto, M. Tsujimoto, H. Minami, and K. Kadowaki, "Study of Radiation Characteristics of Intrinsic Josephson Junction Terahertz Emitters with Different Thickness of $Bi_2Sr_2CaCu_2O_{8+\delta}$ Crystals," *Materials*, vol. 14, no. 5.

[23] K. Delfanazari, H. Asai, M. Tsujimoto, T. Kashiwagi, T. Kitamura, T. Yamamoto, W. Wilson, R. A. Klemm, T. Hattori, and K. Kadowaki, "Effect of Bias Electrode Position on Terahertz Radiation From Pentagonal Mesas of Superconducting $Bi_2Sr_2CaCu_2O_{8+\delta}$," *IEEE Transactions on Terahertz Science and Technology,* vol. 5, no. 3, pp. 505–511, 2015.

[24] Y. Xiong, T. Kashiwagi, R. A. Klemm, K. Kadowaki, and K. Delfanazari, "Engineering the Cavity modes and Polarization in Integrated Superconducting Coherent Terahertz Emitters," in *2020 45th International Conference on Infrared, Millimeter, and Terahertz Waves (IRMMW-THz)*, 8–13 Nov. 2020 2020, pp. 1–2.

[25] K. Delfanazari, H. Asai, M. Tsujimoto, T. Kashiwagi, T. Kitamura, T. Yamamoto, M. Sawamura, K. Ishida, M. Tachiki, R. A. Klemm, T. Hattori, and K. Kadowaki, "Study of coherent and continuous terahertz wave emission in equilateral triangular mesas of superconducting $Bi_2Sr_2CaCu_2O_{8+\delta}$ intrinsic Josephson junctions," *Physica C-Superconductivity and Its Applications,* vol. 491, pp. 16–19, 2013.

[26] Y. Saiwai, T. Kashiwagi, K. Nakade, M. Tsujimoto, H. Minami, R. A. Klemm, and K. Kadowaki, "Liquid helium-free high-Tc superconducting terahertz emission system and its applications," *Japanese Journal of Applied Physics,* vol. 59, no. 10, p. 105004, 2020.

[27] K. A. Fedorova, H. Guoyu, M. Wichmann, C. Kriso, F. Zhang, W. Stolz, M. Scheller, M. Koch, and A. Rahimi-Iman, "Widely Tunable Terahertz-Generating Semiconductor Disk Laser," *physica status solidi (RRL) – Rapid Research Letters,* vol. 14, no. 10, p. 2000204, 2020.

[28] R. Cattaneo, E. A. Borodianskyi, A. A. Kalenyuk, and V. M. Krasnov, "Superconducting Terahertz Sources with 12% Power Efficiency," *Physical Review Applied,* vol. 16, no. 6, 2021.

[29] K. Yamaki, M. Tsujimoto, T. Yamamoto, A. Furukawa, T. Kashiwagi, H. Minami, and K. Kadowaki, "High-power terahertz electromagnetic wave emission from high-Tc superconducting Bi2Sr2CaCu2O8+δ mesa structures," *Optics Express,* vol. 19, no. 4, pp. 3193–3201, 2011.

[30] J. R. Rain, P. Cai, A. Baekey, M. A. Reinhard, R. I. Vasquez, A. C. Silverman, C. L. Cain, and R. A. Klemm, "Wave functions for high-symmetry, thin microstrip antennas, and two-dimensional quantum boxes," *Physical Review A,* vol. 104, no. 6, p. 062205, 2021.

[31] Y. Xiong and K. Delfanazari, "Engineering Circular Polarization in Chip-integrated High-Tc Superconducting THz Antennas," in *2021 Photonics & Electromagnetics Research Symposium (PIERS)*, 21–25 Nov. 2021 2021, pp. 1016–1019.

[32] Y. Xie, N. Bai, W. Hong, and X. Sun, "Study of a hexagonal lattice defect photonic crystal waveguide slow wave structure for G-band traveling wave tube," *Journal of Electromagnetic Waves and Applications,* vol. 36, no. 6, pp. 843–855, 2022.

[33] D. P. Cerkoney, C. Reid, C. M. Doty, A. Gramajo, T. D. Campbell, M. A. Morales, K. Delfanazari, M. Tsujimoto, T. Kashiwagi, T. Yamamoto, C. Watanabe, H. Minami, K. Kadowaki, and R. A. Klemm, "Cavity mode enhancement of terahertz emission from equilateral triangular microstrip antennas of the high-Tc superconductor $Bi_2Sr_2CaCu_2O_{8+\delta}$," *Journal of Physics: Condensed Matter,* vol. 29, no. 1, p. 015601, 2017.

[34] R. A. Klemm, K. Delfanazari, M. Tsujimoto, T. Kashiwagi, T. Kitamura, T. Yamamoto, M. Sawamura, K. Ishida, T. Hattori, and K. Kadowaki, "Modeling the electromagnetic cavity mode contributions to the THz emission from triangular $Bi_2Sr_2CaCu_2O_{8+\delta}$ mesas," *Physica C: Superconductivity,* vol. 491, pp. 30–34, 2013.

[35] S. Kalhor, M. Ghanaatshoar, T. Kashiwagi, K. Kadowaki, M. J. Kelly, and K. Delfanazari, "Thermal Tuning of High-T-c Superconducting $Bi_2Sr_2CaCu_2O_{8+\delta}$ Terahertz Metamaterial," *IEEE Photonics Journal,* vol. 9, no. 5, 2017.

[36] R. Degl'Innocenti, H. Lin, and M. Navarro-Cía, "Recent progress in terahertz metamaterial modulators," vol. 11, no. 8, pp. 1485–1514, 2022.

[37] V. Savinov, K. Delfanazari, V. A. Fedotov, and N. I. Zheludev, "Giant nonlinearity in a superconducting sub-terahertz metamaterial," *Applied Physics Letters,* vol. 108, no. 10, p. 101107, 2016.

[38] A. S. Malishevskii and S. A. Uryupin, "On Cherenkov excitation of electromagnetic waves by vortex travelling in Josephson sandwich," *Physica Scripta,* vol. 97, no. 5, p. 055817, 2022.

[39] S. Kalhor, S. J. Kindness, R. Wallis, H. E. Beere, M. Ghanaatshoar, R. Degl'Innocenti, M. J. Kelly, S. Hofmann, H. J. Joyce, D. A. Ritchie, and K. Delfanazari, "Active Terahertz Modulator and Slow Light Metamaterial Devices with Hybrid Graphene-Superconductor Photonic Integrated Circuits," *Nanomaterials,* vol. 11, no. 11, 2021.

[40] A. Squires, X. Gao, T. van der Laan, Z. Han, and J. Du, "Adding a Tuneable Response to a Terahertz Metasurface Using a Graphene Thin Film," *Journal of Infrared, Millimeter, and Terahertz Waves,* vol. 43, no. 9, pp. 806–818, 2022.

[41] S. Kalhor, S. J. Kindness, R. Wallis, H. E. Beere, M. Ghanaatshoar, R. Degl'Innocenti, M. J. Kelly, S. Hofmann, H. J. Joyce, D. A. Ritchie, and K. Delfanazari, "Active Terahertz Modulator and Slow Light Metamaterial Devices with Hybrid Graphene-superconductor Coupled Split-ring Resonator Arrays," in *2022 Photonics & Electromagnetics Research Symposium (PIERS)*, 25–29 April 2022, pp. 967–971.

[42] S. J. Kindness, N. W. Almond, W. Michailow, B. Wei, K. Delfanazari, P. Braeuninger-Weimer, S. Hofmann, H. E. Beere, D. A. Ritchie, and R. Degl'Innocenti, "A Terahertz Chiral Metamaterial Modulator," *Advanced Optical Materials,* vol. 8, no. 21, p. 2000581, 2020.

[43] C. Li, Y. Teng, S. Duan, Y. Xiao, Y. Jiang, R. Su, M. Yu, Y. Juan, M. Hua, J. He, and L. Jiang, "Electrically terahertz switchable device based on superconducting composite structure metamaterial," *Applied Physics Letters,* vol. 121, no. 3, p. 031702, 2022.

[44] S. J. Kindness, N. W. Almond, W. Michailow, B. Wei, L. A. Jakob, K. Delfanazari, P. Braeuninger-Weimer, S. Hofmann, H. E. Beere, D. A. Ritchie, and R. Degl'Innocenti, "Graphene-Integrated Metamaterial Device for All-Electrical Polarization Control of Terahertz Quantum Cascade Lasers," *ACS Photonics,* vol. 6, no. 6, pp. 1547–1555, 2019.

[45] K. Delfanazari, "Ultrafast Terahertz Superconductor Van der Waals Metamaterial Photonic Switch," *Advanced Photonics Research,* vol. 5, no. 10, p. 2400045, 2024.

[46] S. Kalhor and K. Delfanazari, "Ultrafast Terahertz Dynamics in Hybrid Van der Waals Superconductor-Topological Insulator Metamaterials," *Advanced Photonics Research,* vol. 7, no. 4, p. e202500195, 2026.

[47] S. Kalhor, S. Kar, R. Singh, and K. Delfanazari, "Topological Photonic Devices and Circuits at Terahertz Frequencies," *Laser & Photonics Reviews,* vol. 20, no. 7, p. e03162, 2026.

[48] F. Sizov and A. Rogalski, "THz detectors," *Progress in Quantum Electronics,* vol. 34, no. 5, pp. 278–347, 2010.

[49] S. Castilla, B. Terrés, M. Autore, L. Viti, J. Li, A. Y. Nikitin, I. Vangelidis, K. Watanabe, T. Taniguchi, E. Lidorikis, M. S. Vitiello, R. Hillenbrand, K.-J. Tielrooij, and F. H. L. Koppens, "Fast and Sensitive Terahertz Detection Using an Antenna-Integrated Graphene pn Junction," *Nano Letters,* vol. 19, no. 5, pp. 2765–2773, 2019.

[50] R. A. Lewis, "A review of terahertz detectors," *Journal of Physics D: Applied Physics,* vol. 52, no. 43, p. 433001, 2019.

[51] T. Schneider, A. Wiatrek, S. Preussler, M. Grigat, and R. P. Braun, "Link Budget Analysis for Terahertz Fixed Wireless Links," *IEEE Transactions on Terahertz Science and Technology,* vol. 2, no. 2, pp. 250–256, 2012.

[52] J. Y. Sun, F. J. Hu, and S. Lucyszyn, "Predicting Atmospheric Attenuation Under Pristine Conditions Between 0.1 and 100 THz," *IEEE Access,* vol. 4, pp. 9377–9399, 2016.

[53] C. Ottaviani, M. J. Woolley, M. Erementchouk, J. F. Federici, P. Mazumder, S. Pirandola, and C. Weedbrook, "Terahertz Quantum Cryptography," *IEEE Journal on Selected Areas in Communications,* vol. 38, no. 3, pp. 483–495, 2020.

[54] S. Pirandola, U. L. Andersen, L. Banchi, M. Berta, D. Bunandar, R. Colbeck, D. Englund, T. Gehring, C. Lupo, C. Ottaviani, J. L. Pereira, M. Razavi, J. S. Shaari, M. Tomamichel, V. C. Usenko, G. Vallone, P. Villoresi, and P. Wallden, "Advances in quantum cryptography," *Advances in Optics and Photonics,* vol. 12, no. 4, pp. 1012–1236, 2020.

[55] S. Pirandola, R. Laurenza, C. Ottaviani, and L. Banchi, "Fundamental limits of repeaterless quantum communications," *Nature Communications,* vol. 8, 2017.

[56] S. Pirandola, "Composable security for continuous variable quantum key distribution: Trust levels and practical key rates in wired and wireless networks," *Physical Review Research,* vol. 3, no. 4, p. 043014, 2021.

[57] H.-K. Lo and H. F. Chau, "Unconditional Security of Quantum Key Distribution over Arbitrarily Long Distances," *Science,* vol. 283, no. 5410, pp. 2050–2056, 1999.

[58] C. J. Liu, C. H. Zhu, X. Liu, M. Nie, H. Yang, and C. X. Pei, "Multicarrier Multiplexing Continuous-Variable Quantum Key Distribution at Terahertz Bands Under Indoor Environment and in Inter-Satellite Links Communication," *IEEE Photonics Journal,* vol. 13, no. 4, 2021.

[59] N. K. Kundu, M. R. McKay, and R. K. Mallik, "Wireless quantum key distribution at terahertz frequencies: Opportunities and challenges," *IET Quantum Communication,* vol. n/a, no. n/a, 2024.

[60] R. H. Shi, J. J. Shi, Y. Guo, X. Q. Peng, and M. H. Lee, "Quantum MIMO Communication Scheme Based on Quantum Teleportation with Triplet States," *International Journal of Theoretical Physics,* vol. 50, no. 8, pp. 2334–2346, 2011.

[61] N. K. Kundu, S. P. Dash, M. R. McKay, and R. K. Mallik, "MIMO Terahertz Quantum Key Distribution," *IEEE Communications Letters,* vol. 25, no. 10, pp. 3345–3349, 2021.

[62] H. Zhang, Y. Mao, D. Huang, J. Li, L. Zhang, and Y. Guo, "Security analysis of orthogonal-frequency-division-multiplexing--based continuous-variable quantum key distribution with imperfect modulation," *Physical Review A,* vol. 97, no. 5, p. 052328, 2018.

[63] M. A. Belkin, Q. J. Wang, C. Pflugl, A. Belyanin, S. P. Khanna, A. G. Davies, E. H. Linfield, and F. Capasso, "High-Temperature Operation of Terahertz Quantum Cascade Laser Sources," *IEEE Journal of Selected Topics in Quantum Electronics,* vol. 15, no. 3, pp. 952–967, 2009.

[64] M. Asada and S. Suzuki, "Terahertz Emitter Using Resonant-Tunneling Diode and Applications," *Sensors,* vol. 21, no. 4, 2021.

[65] E. A. Borodianskyi and V. M. Krasnov, "Josephson emission with frequency span 1–11 THz from small $Bi_2Sr_2CaCu_2O_{8+\delta}$ mesa structures," *Nature Communications,* vol. 8, no. 1, p. 1742, 2017.

[66] H. Sun, S. Chen, Y.-L. Wang, G. Sun, J. Chen, T. Hatano, V. P. Koshelets, D. Koelle, R. Kleiner, H. Wang, and P. Wu, "Compact High-Tc Superconducting Terahertz Emitter with Tunable Frequency from 0.15 to 1 THz," *Applied Sciences*, vol. 13, no. 6.

[67] L. Ozyuzer, A. E. Koshelev, C. Kurter, N. Gopalsami, Q. Li, M. Tachiki, K. Kadowaki, T. Yamamoto, H. Minami, H. Yamaguchi, T. Tachiki, K. E. Gray, W. K. Kwok, and U. Welp, "Emission of Coherent THz Radiation from Superconductors," *Science,* vol. 318, no. 5854, pp. 1291–1293, 2007.

[68] M. Zhang, S. Nakagawa, Y. Enomoto, Y. Kuzumi, R. Kikuchi, Y. Yamauchi, T. Hattori, R. A. Klemm, K. Kadowaki, T. Kashiwagi, and K. Delfanazari, "Tunable terahertz source on a chip with decade-long stability using layered-superconductor elliptical microcavities," *Physical Review Applied,* vol. 24, no. 5, p. 054012, 2025.

[69] K. J. Kihlstrom, K. C. Reddy, S. Elghazoly, T. E. Sharma, A. E. Koshelev, U. Welp, Y. Hao, R. Divan, M. Tsujimoto, K. Kadowaki, W. K. Kwok, and T. M. Benseman, "Powerful Terahertz Emission from a $Bi_2Sr_2CaCu_2O_{8+\delta}$ Mesa Operating Above 77 K," *Physical Review Applied,* vol. 19, no. 3, p. 034055, 2023.

[70] H. Minami, C. Watanabe, T. Kashiwagi, T. Yamamoto, K. Kadowaki, and R. A. Klemm, "0.43 THz emission from high-Tc superconducting emitters optimized at 77 K," *Journal of Physics: Condensed Matter,* vol. 28, no. 2, p. 025701, 2016.

[71] B. D. Josephson, "Possible new effects in superconductive tunnelling," *Physics Letters,* vol. 1, no. 7, pp. 251–253, 1962.

[72] M. Tsujimoto, K. Yamaki, K. Deguchi, T. Yamamoto, T. Kashiwagi, H. Minami, M. Tachiki, K. Kadowaki, and R. A. Klemm, "Geometrical Resonance Conditions for THz Radiation from the Intrinsic Josephson Junctions in $Bi_2Sr_2CaCu_2O_{8+\delta}$," *Physical Review Letters,* vol. 105, no. 3, p. 037005, 2010.

[73] H. B. Wang, S. Guénon, B. Gross, J. Yuan, Z. G. Jiang, Y. Y. Zhong, M. Grünzweig, A. Iishi, P. H. Wu, T. Hatano, D. Koelle, and R. Kleiner, "Coherent Terahertz Emission of Intrinsic Josephson Junction Stacks in the Hot Spot Regime," *Physical Review Letters,* vol. 105, no. 5, p. 057002, 2010.

[74] S. Guénon, M. Grünzweig, B. Gross, J. Yuan, Z. G. Jiang, Y. Y. Zhong, M. Y. Li, A. Iishi, P. H. Wu, T. Hatano, R. G. Mints, E. Goldobin, D. Koelle, H. B. Wang, and R. Kleiner, "Interaction of hot spots and terahertz waves in ${\text{Bi}}_{2}{\text{Sr}}_{2}{\text{CaCu}}_{2}{\text{O}}_{8}$ intrinsic Josephson junction stacks of various geometry," *Physical Review B,* vol. 82, no. 21, p. 214506, 2010.

[75] S. Kalhor, M. Ghanaatshoar, and K. Delfanazari, "On-chip Superconducting THz Metamaterial Bandpass Filter," in *2020 45th International Conference on Infrared, Millimeter, and Terahertz Waves (IRMMW-THz)*, 8–13 Nov. 2020 2020, pp. 1–2.

[76] K. Yang, S. Liu, S. Arezoomandan, A. Nahata, and B. Sensale-Rodriguez, "Graphene-based tunable metamaterial terahertz filters," *Applied Physics Letters,* vol. 105, no. 9, p. 093105, 2014.

[77] I. J. H. McCrindle, J. Grant, T. D. Drysdale, and D. R. S. Cumming, "Multi-Spectral Materials: Hybridisation of Optical Plasmonic Filters and a Terahertz Metamaterial Absorber," *Advanced Optical Materials,* vol. 2, no. 2, pp. 149–153, 2014.

[78] S. Kalhor, M. Ghanaatshoar, H. J. Joyce, D. A. Ritchie, K. Kadowaki, and K. Delfanazari, "Millimeter-Wave-to-Terahertz Superconducting Plasmonic Waveguides for Integrated Nanophotonics at Cryogenic Temperatures," *Materials,* vol. 14, no. 15, 2021.

[79] S. Atakaramians, S. Afshar V, T. M. Monro, and D. Abbott, "Terahertz dielectric waveguides," *Advances in Optics and Photonics,* vol. 5, no. 2, pp. 169–215, 2013.

[80] S. Kalhor, M. Ghanaatshoar, and K. Delfanazari, "Guiding of terahertz photons in superconducting nano-circuits," in *2020 International Conference on UK-China Emerging Technologies (UCET)*, 20–21 Aug. 2020 2020, pp. 1–3.

[81] G. Gallot, S. P. Jamison, R. W. McGowan, and D. Grischkowsky, "Terahertz waveguides," *J. Opt. Soc. Am. B,* vol. 17, no. 5, pp. 851–863, 2000.

[82] K. Wang and D. M. Mittleman, "Metal wires for terahertz wave guiding," *Nature,* vol. 432, no. 7015, pp. 376–379, 2004.

[83] M. Zhang, Foshat, P., Poorgholam Khanjari, S., Imran, M. , Weides, M. and Delfanazari, K, "Microwave Quantum Key Distribution with Cryogenic Microwave Components for Superconducting Quantum Computing," presented at the 2022 International Symposium on Quantum Computing: Circuits Systems Automation and Applications (QC-CSAA), Knoxville, TN, USA, 18–19 July 2022.

[84] P. Magnard, S. Storz, P. Kurpiers, J. Schär, F. Marxer, J. Lütolf, T. Walter, J. C. Besse, M. Gabureac, K. Reuer, A. Akin, B. Royer, A. Blais, and A. Wallraff, "Microwave Quantum Link between Superconducting Circuits Housed in Spatially Separated Cryogenic Systems," *Physical Review Letters,* vol. 125, no. 26, p. 260502, 2020.

[85] F. K. Florian Fesquet, Michael Renger, Qiming Chen, Kedar Honasoge, Oscar Gargiulo, Yuki Nojiri, Achim Marx, Frank Deppe, Rudolf Gross, Kirill G. Fedorov, "Perspectives of microwave quantum key distribution in open-air," *arXiv:2203.05530*.

[86] H. Hemmati and D. Caplan, "Chapter 4 - Optical Satellite Communications," in *Optical Fiber Telecommunications (Sixth Edition)*, I. P. Kaminow, T. Li, and A. E. Willner Eds. Boston: Academic Press, 2013, pp. 121–162.

[87] M. Karmoose, C. Fragouli, S. Diggavi, R. Misoczki, L. L. Yang, and Z. L. Zhang, "Using mm-Waves for Secret Key Establishment," *IEEE Communications Letters,* vol. 23, no. 6, pp. 1077–1080, 2019.

[88] Z. Q. Wang, R. Malaney, and J. Green, "Inter-satellite Quantum Key Distribution at Terahertz Frequencies," in *IEEE International Conference on Communications (IEEE ICC)*, Shanghai, PEOPLES R CHINA, May 20–24 2019, in IEEE International Conference on Communications, 2019,

[89] Y. Q. He, Y. Y. Mao, D. Huang, Q. Liao, and Y. Guo, "Indoor channel modeling for continuous variable quantum key distribution in the terahertz band," *Optics Express,* vol. 28, no. 22, pp. 32386–32402, 2020.

[90] I. H. L. Grande, S. Etcheverry, J. Aldama, S. Ghasemi, D. Nolan, and V. Pruneri, "Adaptable transmitter for discrete and continuous variable quantum key distribution," *Optics Express,* vol. 29, no. 10, pp. 14815–14827, 2021.

[91] R. Jantti, R. Di Candia, R. F. Duan, and K. Ruttik, "Multiantenna Quantum Backscatter Communications," in *36th IEEE Global Communications Conference (GLOBECOM)*, Singapore, SINGAPORE, Dec 04–08 2017, in IEEE Globecom Workshops, 2017,

[92] H. Deng and A. Sayeed, "Mm-Wave MIMO Channel Modeling and User Localization Using Sparse Beamspace Signatures," in *IEEE 15th International Workshop on Signal Processing Advances in Wireless Communications (SPAWC)*, Toronto, CANADA, Jun 22–25 2014, in IEEE International Workshop on Signal Processing Advances in Wireless Communications, 2014, pp. 130–134.

[93] S. A. Busari, K. M. S. Huq, S. Mumtaz, and J. Rodriguez, "Terahertz Massive MIMO for Beyond-5G Wireless Communication," in *IEEE International Conference on Communications (IEEE ICC)*, Shanghai, PEOPLES R CHINA, May 20–24 2019, in IEEE International Conference on Communications, 2019,

[94] B. Kraus, N. Gisin, and R. Renner, "Lower and Upper Bounds on the Secret-Key Rate for Quantum Key Distribution Protocols Using One-Way Classical Communication," *Physical Review Letters,* vol. 95, no. 8, p. 080501, 2005.

[95] R. Renner and J. I. Cirac, "de Finetti Representation Theorem for Infinite-Dimensional Quantum Systems and Applications to Quantum Cryptography," *Physical Review Letters,* vol. 102, no. 11, p. 110504, 2009.

[96] F. Grosshans, G. Van Assche, J. Wenger, R. Brouri, N. J. Cerf, and P. Grangier, "Quantum key distribution using gaussian-modulated coherent states," *Nature,* vol. 421, no. 6920, pp. 238–241, 2003.

[97] C. Weedbrook, S. Pirandola, R. Garcia-Patron, N. J. Cerf, T. C. Ralph, J. H. Shapiro, and S. Lloyd, "Gaussian quantum information," *Reviews of Modern Physics,* vol. 84, no. 2, pp. 621–669, 2012.

[98] Y. Liao, K. Wang, H. Zhu, and X. Ji, "Crosstalk in CMOS Terahertz Detector Array With On-Chip SPR Antenna," *IEEE Photonics Journal,* vol. 14, no. 6, pp. 1–6, 2022.

[99] C. Weedbrook, S. Pirandola, S. Lloyd, and T. C. Ralph, "Quantum Cryptography Approaching the Classical Limit," *Physical Review Letters,* vol. 105, no. 11, 2010.

[100] Y. H. Yang, A. Shutler, and D. Grischkowsky, "Measurement of the transmission of the atmosphere from 0.2 to 2 THz," *Optics Express,* vol. 19, no. 9, pp. 8830–8838, 2011.

[101] H. Guerboukha, R. Shrestha, J. Neronha, O. Ryan, M. Hornbuckle, Z. Fang, and D. M. Mittleman, "Efficient leaky-wave antennas at terahertz frequencies generating highly directional beams," *Applied Physics Letters,* vol. 117, no. 26, p. 261103, 2020.

[102] Z. Zhao, R. Zhang, H. Song, K. Pang, A. Almaiman, H. Zhou, H. Song, C. Liu, N. Hu, X. Su, A. Minoofar, H. Sasaki, D. Lee, M. Tur, A. F. Molisch, and A. E. Willner, "Modal coupling and crosstalk due to turbulence and divergence on free space THz links using multiple orbital angular momentum beams," *Scientific Reports,* vol. 11, no. 1, p. 2110, 2021.

[103] X. Su, R. Zhang, Z. Zhao, H. Song, A. Minoofar, N. Hu, H. Zhou, K. Zou, K. Pang, H. Song, B. Lynn, S. Zach, M. Tur, A. F. Molisch, H. Sasaki, D. Lee, and A. E. Willner, "Receiver aperture and multipath effects on power loss and modal crosstalk in a THz wireless link using orbital-angular-momentum multiplexing," *Scientific Reports,* vol. 12, no. 1, p. 14053, 2022.

[104] S. Kalhor, S. Savel'ev, and K. Delfanazari, "Engineering ultrastrong coupling between Josephson plasmon polaritons and subwavelength microcavity arrays in silicon/van der Waals layered superconductor heterostructure for terahertz hybrid circuit cavity quantum electrodynamics," *Physical Review B,* vol. 106, no. 24, p. 245140, 2022.

[105] P. Huang, T. Wang, R. Chen, P. Wang, Y. Zhou, and G. Zeng, "Experimental continuous-variable quantum key distribution using a thermal source," *New Journal of Physics,* vol. 23, no. 11, p. 113028, 2021.

[106] M. Zhang, P. Huang, P. Wang, S. Wei, and G. Zeng, "Experimental free-space continuous-variable quantum key distribution with thermal source," *Opt. Lett.,* vol. 48, no. 5, pp. 1184–1187, 2023.

[107] X. Chen, H. Lindley-Hatcher, R. I. Stantchev, J. Wang, K. Li, A. Hernandez Serrano, Z. D. Taylor, E. Castro-Camus, and E. Pickwell-MacPherson, "Terahertz (THz) biophotonics technology: Instrumentation, techniques, and biomedical applications," *Chemical Physics Reviews,* vol. 3, no. 1, p. 011311, 2022.

[108] M. Zhang, S. Pirandola, and K. Delfanazari, "Millimetre-Waves to Terahertz SISO and MIMO Continuous Variable Quantum Key Distribution," *IEEE Transactions on Quantum Engineering,* pp. 1–11, 2023.

[109] F. A. Dicandia, N. J. G. Fonseca, M. Bacco, S. Mugnaini, and S. Genovesi, "Space-Air-Ground Integrated 6G Wireless Communication Networks: A Review of Antenna Technologies and Application Scenarios," *Sensors*, vol. 22, no. 9.

[110] K. Delfanazari, "On-chip coherent terahertz emitters with gigahertz modulation," *Nature Photonics,* vol. 18, no. 3, pp. 214–215, 2024.

[111] S. P. Kish, P. J. Gleeson, A. Walsh, P. K. Lam, and S. M. Assad, "Comparison of Discrete Variable and Continuous Variable Quantum Key Distribution Protocols with Phase Noise in the Thermal-Loss Channel," *Quantum,* vol. 8, pp. 1382–1382, 2024.

[112] H. Wang, Y. Pan, Y. Shao, Y. Pi, T. Ye, Y. Li, T. Zhang, J. Liu, J. Yang, L. Ma, W. Huang, and B. Xu, "Performance analysis for OFDM-based multi-carrier continuous-variable quantum key distribution with an arbitrary modulation protocol," *Optics Express,* vol. 31, no. 4, pp. 5577–5592, 2023.

[113] C. Shaoping and Z. Cuitao, "ICI and ISI analysis and mitigation for OFDM systems with insufficient cyclic prefix in time-varying channels," *IEEE Transactions on Consumer Electronics,* vol. 50, no. 1, pp. 78–83, 2004.

[114] W. Lee, S. Han, S.-R. Moon, J. Park, S. Yoo, H. Park, J. K. Lee, K. Yu, and S. H. Cho, "Coherent terahertz wireless communication using dual-parallel MZM-based silicon photonic integrated circuits," *Optics Express,* vol. 30, no. 2, pp. 2547–2563, 2022.

[115] M. Miyamoto, R. Kobayashi, G. Kuwano, M. Tsujimoto, and I. Kakeya, "Wide-band frequency modulation of a terahertz intrinsic Josephson junction emitter of a cuprate superconductor," *Nature Photonics,* vol. 18, no. 3, pp. 267–275, 2024.

[116] F. Laudenbach, C. Pacher, C.-H. F. Fung, A. Poppe, M. Peev, B. Schrenk, M. Hentschel, P. Walther, and H. Hübel, "Continuous-Variable Quantum Key Distribution with Gaussian Modulation—The Theory of Practical Implementations," *Advanced Quantum Technologies,* vol. 1, no. 1, p. 1800011, 2018.

[117] V. Scarani, H. Bechmann-Pasquinucci, N. J. Cerf, M. Dusek, N. Lutkenhaus, and M. Peev, "The security of practical quantum key distribution," *Reviews of Modern Physics,* vol. 81, no. 3, pp. 1301–1350, 2009.

[118] X. Liu, C. Xu, S. X. Ng, and L. Hanzo, "OTFS-Based CV-QKD Systems for Doubly Selective THz Channels," *IEEE Transactions on Communications,* vol. 73, no. 8, pp. 6274–6289, 2025.

[119] C. Weedbrook, S. Pirandola, and T. C. Ralph, "Continuous-variable quantum key distribution using thermal states," *Physical Review A,* vol. 86, no. 2, p. 022318, 2012.

[120] Y. Yang, M. Mandehgar, and D. Grischkowsky, "Determination of the water vapor continuum absorption by THz-TDS and Molecular Response Theory," *Optics Express,* vol. 22, no. 4, pp. 4388–4403, 2014.

[121] D. M. Slocum, E. J. Slingerland, R. H. Giles, and T. M. Goyette, "Atmospheric absorption of terahertz radiation and water vapor continuum effects," *Journal of Quantitative Spectroscopy and Radiative Transfer,* vol. 127, pp. 49–63, 2013.

[122] I. E. Gordon, L. S. Rothman, R. J. Hargreaves, R. Hashemi, E. V. Karlovets, F. M. Skinner, E. K. Conway, C. Hill, R. V. Kochanov, Y. Tan, P. Wcisło, A. A. Finenko, K. Nelson, P. F. Bernath, M. Birk, V. Boudon, A. Campargue, K. V. Chance, A. Coustenis, B. J. Drouin, J. M. Flaud, R. R. Gamache, J. T. Hodges, D. Jacquemart, E. J. Mlawer, A. V. Nikitin, V. I. Perevalov, M. Rotger, J. Tennyson, G. C. Toon, H. Tran, V. G. Tyuterev, E. M. Adkins, A. Baker, A. Barbe, E. Canè, A. G. Császár, A. Dudaryonok, O. Egorov, A. J. Fleisher, H. Fleurbaey, A. Foltynowicz, T. Furtenbacher, J. J. Harrison, J. M. Hartmann, V. M. Horneman, X. Huang, T. Karman, J. Karns, S. Kassi, I. Kleiner, V. Kofman, F. Kwabia–Tchana, N. N. Lavrentieva, T. J. Lee, D. A. Long, A. A. Lukashevskaya, O. M. Lyulin, V. Y. Makhnev, W. Matt, S. T. Massie, M. Melosso, S. N. Mikhailenko, D. Mondelain, H. S. P. Müller, O. V. Naumenko, A. Perrin, O. L. Polyansky,

E. Raddaoui, P. L. Raston, Z. D. Reed, M. Rey, C. Richard, R. Tóbiás, I. Sadiek, D. W. Schwenke, E. Starikova, K. Sung, F. Tamassia, S. A. Tashkun, J. Vander Auwera, I. A. Vasilenko, A. A. Vigasin, G. L. Villanueva, B. Vispoel, G. Wagner, A. Yachmenev, and S. N. Yurchenko, "The HITRAN2020 molecular spectroscopic database," *Journal of Quantitative Spectroscopy and Radiative Transfer,* vol. 277, p. 107949, 2022.

[123] W. Zhao, Q. Liao, D. Huang, and Y. Guo, "Performance analysis of the satellite-to-ground continuous-variable quantum key distribution with orthogonal frequency division multiplexed modulation," *Quantum Information Processing,* vol. 18, no. 1, p. 39, 2018.

[124] A. Hosseinzadeh and C. T. Middlebrook, "Linearity optimizations of analog ring resonator modulators through bias voltage adjustments," *Optics Communications,* vol. 410, pp. 345–349, 2018.

[125] L. Samara, S. Haussmann, E. Tufa, A. A. D. Amico, T. Zugno, I. Kallfass, and T. Kürner, "Sub-THz Power Amplifiers: Measurements, Behavioral Modeling, and Predistortion Algorithms," *IEEE Transactions on Terahertz Science and Technology,* vol. 15, no. 6, pp. 1007–1019, 2025.

[126] S. Sekimoto, C. Watanabe, H. Minami, T. Yamamoto, T. Kashiwagi, R. A. Klemm, and K. Kadowaki, "Continuous 30 μW terahertz source by a high-Tc superconductor mesa structure," *Applied Physics Letters,* vol. 103, no. 18, p. 182601, 2013.

[127] R. Wieland, O. Kizilaslan, N. Kinev, E. Dorsch, S. Guénon, Z. Song, Z. Wei, H. Wang, P. Wu, D. Koelle, V. P. Koshelets, and R. Kleiner, "Terahertz emission from mutually synchronized standalone $Bi_2Sr_2CaCu_2O_{8+x}$ intrinsic-Josephson-junction stacks," *Physical Review Applied,* vol. 22, no. 4, p. 044022, 2024.

[128] Y. Cai, L. Zhang, J. Zhang, B. Hua, K. Ma, J. Ding, X. Bian, M. Lei, Y. Liu, J. Li, Z. Xin, X. Chen, J. Cai, P. Pan, Y. Huang, J. Feng, M. Zhu, and X. You, "Surpassing kilometer-scale terahertz wireless communication beyond 300 GHz enabled by hybrid photonic–electronic synergy," *Light: Science & Applications,* vol. 15, no. 1, p. 228, 2026.

[129] H. Hamada, T. Tsutsumi, H. Matsuzaki, T. Fujimura, I. Abdo, A. Shirane, K. Okada, G. Itami, H. J. Song, H. Sugiyama, and H. Nosaka, "300-GHz-Band 120-Gb/s Wireless Front-End Based on InP-HEMT PAs and Mixers," *IEEE Journal of Solid-State Circuits,* vol. 55, no. 9, pp. 2316–2335, 2020.

[130] L. John, F. Thome, A. Leuther, and A. Tessmann, "Broadband InGaAs mHEMT THz Transmitters and Receivers," in *Optical Fiber Communication Conference (OFC) 2024*, San Diego California, 2024/03/24 2024: Optica Publishing Group, in Technical Digest Series, p. W4A.5.

[131] C. Liu, Y. Chao, L. Wang, C. Zhu, and Q. Li, "Continuous variable quantum key distribution based on simultaneous quantum and classical communication in the terahertz band," *Applied Optics,* vol. 62, no. 26, pp. 7024–7035, 2023.

[132] S. Shi, S. Yuan, J. Zhou, and P. Jiang, "Terahertz technology and its applications in head and neck diseases," (in eng), *iScience,* vol. 26, no. 7, p. 107060, 2023.

[133] W. Nsengiyumva, S. Zhong, L. Zheng, W. Liang, B. Wang, Y. Huang, X. Chen, and Y. Shen, "Sensing and Nondestructive Testing Applications of Terahertz Spectroscopy and Imaging Systems: State-of-the-Art and State-of-the-Practice," *IEEE Transactions on Instrumentation and Measurement,* vol. 72, pp. 1–83, 2023.

[134] M. Kutas, B. Haase, P. Bickert, F. Riexinger, D. Molter, and G. von Freymann, "Terahertz quantum sensing," *Science Advances,* vol. 6, no. 11, p. eaaz8065.

[135] Y. Todorov, S. Dhillon, and J. Mangeney, "THz quantum gap: exploring potential approaches for generating and detecting non-classical states of THz light," vol. 13, no. 10, pp. 1681–1691, 2024.

[136] T. Mochiku and K. Kadowaki, "Growth and properties of $Bi_2Sr_2(Ca, Y)Cu_2O_{8+\delta}$ single crystals," *Physica C: Superconductivity,* vol. 235-240, pp. 523–524, 1994.

[137] R. Kleiner, F. Steinmeyer, G. Kunkel, and P. MÜLler, "Intrinsic Josephson effects in $Bi_2Sr_2CaCu_2O_8$ single crystals," *Phys Rev Lett,* vol. 68, no. 15, pp. 2394–2397, 1992.

[138] C. Watanabe, H. Minami, T. Yamamoto, T. Kashiwagi, R. A. Klemm, and K. Kadowaki, "Spectral investigation of hot spot and cavity resonance effects on the terahertz radiation from high-Tc superconducting $Bi_2Sr_2CaCu_2O_{8+\delta}$ mesas," *Journal of Physics: Condensed Matter,* vol. 26, no. 17, p. 172201, 2014.

[139] N. Miyakawa, P. Guptasarma, J. F. Zasadzinski, D. G. Hinks, and K. E. Gray, "Strong Dependence of the Superconducting Gap on Oxygen Doping from Tunneling Measurements on $Bi_2Sr_2CaCu_2O_{8-\delta}$," *Physical Review Letters,* vol. 80, no. 1, pp. 157–160, 1998.

[140] C. Kurter, K. E. Gray, J. F. Zasadzinski, L. Ozyuzer, A. E. Koshelev, Q. Li, T. Yamamoto, K. Kadowaki, W. K. Kwok, M. Tachiki, and U. Welp, "Thermal Management in Large Bi2212 Mesas Used for Terahertz Sources," *IEEE Transactions on Applied Superconductivity,* vol. 19, no. 3, pp. 428–431, 2009.

[141] R. A. Klemm and K. Kadowaki, "Output from a Josephson stimulated terahertz amplified radiation emitter," *Journal of Physics: Condensed Matter,* vol. 22, no. 37, p. 375701, 2010.

[142] M. Tachiki, M. Iizuka, K. Minami, S. Tejima, and H. Nakamura, "Emission of continuous coherent terahertz waves with tunable frequency by intrinsic Josephson junctions," *Physical Review B,* vol. 71, no. 13, p. 134515, 2005.

[143] L. N. Bulaevskii and A. E. Koshelev, "Radiation due to Josephson Oscillations in Layered Superconductors," *Physical Review Letters,* vol. 99, no. 5, p. 057002, 2007.

[144] A. Elarabi, Y. Yoshioka, M. Tsujimoto, and I. Kakeya, "Circularly polarized terahertz radiation monolithically generated by cylindrical mesas of intrinsic Josephson junctions," *Applied Physics Letters,* vol. 113, no. 5, p. 052601, 2018.

[145] T. M. Benseman, K. E. Gray, A. E. Koshelev, W. K. Kwok, U. Welp, H. Minami, K. Kadowaki, and T. Yamamoto, "Powerful terahertz emission from $Bi_2Sr_2CaCu_2O_{8+\delta}$ mesa arrays," *Applied Physics Letters,* vol. 103, no. 2, p. 022602, 2013.

[146] Y. Saito, I. Kakeya, and Y. Takano, "Polarization analysis of terahertz emission from Bi-2212 cross-whisker intrinsic Josephson junction devices and their refractive index," *Applied Physics Letters,* vol. 121, no. 21, p. 212601, 2022.

[147] M. Tsujimoto, H. Minami, K. Delfanazari, M. Sawamura, R. Nakayama, T. Kitamura, T. Yamamoto, T. Kashiwagi, T. Hattori, and K. Kadowaki, "Terahertz imaging system using high-Tc superconducting oscillation devices," *Journal of Applied Physics,* vol. 111, no. 12, p. 123111, 2012.

[148] M. Tsujimoto, K. Delfanazari, T. Kashiwagi, T. Hattori, and K. Kadowaki, "Terahertz imaging system with on-chip superconducting Josephson plasma emitters for nondestructive testing," *arXiv preprint arXiv:2305.14643,* 2023.

[149] M. Li, J. Yuan, N. Kinev, J. Li, B. Gross, S. Guénon, A. Ishii, K. Hirata, T. Hatano, D. Koelle, R. Kleiner, V. P. Koshelets, H. Wang, and P. Wu, "Linewidth dependence of coherent terahertz emission from $Bi_2Sr_2CaCu_2O_8$ intrinsic Josephson junction stacks in the hot-spot regime," *Physical Review B,* vol. 86, no. 6, p. 060505, 2012.

[150] H. Minami, C. Watanabe, K. Sato, S. Sekimoto, T. Yamamoto, T. Kashiwagi, R. A. Klemm, and K. Kadowaki, "Local SiC photoluminescence evidence of hot spot formation and sub-THz coherent emission from a rectangular $Bi_2Sr_2CaCu_2O_{8+\delta}$ mesa," *Physical Review B,* vol. 89, no. 5, p. 054503, 2014.

[151] E. Sobakinskaya, V. L. Vaks, N. Kinev, M. Ji, M. Y. Li, H. B. Wang, and V. P. Koshelets, "High-resolution terahertz spectroscopy with a noise radiation source based on high-Tc superconductors," *Journal of Physics D: Applied Physics,* vol. 50, no. 3, p. 035305, 2017.

[152] R. Kleiner and H. Wang, "Terahertz emission from $Bi_2Sr_2CaCu_2O_{8+x}$ intrinsic Josephson junction stacks," *Journal of Applied Physics,* vol. 126, no. 17, 2019.

[153] H. B. Wang, S. Guénon, J. Yuan, A. Iishi, S. Arisawa, T. Hatano, T. Yamashita, D. Koelle, and R. Kleiner, "Hot Spots and Waves in $Bi_2Sr_2CaCu_2O_8$ Intrinsic Josephson Junction Stacks: A Study by Low Temperature Scanning Laser Microscopy," *Physical Review Letters,* vol. 102, no. 1, p. 017006, 2009.

[154] D. R. Kazanov and A. M. Monakhov, "Optical Modes in Elliptical Microcavities for Single-Photon Sources," *JETP Letters,* vol. 117, no. 6, pp. 422–427, 2023.

[155] P. Series, "Attenuation by atmospheric gases and related effects," *Recommendation ITU-R 25,* pp. 676–12, 2019.

[156] K. Delfanazari, "Chip-scale electrically driven superconducting coherent photon sources for quantum information processing," *Nature Photonics,* 2025.